Monatsh Chem
DOI 10.1007/s00706-009-0128-4

REVIEW

Room-temperature spin-transition iron compounds

**Ivan Šalitroš · N. T. Madhu · Roman Boča ·
Ján Pavlik · Mario Ruben**

Received: 17 December 2008 / Accepted: 22 December 2008

Abstract Since the discovery of the spin transition phenomenon in tris(*N*,*N*-dialkyldithiocarbamato) iron(III) complexes [1], numerous investigations have been devoted to this field of molecular magnetism. The spin transition phenomenon is probably the most spectacular example of bistability in molecular chemistry. However, it is a challenge to obtain spin transition materials when working under ambient conditions (e.g. room temperature and pressure), which would be highly advantageous for potential applications. So far, only some Fe(II) and Fe(III) molecular systems have shown temperature-induced spin transitions around and even above room temperature. Within this review we discuss the characteristics of this class of bistable compounds in detail and we try to draw more general conclusions regarding the integration, implementation and application of spin transition compounds as switching elements in hybrid molecular devices.

Keywords Iron complexes · Spin transition · Room temperature · Molecular magnetism

Introduction

The design of molecules that can be utilised for information processing and data storage is an attractive goal in present material science. However, one of the great challenges underlying the search for such molecule-based functional materials is to produce systems that exhibit properties of technological interest that can be tuned and exploited at room temperature. Some landmark achievements in this respect are the discovery of a molecule-based magnet that displays ordering above 300 °C [2], and the preparation of molecular materials that undergo spin transition near to room temperature [3].

In octahedral ligand fields, transition metal ions with d^4–d^7 configurations adopt either a high-spin (HS) or a low-spin (LS) electronic arrangement, according to whether the crystal field energy is lower or higher than the mean spin pairing energy. If the two energies are comparable, transitions between the two spin states can be brought about by varying the temperature for example. In many cases, particularly for ferrous compounds, bistability takes place, in other words the LS–HS and HS–LS transitions occur at different temperatures, forming a hysteresis loop. Materials in which thermally induced spin transitions take place near room temperature are interesting in view of their possible use as molecular electronic devices intended for the purpose of information recording and processing [4, 5].

Such spin transitions are triggered by external perturbations, such as electromagnetic radiation, magnetic fields, and pressure/temperature variations. Within crystalline phases, the response to the spin transition may be transmitted in a cooperative manner throughout the material, leading to hysteretic behaviour [6]. Such molecular solid state systems show characteristics of bistability, and can therefore be considered externally addressable molecular

I. Šalitroš · N. T. Madhu · M. Ruben (✉)
Institute for Nanotechnology, Karlsruhe Institute of Technology (KIT), PB-3640, 76021 Karlsruhe, Germany
e-mail: mario.ruben@int.fzk.de

I. Šalitroš · R. Boča (✉) · J. Pavlik
Faculty of Chemical and Food Technology,
Institute of Inorganic Chemistry,
Technology and Materials,
Slovak University of Technology,
Bratislava 812 37, Slovak Republic
e-mail: roman.boca@stuba.sk

switches. Current efforts are aimed at integrating spin transition systems into metal organic frameworks in order to combine their properties, such as chirality, conductivity, or those derived from nanoporosity. The molecular approach used to prepare hybrid materials has been mostly exploited to obtain networks that exhibit a wide range of pore size and shapes [7, 8], and which have the added potential of offering a variety of other functions, in particular because of the inclusion of transition metals [9]. This may lead to systems where the multifunctionality is manifested by the coexistence of more than one property, such as ferromagnetism and metal conductivity [10], with no mutual interdependence. The presence of different functions within a material can, however, occur in such a way that they influence each other in a synergetic manner, thereby producing effects that would not be observed if these properties were not coupled. Remarkable examples are, for instance, the observation of a switchable dielectric constant in a material controlled by the spin state of its spin transition centres [11], or the ability to modify the spin transition properties of a nanoporous framework by changing the nature of its guest molecules [12].

Temperature-dependent spin transition

Definition of spin transition

Atoms of first-row transition metals with electronic configurations d^4–d^7 (Cr^{II}, Mn^{III}, Fe^{III}, Mn^{II}, Fe^{II}, Co^{III}, Co^{II}) in an octahedral symmetry can adopt two different electronic ground states according to the occupation of the d orbitals split into the e_g and t_{2g} subsets. When the energy difference between these orbitals (Δ) is greater than the interelectronic repulsion energy (P), the electrons tend to occupy the orbitals of lower energy t_{2g}, and the configuration of the central metal ion is low spin (LS). In contrast, when $\Delta < P$, the d electrons obey Hund's rule, and the metal complex adopts the high-spin state (HS).

In-between these limits of high and low spin, a situation where the crystal field energy and interelectronic repulsion energy have similar values can occur. Here, the difference in energy between the HS and LS states is on the order of the magnitude of the thermal energy kT. The spin state of this type of molecule depends only on external conditions (T, p, B), and this kind of phenomenon is termed "spin transition" (ST) or "spin crossover" (SC) herein.

Conditions of the spin transition

The usual explanation of the spin crossover is based upon an orbital diagram, as exemplified in Fig. 1. Since the ground state is low spin, the electrons jump from nonbonding t_{2g} orbitals into the antibonding e_g counterparts, making the final state high spin. This also rationalizes a weakening of the bonds between the central atom and the donor set. The orbital picture, however, is a strongly oversimplified view, as this overlooks the interelectronic repulsion and spin-orbit coupling.

The explicit inclusion of the interelectronic repulsion means that the atomic terms $|\alpha, L, S, M_L, M_S\rangle$ are accounted for in the orbital and spin basis set. On adding the crystal field potential, the wavefunction of the central atom is represented by the crystal field terms $|\alpha, \Gamma, \gamma, S, M_S\rangle$, like $^1A_{1g}$ and $^5T_{2g}$ for Fe(II); $^2T_{2g}$ and $^6A_{1g}$ for Fe(III). Upon including the spin–orbit interaction (SOI), we arrive at the crystal field multiplets $|\alpha, \Gamma\prime, \gamma'\rangle$ which are classified in terms of irreducible representations of the respective double group (Γ_1 through Γ_8 for **O'**). While the crystal field terms are used in interpreting the *d*–*d* electron spectra, the crystal field multiplets form the basis for interpreting the magnetic properties.

A theoretical modeling of magnetic properties needs to include the interelectron repulsion (parametrized by the Racah parameters B and C for the central atom), the crystal field potential (parametrized by the crystal field strengths F_4 and eventually F_2, for each ligand, of which $10Dq = (10/6)F_4$), and the spin–orbit interaction (with the spin–orbit coupling constant ξ). Upon adding the orbital–Zeeman and spin–Zeeman interactions, the eigenvalues of the interaction Hamiltonian represent the Zeeman levels. The calculated energy levels enter into the partition function, from which the magnetization (M) and magnetic susceptibility (χ) are evaluated using the apparatus of statistical thermodynamics [13]. Instead of the magnetic susceptibility, the effective magnetic moment (μ_{eff}) is a more appropriate function to plot: $\mu_{\text{eff}} = [(3k/N_A\mu_0)\chi_{\text{mol}}T]^{1/2}$.

Modelling based upon the generalized crystal field (CF) theory has been done with $B = 1{,}122\ \text{cm}^{-1}$, $C = 4.2B$, and $\xi = 460\ \text{cm}^{-1}$ for Fe(III). The calculated temperature dependence of the effective magnetic moment is displayed in Fig. 2, and one can see that the spin crossover occurs only in a very narrow interval of the crystal field strength. With $F_4 = 17{,}700\ \text{cm}^{-1}$ the ground crystal field term is $^6A_{1g}$ (high spin), whereas with $F_4 = 18{,}200\ \text{cm}^{-1}$ it is $^2T_{2g}$ (low spin). At intermediate CF strength a delicate situation occurs. With $F_4 = 18{,}000\ \text{cm}^{-1}$, the ground CF term is $^6A_{1g}$, preventing the spin transition since it is already HS. However, the spin–orbit splitting of the excited $^2T_{2g}$ term ($690\ \text{cm}^{-1}$) is greater than the interterm gap ($425\ \text{cm}^{-1}$), so that the ground crystal field multiplet is $\Gamma_7(\times 2) \leftarrow {}^2T_{2g}$. Therefore, the condition for the spin crossover $\Delta S > 0$ is fulfilled and it proceeds according to the bold curve shown in Fig. 2. (Because of the calculations in the complete 252-member basis set spanned by d^5 functions, the second-order interaction of the lowest Γ_8–Γ_8 and Γ_7–Γ_7 parents is

Fig. 1 Orbital picture differentiating between low-spin and high-spin octahedral iron complexes: *left* Fe(II), *right* Fe(III)

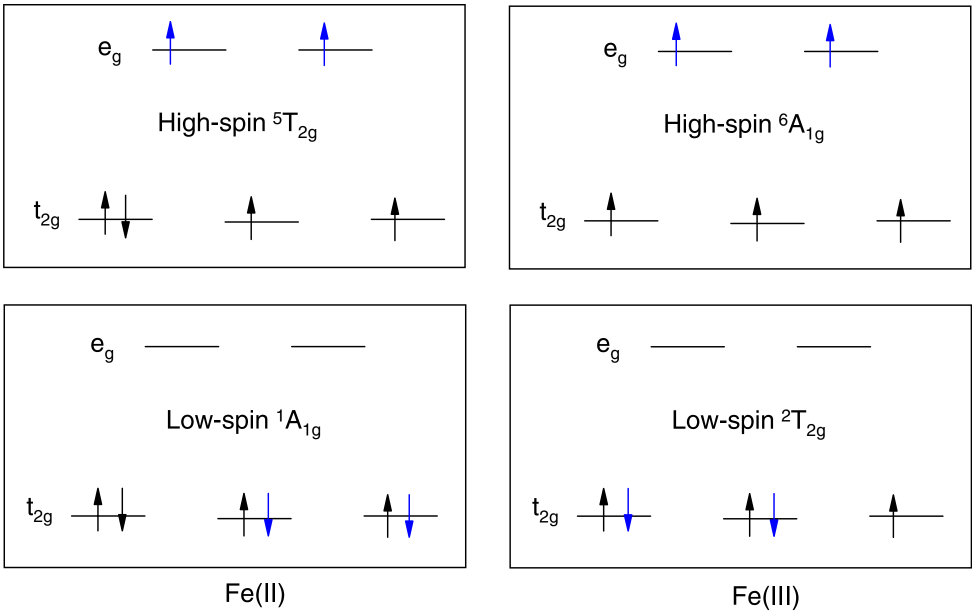

naturally involved.) The modelling described above shows that the situation in mononuclear Fe(III) complexes is much more complex than reported so far: instead of a single energy gap, we must consider two gaps.

The splitting of the isolated $^{2}T_{2g}(\times 6)$ crystal field term into $\Gamma_8 = U_{3/2}(\times 4)$ and $\Gamma_7 = E_{5/2}(\times 2)$ multiplets equals $(3/2)\lambda = (3/2)\xi = 690\ \mathrm{cm}^{-1}$ for Fe(III) and thus is rather high, whereas no splitting of the term $^{6}A_{1g} \rightarrow (\Gamma_8, \Gamma_7)$ occurs at the first order for an octahedral system.

The modelling of Fe(II) systems ($B = 897\ \mathrm{cm}^{-1}$, $C = 4.3B$, and $\xi = 400\ \mathrm{cm}^{-1}$) shows that the onset of the spin transition appears at $F_4 = 12{,}860\ \mathrm{cm}^{-1}$; with $F_4 = 14{,}000\ \mathrm{cm}^{-1}$ the complex is low spin. However, on passing to the high-temperature limit ($T > 1{,}000$ K), this complex also turns high spin. Only the $^{5}T_{2g}$ term is split by the spin–orbit coupling, and the SOI splitting amounts to $493\ \mathrm{cm}^{-1}$ (for $F_4 = 12{,}900\ \mathrm{cm}^{-1}$). It can be concluded that in the Fe(II) system the energy levels are grouped into four groups separated by three gaps.

The above modelling of the magnetic behaviour was done with the assumption of a regular octahedral arrangement (which is always absent in real systems), and with the approximation of a vertical excitation process.

The delicate balance of the crystal field strengths with respect to the electron repulsion used to be explained via Tanabe–Sugano diagrams. These were reconstructed with actual B and C parameters for Fe(II) and Fe(III), respectively, and they are displayed in Fig. 3. It can be seen that for Fe(II) systems the critical crossover of the $^{5}T_{2g} \leftrightarrow {}^{1}A_{1g}$ states appears at $Dq/B = 2.38$, which yields $Dq = 2{,}135\ \mathrm{cm}^{-1}$ and $F_4 = 12{,}809\ \mathrm{cm}^{-1}$, which is close to the "observed" onset value of the spin transition in Fig. 2. Analogously, for Fe(III), the critical crossover of $^{6}A_{1g} \leftrightarrow {}^{2}T_{2g}$ occurs at $Dq/B = 2.70$, which yields $Dq = 3{,}029\ \mathrm{cm}^{-1}$ and $F_4 = 18{,}176\ \mathrm{cm}^{-1}$ which again matches the region of the "observed" spin transition.

The drawback of these Tanabe–Sugano diagrams is that they are valid only for regular octahedral complexes. It would be helpful to have their analogues for decreased symmetry. Figure 4 provides such a picture, generated for three lowest energy levels and mapped as a function of the axial (2×) and equatorial (4×) ligand-field strengths. From diagrams like this, it is possible to read off the crystal field strengths bordering the crossover.

The crossover point in the Tanabe–Sugano diagram simply means that, for a given ligand, there is a nuclear configuration for which the LS and the HS states are accidentally degenerate. In general, such a nuclear configuration does not correspond to either of the equilibrium configurations, because in iron(II) the low-spin state with the $(t_2)^6$ configuration generally has a shorter metal–ligand bond length than the HS state with the $(t_2)^4(e)^2$ configuration by roughly 0.2 Å [14]. The condition for a thermal spin transition is that $\Delta E_{\mathrm{HL}} > 0$, and is of the order of kT. The $^{1}A_1$ state will only be populated at low temperatures if this condition is fulfilled. At higher temperatures, almost quantitative, entropy-driven population of the $^{5}T_2$ state will occur due to its 15-fold electronic degeneracy, along with a higher density of vibrational states.

The Fe(II)–ligand bond lengths in the LS state are typically $r_{\mathrm{LS}} \sim 1.96$–$2.00$ Å, resulting in a bond length difference between the HS and the LS states $\Delta r_{\mathrm{HL}} = r_{\mathrm{HS}} - r_{\mathrm{LS}}$ in the range of $\Delta r_{\mathrm{HL}} \sim 0.16$–$0.21$ Å. Thus, estimating from the proportionality $(10Dq^{\mathrm{LS}}/10Dq^{\mathrm{HS}}) = (r_{\mathrm{HS}}/r_{\mathrm{LS}})^5$, the ligand field strength is expected to increase by almost a factor of 2 upon passing from the

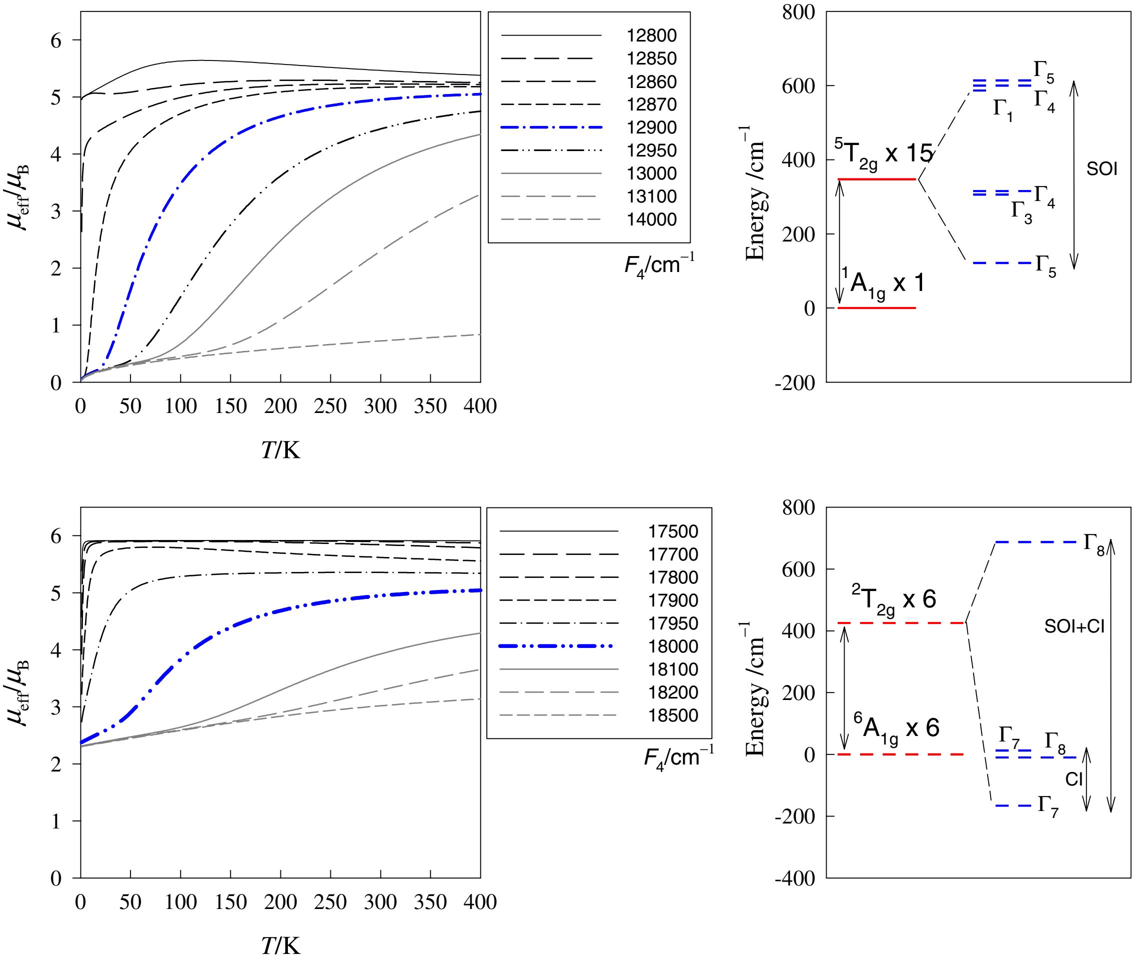

Fig. 2 Effective magnetic moment of octahedral iron complexes for various crystal field strengths, showing the spin transition. *Top panels*, Fe(II); *bottom*, Fe(III). Crystal field terms are labelled with Mulliken notation; crystal field multiplets are labelled with that of Bethe

HS to the LS state. In the Tanabe–Sugano diagram, an iron(II) spin transition compound $10Dq^{\mathrm{HS}}$ will be situated well to the left and $10Dq^{\mathrm{LS}}$ well to the right of the crossover point.

Experimental techniques for characterizing the spin transition

Various experimental techniques are suitable for determining the characteristics of a particular spin transition process. Initially, the ST is investigated by performing temperature-dependent magnetic susceptibility measurements. The molar susceptibility for a pure compound free of any paramagnetic impurity consists of the LS and HS fractions

$$\chi_{\mathrm{mol}} = x_{\mathrm{HS}}\chi_{\mathrm{HS}} + (1 - x_{\mathrm{HS}})\chi_{\mathrm{LS}} \tag{1}$$

where the mole fraction of the high-spin species (x_{HS}) is a temperature-dependent quantity. It can be calculated from the product functions χT as

$$x_{\mathrm{HS}} = \frac{\chi_{\mathrm{mol}}T - (\chi T)_{\mathrm{LT}}}{(\chi T)_{\mathrm{HT}} - (\chi T)_{\mathrm{LT}}} \tag{2}$$

The limits $(\chi T)_{\mathrm{LT}}$ and $(\chi T)_{\mathrm{HT}}$ can be detected from experimental data assuming that the Curie law is obeyed:

$$(\chi T)_{\mathrm{LS}} = C_0 g_{\mathrm{LS}}^2 S_{\mathrm{LS}}(S_{\mathrm{LS}} + 1)/3 \tag{3}$$

$$(\chi T)_{\mathrm{HS}} = C_0 g_{\mathrm{HS}}^2 S_{\mathrm{HS}}(S_{\mathrm{HS}} + 1)/3 \tag{4}$$

which contain the reduced Curie constant: $C_0 = N_{\mathrm{A}}\mu_0\mu_{\mathrm{B}}^2/k$. The high-spin mole fraction defines the equilibrium constant

$$K = \frac{x_{\mathrm{HS}}}{1 - x_{\mathrm{HS}}} \tag{5}$$

which enters the van't Hoff plot (i.e. the function ln$K$ versus T^{-1}).

Since the vast majority of ST compounds are either iron(II) or iron(III) complexes, temperature-dependent ^{57}Fe Mössbauer spectroscopy is very powerful tool for investigating the ST behaviour of iron compounds. Thereby, a

Fig. 3 Tanabe–Sugano diagrams for octahedral iron complexes (actual *B* and *C* values are used)

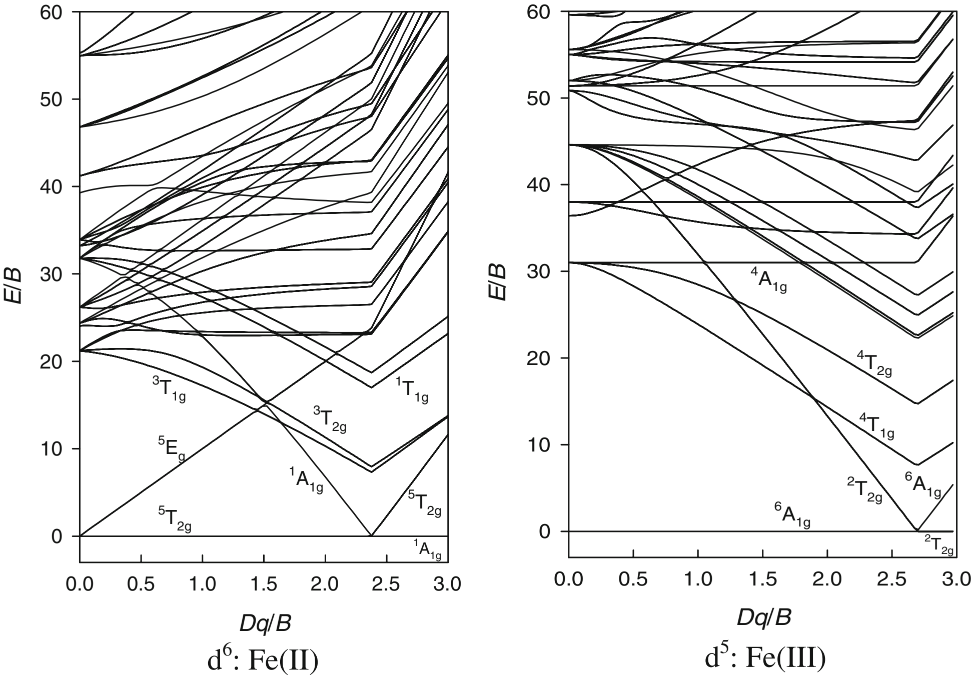

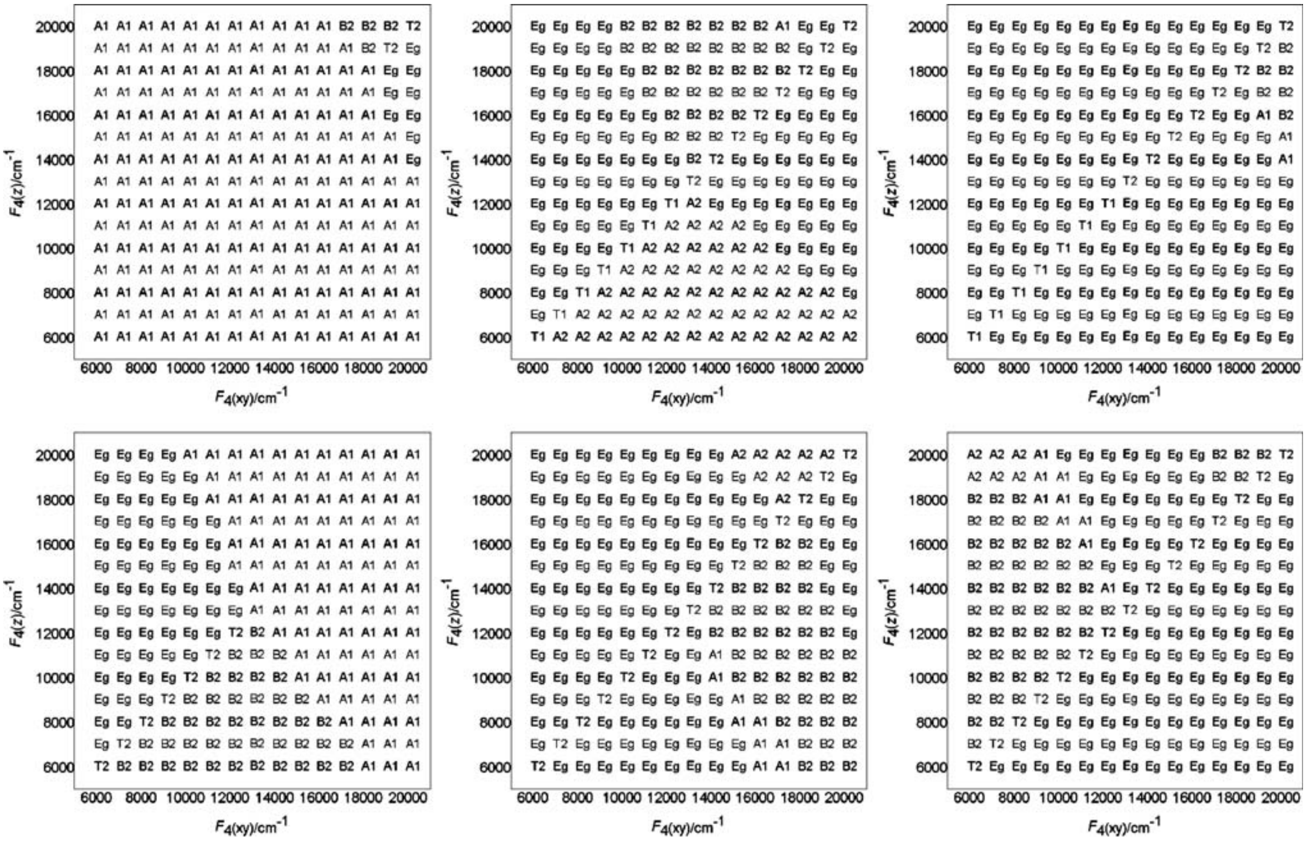

	6000		8000		10000		12000		14000		16000		18000		20000
20000	A1	A1	A1	A1	A1	A1	A1	A1	A1	A1	A1	B2	B2	B2	T2
	A1	A1	A1	A1	A1	A1	A1	A1	A1	A1	A1	A1	B2	T2	Eg
18000	A1	A1	A1	A1	A1	A1	A1	A1	A1	A1	A1	A1	A1	Eg	Eg
	A1	A1	A1	A1	A1	A1	A1	A1	A1	A1	A1	A1	A1	Eg	Eg
16000	A1	A1	A1	A1	A1	A1	A1	A1	A1	A1	A1	A1	A1	Eg	Eg
	A1	A1	A1	A1	A1	A1	A1	A1	A1	A1	A1	A1	A1	A1	Eg
14000	A1	A1	A1	A1	A1	A1	A1	A1	A1	A1	A1	A1	A1	A1	Eg
	A1	A1	A1	A1	A1	A1	A1	A1	A1	A1	A1	A1	A1	A1	A1
12000	A1	A1	A1	A1	A1	A1	A1	A1	A1	A1	A1	A1	A1	A1	A1
	A1	A1	A1	A1	A1	A1	A1	A1	A1	A1	A1	A1	A1	A1	A1
10000	A1	A1	A1	A1	A1	A1	A1	A1	A1	A1	A1	A1	A1	A1	A1
	A1	A1	A1	A1	A1	A1	A1	A1	A1	A1	A1	A1	A1	A1	A1
8000	A1	A1	A1	A1	A1	A1	A1	A1	A1	A1	A1	A1	A1	A1	A1
	A1	A1	A1	A1	A1	A1	A1	A1	A1	A1	A1	A1	A1	A1	A1
6000	A1	A1	A1	A1	A1	A1	A1	A1	A1	A1	A1	A1	A1	A1	A1

	6000		8000		10000		12000		14000		16000		18000		20000
20000	Eg	Eg	Eg	Eg	B2	B2	B2	B2	B2	B2	B2	A1	Eg	Eg	T2
	Eg	Eg	Eg	Eg	B2	B2	B2	B2	B2	B2	B2	B2	Eg	T2	Eg
18000	Eg	Eg	Eg	Eg	Eg	B2	B2	B2	B2	B2	B2	B2	T2	Eg	Eg
	Eg	Eg	Eg	Eg	Eg	B2	B2	B2	B2	B2	B2	T2	Eg	Eg	Eg
16000	Eg	Eg	Eg	Eg	Eg	Eg	B2	B2	B2	B2	T2	Eg	Eg	Eg	Eg
	Eg	Eg	Eg	Eg	Eg	Eg	B2	B2	B2	T2	Eg	Eg	Eg	Eg	Eg
14000	Eg	Eg	Eg	Eg	Eg	Eg	Eg	B2	T2	Eg	Eg	Eg	Eg	Eg	Eg
	Eg	Eg	Eg	Eg	Eg	Eg	Eg	T2	Eg	Eg	Eg	Eg	Eg	Eg	Eg
12000	Eg	Eg	Eg	Eg	Eg	Eg	T1	A2	Eg	Eg	Eg	Eg	Eg	Eg	Eg
	Eg	Eg	Eg	Eg	Eg	T1	A2	A2	A2	A2	Eg	Eg	Eg	Eg	Eg
10000	Eg	Eg	Eg	Eg	T1	A2	A2	A2	A2	A2	A2	Eg	Eg	Eg	Eg
	Eg	Eg	Eg	T1	A2	A2	A2	A2	A2	A2	A2	A2	Eg	Eg	Eg
8000	Eg	Eg	T1	A2	A2	A2	A2	A2	A2	A2	A2	A2	A2	A2	Eg
	Eg	T1	A2	A2	A2	A2	A2	A2	A2	A2	A2	A2	A2	A2	A2
6000	T1	A2	A2	A2	A2	A2	A2	A2	A2	A2	A2	A2	A2	A2	A2

	6000		8000		10000		12000		14000		16000		18000		20000
20000	Eg	Eg	Eg	Eg	Eg	Eg	Eg	Eg	Eg	Eg	Eg	Eg	Eg	Eg	T2
	Eg	Eg	Eg	Eg	Eg	Eg	Eg	Eg	Eg	Eg	Eg	Eg	Eg	T2	B2
18000	Eg	Eg	Eg	Eg	Eg	Eg	Eg	Eg	Eg	Eg	Eg	Eg	T2	B2	B2
	Eg	Eg	Eg	Eg	Eg	Eg	Eg	Eg	Eg	Eg	Eg	T2	Eg	B2	B2
16000	Eg	Eg	Eg	Eg	Eg	Eg	Eg	Eg	Eg	Eg	T2	Eg	Eg	A1	B2
	Eg	Eg	Eg	Eg	Eg	Eg	Eg	Eg	Eg	T2	Eg	Eg	Eg	Eg	A1
14000	Eg	Eg	Eg	Eg	Eg	Eg	Eg	Eg	T2	Eg	Eg	Eg	Eg	Eg	A1
	Eg	Eg	Eg	Eg	Eg	Eg	Eg	T2	Eg	Eg	Eg	Eg	Eg	Eg	Eg
12000	Eg	Eg	Eg	Eg	Eg	Eg	T1	Eg	Eg	Eg	Eg	Eg	Eg	Eg	Eg
	Eg	Eg	Eg	Eg	Eg	T1	Eg	Eg	Eg	Eg	Eg	Eg	Eg	Eg	Eg
10000	Eg	Eg	Eg	Eg	T1	Eg	Eg	Eg	Eg	Eg	Eg	Eg	Eg	Eg	Eg
	Eg	Eg	Eg	T1	Eg	Eg	Eg	Eg	Eg	Eg	Eg	Eg	Eg	Eg	Eg
8000	Eg	Eg	T1	Eg	Eg	Eg	Eg	Eg	Eg	Eg	Eg	Eg	Eg	Eg	Eg
	Eg	T1	Eg	Eg	Eg	Eg	Eg	Eg	Eg	Eg	Eg	Eg	Eg	Eg	Eg
6000	T1	Eg	Eg	Eg	Eg	Eg	Eg	Eg	Eg	Eg	Eg	Eg	Eg	Eg	Eg

	6000		8000		10000		12000		14000		16000		18000		20000
20000	Eg	Eg	Eg	Eg	A1	A1	A1	A1	A1	A1	A1	A1	A1	A1	A1
	Eg	Eg	Eg	Eg	Eg	A1	A1	A1	A1	A1	A1	A1	A1	A1	A1
18000	Eg	Eg	Eg	Eg	Eg	A1	A1	A1	A1	A1	A1	A1	A1	A1	A1
	Eg	Eg	Eg	Eg	Eg	Eg	A1	A1	A1	A1	A1	A1	A1	A1	A1
16000	Eg	Eg	Eg	Eg	Eg	Eg	A1	A1	A1	A1	A1	A1	A1	A1	A1
	Eg	Eg	Eg	Eg	Eg	Eg	A1	A1	A1	A1	A1	A1	A1	A1	A1
14000	Eg	Eg	Eg	Eg	Eg	Eg	Eg	A1	A1	A1	A1	A1	A1	A1	A1
	Eg	Eg	Eg	Eg	Eg	Eg	Eg	A1	A1	A1	A1	A1	A1	A1	A1
12000	Eg	Eg	Eg	Eg	Eg	Eg	T2	B2	A1	A1	A1	A1	A1	A1	A1
	Eg	Eg	Eg	Eg	Eg	T2	B2	B2	B2	A1	A1	A1	A1	A1	A1
10000	Eg	Eg	Eg	Eg	T2	B2	B2	B2	B2	A1	A1	A1	A1	A1	A1
	Eg	Eg	Eg	T2	B2	B2	B2	B2	B2	B2	A1	A1	A1	A1	A1
8000	Eg	Eg	T2	B2	B2	B2	B2	B2	B2	B2	B2	A1	A1	A1	A1
	Eg	T2	B2	B2	B2	B2	B2	B2	B2	B2	B2	B2	A1	A1	A1
6000	T2	B2	B2	B2	B2	B2	B2	B2	B2	B2	B2	B2	A1	A1	A1

	6000		8000		10000		12000		14000		16000		18000		20000
20000	Eg	Eg	Eg	Eg	Eg	Eg	Eg	Eg	Eg	A2	A2	A2	A2	A2	T2
	Eg	Eg	Eg	Eg	Eg	Eg	Eg	Eg	Eg	Eg	A2	A2	A2	T2	Eg
18000	Eg	Eg	Eg	Eg	Eg	Eg	Eg	Eg	Eg	Eg	Eg	A2	T2	Eg	Eg
	Eg	Eg	Eg	Eg	Eg	Eg	Eg	Eg	Eg	Eg	Eg	T2	Eg	Eg	Eg
16000	Eg	Eg	Eg	Eg	Eg	Eg	Eg	Eg	Eg	Eg	T2	B2	B2	Eg	Eg
	Eg	Eg	Eg	Eg	Eg	Eg	Eg	Eg	Eg	T2	B2	B2	B2	Eg	Eg
14000	Eg	Eg	Eg	Eg	Eg	Eg	Eg	Eg	T2	B2	B2	B2	B2	Eg	Eg
	Eg	Eg	Eg	Eg	Eg	Eg	Eg	T2	B2	B2	B2	B2	B2	B2	Eg
12000	Eg	Eg	Eg	Eg	Eg	Eg	T2	Eg	B2	B2	B2	B2	B2	B2	Eg
	Eg	Eg	Eg	Eg	Eg	T2	Eg	Eg	A1	B2	B2	B2	B2	B2	B2
10000	Eg	Eg	Eg	Eg	T2	Eg	Eg	Eg	A1	B2	B2	B2	B2	B2	B2
	Eg	Eg	Eg	T2	Eg	Eg	Eg	Eg	Eg	A1	B2	B2	B2	B2	B2
8000	Eg	Eg	T2	Eg	Eg	Eg	Eg	Eg	Eg	A1	A1	B2	B2	B2	B2
	Eg	T2	Eg	Eg	Eg	Eg	Eg	Eg	Eg	Eg	A1	A1	B2	B2	B2
6000	T2	Eg	Eg	Eg	Eg	Eg	Eg	Eg	Eg	Eg	A1	A1	B2	B2	B2

	6000		8000		10000		12000		14000		16000		18000		20000
20000	A2	A2	A2	A1	Eg	Eg	Eg	Eg	Eg	Eg	Eg	B2	B2	B2	T2
	A2	A2	A2	A1	A1	Eg	Eg	Eg	Eg	Eg	Eg	B2	B2	T2	Eg
18000	B2	B2	B2	A1	A1	Eg	Eg	Eg	Eg	Eg	Eg	Eg	T2	Eg	Eg
	B2	B2	B2	B2	A1	A1	Eg	Eg	Eg	Eg	Eg	T2	Eg	Eg	Eg
16000	B2	B2	B2	B2	B2	A1	Eg	Eg	Eg	Eg	T2	Eg	Eg	Eg	Eg
	B2	B2	B2	B2	B2	B2	Eg	Eg	Eg	T2	Eg	Eg	Eg	Eg	Eg
14000	B2	B2	B2	B2	B2	B2	A1	Eg	T2	Eg	Eg	Eg	Eg	Eg	Eg
	B2	B2	B2	B2	B2	B2	B2	T2	Eg	Eg	Eg	Eg	Eg	Eg	Eg
12000	B2	B2	B2	B2	B2	B2	T2	Eg	Eg	Eg	Eg	Eg	Eg	Eg	Eg
	B2	B2	B2	B2	B2	T2	Eg	Eg	Eg	Eg	Eg	Eg	Eg	Eg	Eg
10000	B2	B2	B2	B2	T2	Eg	Eg	Eg	Eg	Eg	Eg	Eg	Eg	Eg	Eg
	B2	B2	B2	T2	Eg	Eg	Eg	Eg	Eg	Eg	Eg	Eg	Eg	Eg	Eg
8000	B2	B2	T2	Eg	Eg	Eg	Eg	Eg	Eg	Eg	Eg	Eg	Eg	Eg	Eg
	B2	T2	Eg	Eg	Eg	Eg	Eg	Eg	Eg	Eg	Eg	Eg	Eg	Eg	Eg
6000	T2	Eg	Eg	Eg	Eg	Eg	Eg	Eg	Eg	Eg	Eg	Eg	Eg	Eg	Eg

Fig. 4 Generalized Tanabe–Sugano diagrams for the three lowest energy levels of the $[ML_4^{equ}L_2^{ax}]$ bipyramidal complex. *Top*, *d*^{5}; *bottom*, *d*^{6} system

^{57}Co nucleus-based source (14.4 keV) that moves with a defined velocity emits characteristic γ-rays that are absorbed by the sample, leading to the excitation of ^{57}Fe nuclei (natural abundance is 2.17%) within the sample. The characteristics of the absorption depend on the chemical environment of the ^{57}Fe nucleus and the velocity of the cobalt source. Figure 5 depicts the origin of the absorption of the ^{57}Fe nucleus and the derivation of the Mössbauer spectral parameters as follows.

1. The isomer shift δ [mm s^{-1}] arises from the interaction between the iron nucleus and *s* electrons. From this parameter, we can obtain information about the spin state of iron, its oxidation number, and the nature of the bonding (Table 1).
2. The quadrupole splitting ΔE_Q [mm s^{-1}] originates from the interaction between the quadrupole moment of the iron nucleus and the electric field of the *s* electron cloud, which gives us an idea of the spin state and oxidation number of iron.
3. The magnetic quadrupole splitting ΔE_M [mm s^{-1}] arises in two different cases: if the sample is situated in an external magnetic field and/or if the sample possesses a remnant magnetic field (a ferromagnetic material). Since this parameter describes the interaction of the magnetic moments of nuclei with the magnetic field, local information about magnetic interactions (ferro- or antiferromagnetic) can be retrieved in this way.
4. The peak area *A* [%] is an important parameter for spin-transition iron complexes, since this gives a quantitative evaluation of the electronic state of the iron ion.

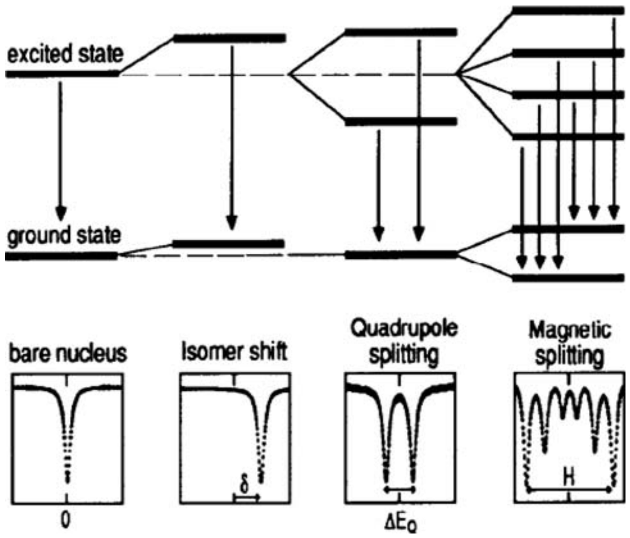

Fig. 5 Origin of Mössbauer spectral parameters in the ^{57}Fe nucleus

Table 1 Typical ranges of isomer shifts δ for various oxidation numbers and spin states (*S*) of iron

Type	*S*	δ/mm s^{-1}
Fe(II)	2	0.7–1.3
	1	0.2–0.5
	0	−0.2–0.3
Fe(III)	5/2	0.2–0.5
	3/2	0.2–0.4
	1/2	−0.5–0.4

Temperature-dependent far-infrared vibration spectroscopy is another useful tool for the investigation of ST compounds, as the spin transition causes changes in the vibrational states of the coordination polyhedron. As the temperature increases the intensity of the LS vibrations decrease and the HS peaks increase. The respective peak areas give rise to the mole fraction

$$x_{\mathrm{HS}}(T) = \frac{A(T) - A_{\min}}{A_{\max} - A_{\min}} \tag{6}$$

The spin transition (ST) in the solid state is associated with a first-order phase transition. Since the cell parameters of the crystal lattice alter during the spin transition, X-ray powder diffraction can be utilized to monitor the ST process. Single-crystal X-ray structure analysis for the pure low-spin and high-spin species results in bond lengths that show characteristic changes for individual central atoms (Table 2). The EXAFS technique is also applicable in this respect.

Since it is an ideal technique for the investigation of phase transitions in general, calorimetry has been also applied to spin transition systems, and it allows the changes in thermodynamic quantities such as enthalpy and entropy to be determined [13]. The enthalpy change $\Delta_{\mathrm{trs}}H = \Delta H_{\mathrm{HS}} - \Delta H_{\mathrm{LS}}$ is typically 10–20 kJ mol^{-1}, and the entropy change $\Delta_{\mathrm{trs}}S = S_{\mathrm{HS}} - S_{\mathrm{LS}}$ is on the order of 50–80 J K^{-1} mol^{-1}.

Classification of spin transitions

Temperature-dependent spin transitions occur in the crystalline and amorphous solid states as well as in liquid

Table 2 Typical changes in bond lengths in the coordination polyhedra of some ST metal ions

	ΔS	Δr/Å
Fe(II)	2	0.14–0.24
Fe(III)	2	0.11–0.16
Co(II)	1	0.09–0.11

ΔS, change of spin; Δr, change of bond length solutions. In the latter case, the molar fraction of complex molecules in the HS state as a function of temperature $x_{HS}^{(T)}$ always follows a simple Boltzmann distribution law for the two states. In the solid state, however, the situation is different. Interactions between the spin-state-changing metal complexes themselves as well as the complex molecules and the lattice may become very effective, leading to different shapes of $x_{HS}^{(T)}$ curves, as schematically represented in Fig. 6: (a) gradual, (b) abrupt, (c) with hysteresis, (d) plateau(x), reflecting two (or more) stepped transitions, and (e) a transition with a residual HS fraction at low temperatures.

In view of potential solid-state applications, abrupt and complete spin transitions exhibiting a wide hysteresis around room temperature would be of great interest [15, 16]. In the following we will review and discuss the state of the art for spin transitions, as measured against the abovementioned criteria.

Room-temperature spin transition systems

Iron(II)–triazole complexes

Most of the known room-temperature ST compounds reported to date are derived from the 1,2,4-triazol (trz) ligand system (Fig. 7a). Structurally, these complexes consist of linear chains in which the Fe(II) ions are linked by triple *N*1,*N*2-1,2,4-triazole bridges (Fig. 7b). A series of iron(II) coordination polymers of 4-octadecyl-1,2,4-triazole have been synthesized and their spin transition properties have been investigated thoroughly [17, 18]. Thus, the introduction of the tosylate counteranion led to a sharp spin transition close to room temperature ($T_{1/2} \sim 300$ K) with a rather large hysteresis of ca. $\Delta T_{1/2} = 15$ K (vide infra). It is interesting to note that water has been found to be a good solvent for the synthesis of iron(II)–triazole coordination polymers. Generally, these complexes are highly cooperative and counteranion exchange has been proven to be a versatile way to fine-tune the spin transition temperature.

Kahn et al. [19] reported the spin transition properties of the compound $\{[Fe^{II}(Htrz)_2(trz)]\}_n(BF_4)_n$ and $\{[Fe^{II}(Htrz)_3]\}_n(BF_4)_{2n}\cdot(H_2O)_n$, (where Htrz and trz$^-$ are the protonated and deprotonated forms of 1,2,4-triazolatole). The ST of the first compound, $\{[Fe^{II}(Htrz)_2(trz)]\}_n(BF_4)_n$, is strongly dependent on the way that it is synthesized. In a water/ethanol mixture, a polymorph $\{[Fe^{II}(Htrz)_2(trz)]\}_n(BF_4)_n$ (**A**) was prepared that exhibited a very abrupt spin transition centred around 360 K with a thermal hysteresis of 50 K, while the polymorph$\{[Fe^{II}(Htrz)_2(trz)]\}_n(BF_4)_n$ (**B**) prepared in pure methanol leads to a smoother transition with a reduced hysteresis width. The spin transition parameters of polymorph **A** also depend strongly on the number of temperature cycles: during the first temperature cycle, polymorph **A** shows STs at $T_{1/2\downarrow} = 345$ K and $T_{1/2\uparrow} = 385$ K (up and down), while $T_{1/2\uparrow}$ is progressively shifted toward higher temperatures during the following four cooling–heating cycles, finally reaching a hysteresis loop of 50 K (Fig 8a). This behaviour was explained by a sort of “running in” of the material. The magnetic behaviour of polymorph **B** exhibits a less abrupt ST with a hysteresis loop width of ca. 50 K.

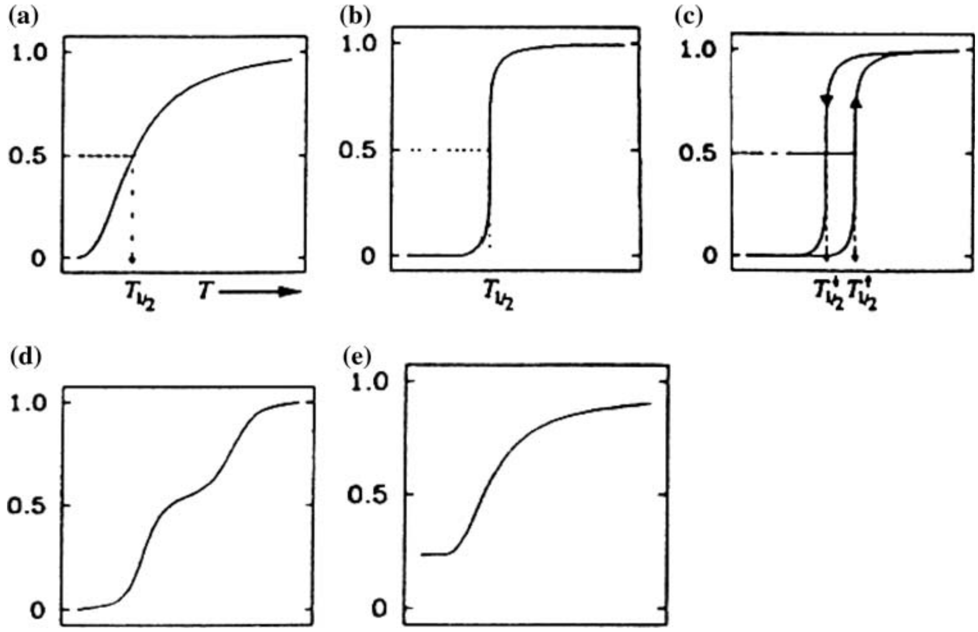

Fig. 6 Various types of spin state transition curves: gradual (**a**), abrupt (**b**), with hysteresis (**c**), two-step transition (**d**), and incomplete (**e**)

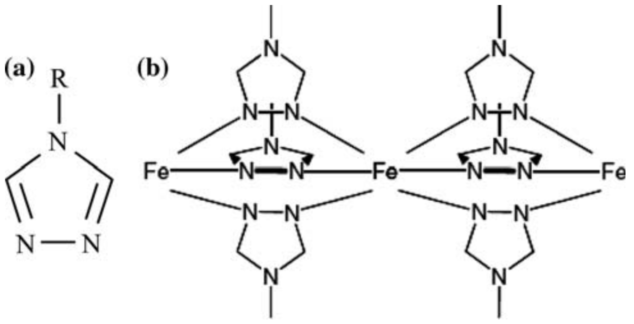

Fig. 7 The molecular structures of **a** the R-trz ligand and **b** the coordination polymer chain $\{[Fe^{II}(R\text{-}trz)_3]^{2+}\}_n$, with trz = 1,2,4-triazole and R representing different substituents

Again, successive thermal cycles modify the ST parameters for this polymorph, and the width of the thermal hysteresis loop is reduced by more 50% after three cycles (Fig. 8b).

In contrast, compound $\{[Fe^{II}(Htrz)_3]\}_n(BF_4)_{2n}\cdot(H_2O)_n$ was found to undergo an $\alpha \leftrightarrow \beta$ phase transition around 420 K, whereby the two phases exhibit different ST behaviours. The α phase shows a rather abrupt spin transition centred around 335 K with a thermal hysteresis of $\Delta T_{1/2} = 22$ K. The β phase is metastable at room temperature and shows an abrupt ST around room temperature with a hysteresis of $\Delta T_{1/2} = 6$ K (Fig. 9). The water-free compound $\{[Fe^{II}(Htrz)_3]\}_n(BF_4)_{2n}$ exhibits a less abrupt ST with a smaller hysteresis compared to its hydrated equivalent.

Nanoparticles of $\{[Fe^{II}(Htrz)_2(trz)]\}_n(BF_4)_n$ have been prepared by the reverse micelle technique [20]. Transmission electron microscopy (TEM) images show that the average nanoparticle size is below 20 nm. The clear deep-purple suspensions of these nanoparticles in *n*-octane are stable for weeks. In addition, the solid produced by controlled evaporation of the solvent can be resuspended to yield a bright transparent suspension. This suspension does indeed turn light pink when heated up, maintaining this colour until it cools down below 70 °C. Both colours, each

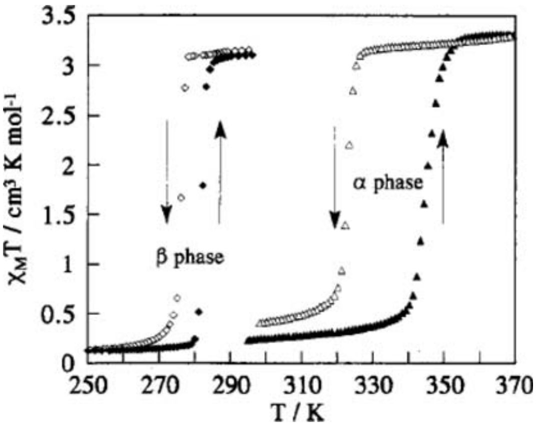

Fig. 9 The magnetic properties of two different crystalline phases (α and β) of the coordination polymer $\{[Fe^{II}(Htrz)_3]\}_n(BF_4)_{2n}\cdot(H_2O)_n$

associated with the high- and low-spin states, respectively, are stable for a wide range of temperatures. A suspension of $\{[Fe^{II}(Htrz)_2(trz)]\}_n(BF_4)_n$ nanoparticles was dried by removing the solvent in vacuum, and magnetic measurements were performed on the solid residue. It was shown that the spin transition of the nanoparticles is clearly preserved in the solid state, and it remains almost identical to that reported for bulk samples. The transition is very abrupt, rendering a well-shaped thermal hysteresis loop over 40 K (Fig. 10).

It was also shown that slight modifications of the synthetic procedure (e.g. different ratios of solvent, water, and surfactants) lead to different micelle sizes, which affect the sizes of the particles and their ST properties. The critical temperatures can be lowered towards room temperature by changing the composition of the nanoparticles by doping the $\{[Fe^{II}(Htrz)_2(trz)]\}_n(BF_4)_n$ nanoparticles with 20% Zn(II) metal ions.

The syntheses and spin transition properties of the compounds $\{[Fe(Htrz)_3]\}_2(ClO_4)_{2n}$ and $\{[Fe(Htrz)_{3-3x}(4\text{-}NH_2trz)_{3x}]\}_n(ClO_4)_{2n}\cdot nH_2O$ (Htrz = 1,2,4-tiazole, 4-NH_2trz = 4-amino-1,2,4-triazole) have been reported [21]. The

Fig. 8 The magnetic properties of the two polymorphs of the coordination polymer $\{[Fe^{II}(Htrz)_2(trz)]\}_n(BF_4)_n$. **a** Representation of the $\chi_M T$ versus T plot of the first cooling/heating cycle of polymorph (**A**) (prepared from an ethanol/water solution), and **b** the first three cycles of the respective $\chi_M T$ versus T plots of polymorph (**B**) prepared from a methanol solution

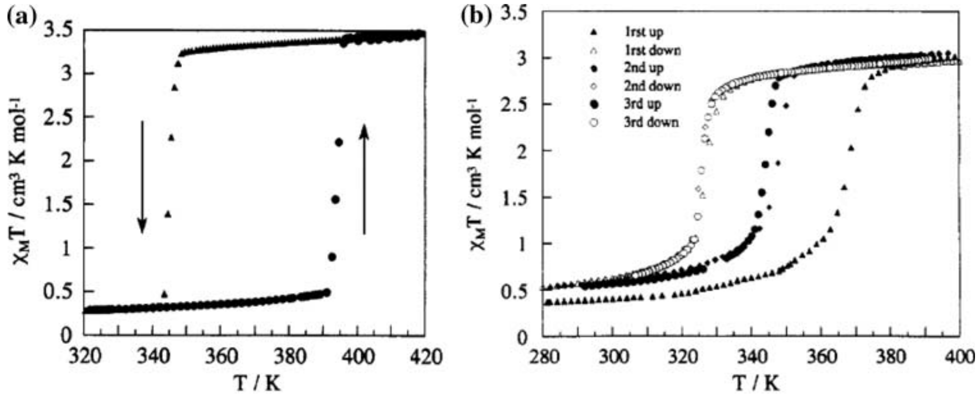

$\{[Fe^{II}(Htrz)_2(trz)]\}_n(BF_4)_n$ **(A)**

$\{[Fe^{II}(Htrz)_2(trz)]\}_n(BF_4)_n$ **(B)**

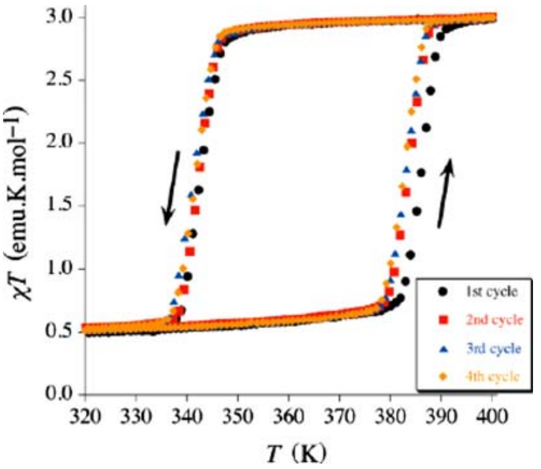

Fig. 10 Representation of the first four cooling/heating cycles of the $\chi_M T$ versus T plot of 20 nm $\{[\mathrm{Fe^{II}(Htrz)_2(trz)}]\}_n(\mathrm{BF_4})_n$ nanoparticles, demonstrating the stability of the thermal hysteresis

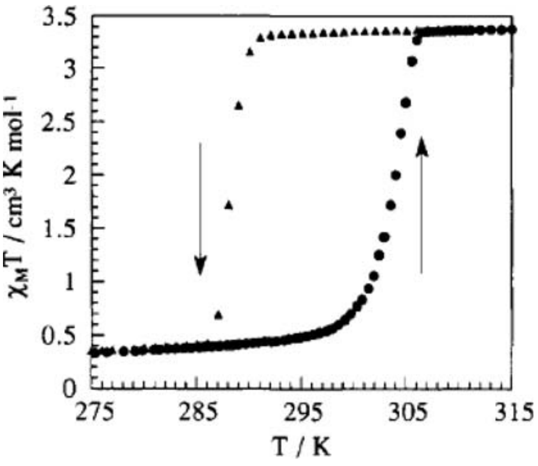

Fig. 11 The $\chi_M T$ versus T plot for $\{[\mathrm{Fe^{II}(Htrz)_{3-3x}(4\text{-}NH_2trz)_{3x}}]\}_n(\mathrm{ClO_4})_{2n}\cdot n\mathrm{H_2O}$, for $x = 0.05$, exhibiting an ST with a wide hysteresis around room temperature

perfectly dry perchlorate analogue, $\{[\mathrm{Fe(Htrz)_3}]\}_n(\mathrm{ClO_4})_{2n}$, shows a rather smooth ST around 265 K with a weak hysteresis of about 5 K. When a drop of water is added to 50 mg of $\{[\mathrm{Fe(Htrz)}]\}_n(\mathrm{ClO_4})_{2n}$, the transition becomes very abrupt in the warming and cooling modes, with $T_{1/2(\uparrow)} = 313$ K and $T_{1/2(\downarrow)} = 296$ K. The water most likely to creates hydrogen bonds which increase the cooperation between the iron(II) centres. The ST is accompanied by an intense change in colour from purple to white. The hysteresis loop is just above room temperature and can be shifted by ligand doping with the 4-$\mathrm{NH_2}$trz ligand. Since the compound $\{[\mathrm{Fe(4\text{-}NH_2trz)}]\}_2(\mathrm{ClO_4})_{2n}$ shows a smooth transition around centred around 130 K, the authors expected that the ST properties could be controlled by mixing of 4-$\mathrm{NH_2}$trz and Htrz ligands. Consequently, the magnetic properties of the material $\{[\mathrm{Fe(Htrz)_{3-3x}(4\text{-}NH_2trz)_{3x}}]\}_n(\mathrm{ClO_4})_{2n}\cdot n\mathrm{H_2O}$ were investigated for compositions $0 \leq x \leq 0.1$, and the authors found the dependences $T_{1/2(\uparrow)} = 313 - 180x$ and $T_{1/2(\downarrow)} = 296 - 160x$. At $x = 0.05$, the transition occurs with hysteretic branches above and below room temperature, with $T_{1/2(\downarrow)} = 288$ K and $T_{1/2(\uparrow)} = 304$ K (Fig. 11).

Kahn et al. [22] reported the spin transition properties of the compound $\{[\mathrm{Fe^{II}(4\text{-}NH_2trz)_3}]\}_n(\mathrm{tos})_{3n}\cdot 2\mathrm{H_2O}$, (tos = tosylate anion) under hydrated and dehydrated conditions. The hydrated form exhibits an abrupt spin transition in the warming regime at 361 K accompanied by the removal of the two noncoordinated water molecules. Cooling the dehydrated compound, $\{[\mathrm{Fe(NH_2trz)_3}]\}_n(\mathrm{tos})_{3n}$, causes a slightly smoother spin transition at 279 K. In the presence of humidity, and at room temperature (293 K), the white $\{[\mathrm{Fe^{II}(4\text{-}NH_2trz)_3}]\}_n(\mathrm{tos})_{3n}$ transforms back into the violet hydrated phase. The dehydration allowed the isolation of a system with an exceptionally large thermal hysteresis loop of ca. 80 K. Historically, the $\{[\mathrm{Fe^{II}(NH_2trz)_3}]\}_n(\mathrm{tos})_3\cdot 2\mathrm{H_2O}$–$\{[\mathrm{Fe^{II}(NH_2trz)_3}]\}_\mathrm{n}(\mathrm{tos})_{3\mathrm{n}}$ couple was one of the first examples of spin transition materials with a large hysteresis that exhibited up and down branches below and above room temperature.

The polymeric compound $\{[\mathrm{Fe^{II}(4\text{-}NH_2trz)_3}]\}_n(\mathrm{NO_3})_{2n}$ (with $\mathrm{NH_2}$trz = 4-amino-1,2,4-triazole) was characterised and studied by optical response and electron spin resonance using $\mathrm{Cu^{2+}}$ and $\mathrm{Mn^{2+}}$ as dopants and paramagnetic probes [23]. In all of the doped samples the spin transition of $\mathrm{Fe^{2+}}$ ions was characterised by a pronounced thermochromic effect between a bright pink colour (LS state) and chalky white colours (HS state), so the ST could be detected optically. It was seen that doping with copper does not affect $T_{1/2(\downarrow)}$, while the stabilised $T_{1/2(\uparrow)}$ value is more sensitive to doping. By changing the amount of dopant from 10 to 1%, the hysteresis loop for the Cu/Fe-doped sample shifts its centre from 312 to 307 K. Simultaneously, the hysteresis loop narrows from 36 K down to 28 K and the ST becomes less abrupt. Doping the same compound with manganese(II) has a more pronounced effect upon the characteristics of the hysteresis loop, which dramatically narrows over the course of the first three thermal cycles (from 41 K to a stabilized value of 21 K). Finally, the hysteresis loop $\Delta T_{1/2}$ narrows and $T_{1/2}$ shifts to a lower temperature with increasing manganese(II) doping level.

Further anion exchange generated a series of iron(II) spin transition compounds of general formula $\{[\mathrm{Fe^{II}(4\text{-}NH_2trz)_3}]\}_n\mathrm{X}_{2n}\cdot x\mathrm{H_2O}$ (X = 1-naphthalene sulfonate, 2-naphthalene sulfonate, 4-hydroxy-1-naphthalenesulfonate, 4-amino-1-naphthalene sulfonate, 6-hydroxy-2-naphthalene sulfonate), and the ST properties of these were investigated in relation to the nature of the anion involved

[24]. These compounds are isostructurally linear chains in which iron(II) ions are linked by N^1,N^2 of 1,2,4-triazole bridges, while the noncoordinating anions of naphthalene sulfonate type mediate interchain interactions. The physical properties of these compounds can be understood by the synergy between the Fe(II) spin transition behaviour and by the dehydration–hydration process for interstitial water solvent molecules. In terms of room-temperature ST, the compound involving the 2-naphthalene sulfonate anion delivers a temperature-induced hysteresis centred at 290 K and with a 14 K hysteresis width. A further series of iron(II) ST compounds of general formula $\{[\mathrm{Fe}^{\mathrm{II}}(\mathrm{hyetrz})_3]\}_n(\mathrm{X})_{2n}$ $x\mathrm{H_2O}$, where hyetrz = 4-(2′-hydroxyl-ethyl)-1,2,4-triazole and X = Cl^-, $\mathrm{NO_3}^-$, Br^-, I^-, $\mathrm{BF_4}^-$, $\mathrm{ClO_4}^-$ and $\mathrm{PF_6}^-$, have been prepared [25]. Here, the ST is strongly associated with the removal of lattice water molecules, which initially stabilize the low-spin state. However, after dehydration, the perchlorate and iodide variants show clearly increased transition temperatures. In general, a correlation where the transition temperature $T_{1/2}$ increased with increasing anion radius was found. For example, in $\{[\mathrm{Fe}^{\mathrm{II}}(\mathrm{hyetrz})_3]\}_n(\mathrm{I})_{2n}$, the ST temperature $T_{1/2}$ gets very close to room temperature, and is accompanied by a thermal hysteresis of 12 K centred in the vicinity of room temperature (291 K). Thus, $\{[\mathrm{Fe}^{\mathrm{II}}(\mathrm{hyetrz})_3]\}_n(\mathrm{I})_{2n}$ represents one of the very few iron(II) spin transition materials to show a spin transition with hysteresis and to be associated with thermochromic effects in the close vicinity of room temperature.

The synthesis, structural characterisation, Mössbauer study and magnetic properties of a trinuclear iron(II) compound containing the hyetrz ligand, $[\mathrm{Fe}^{\mathrm{II}}_3(\mathrm{hyetrz})_3(\mathrm{H_2O})_6]$ $(\mathrm{CF_3SO_3})_6$, were reported by Gütlich et al. [26]. Single-crystal X-ray structure analysis carried out at two different temperatures (120 and 330 K) revealed that the central iron Fe1 was coordinated with six 4-(2′-hydroxyl-ethyl)-1,2,4-triazole nitrogens, and the two peripheral equivalent irons, Fe2 and Fe2′, had coordination polyhedra that contained three hyetrz nitrogens and three water oxygens (Fig. 12a). Hydrogen bonding through the oxygen atoms of the $\mathrm{SO_3}$ groups of the triflate anions links to the coordinated water molecule, and these anions are also linked by hydrogen bonding to the hydroxyl groups of the ethyl chain in the 4-position of each triazole ligand. The bond distances of the central iron Fe1 change with temperature, indicating a LS state at 120 K and a HS state at 330 K. However, the bond lengths of the Fe2 and Fe2′ polyhedra remain constant with temperature and are typical of the HS state of iron(II).

Magnetic measurements reveal a gradual ST behaviour which crosses the room temperature regime. In the temperature range 77–235 K, the χT value is constant and equal to 7.4 emu K mol^{-1}, which corresponds with two HS iron(II) centres and confirms predictions from the X-ray structure at low temperature. Above 240 K the magnetic moment increases with temperature, and at 360 K it reaches the value 10.92 emu K mol^{-1}, which is in accordance with the situation where there are three iron(II) HS centres per molecule. In conclusion, the compound $[\mathrm{Fe}^{\mathrm{II}}_3(\mathrm{hyetrz})_3(\mathrm{H_2O})_6](\mathrm{CF_3SO_3})_6$ can be considered an oligomeric equivalent of the Fe(II) triazole coordination polymer family, for which a full single-crystal X-ray data analysis is yet to be reported. Miller et al. [27] reported the synthesis and variable-temperature infrared and magnetic studies of the mononuclear compound $[\mathrm{Fe}(\mathrm{HB}(\mathrm{C_2H_2N_3})_3)_2]^0$ $(\mathrm{HB}(\mathrm{C_2H_2N_3})_3$ = bis[hydrotris(1,2,4-triazol-1-yl)borate](−)) (Fig. 13a). The variable-temperature (4–350 K) magnetic susceptibility measurements showed an abrupt ST between the LS $S = 0$ to the HS $S = 2$ states, centred at 331 K with a thermal hysteresis of 1.5 K (Fig. 13b). Variable-temperature FTIR spectra between 300 and 360 K in both heating and cooling modes revealed that there were no differences between the spectra recorded at identical temperatures, implying that no thermal hysteresis effect was detected. However, several vibrations show dramatic modifications in intensity and frequency upon ST, proving that changes in distant nonmetal–ligand vibrations can be used to monitor the ST behaviour.

Hoffman-type pyrazine networks

In 2001, the research group of Real et al. [28] reported on bimetallic coordination complexes of the general formula

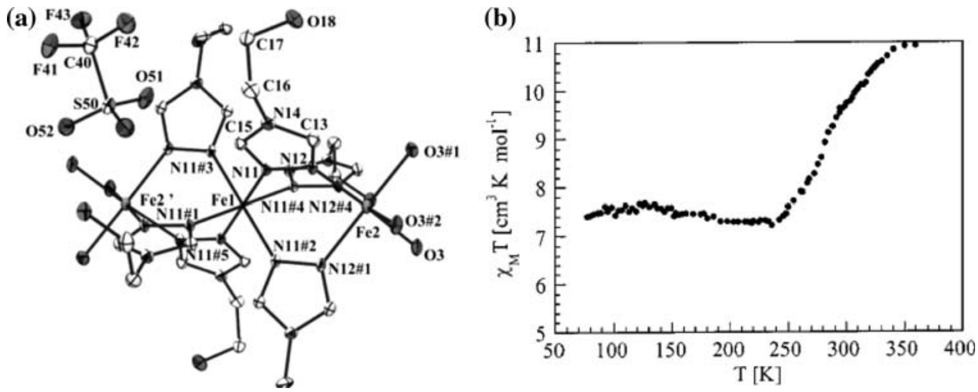

Fig. 12 The crystal structure (**a**) and magnetic properties (**b**) of the compound $[\mathrm{Fe}^{\mathrm{II}}_3(\mathrm{hyetrz})_3(\mathrm{H_2O})_6](\mathrm{CF_3SO_3})_6$

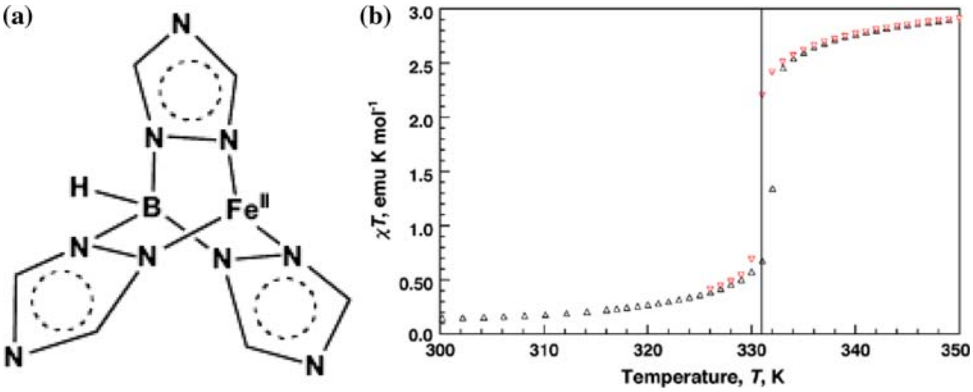

Fig. 13 **a** The proposed coordination of the $HB(C_2H_2N_3)_3(-)$ ligand, and **b** the magnetic properties of the complex $[Fe\{HB(C_2H_2N_3)_3\}_2]^0$

$\{[Fe^{II}(pz)M^{II}(CN)_4]\}_n \cdot xH_2O$ (pz—pyrazine, CN—cyano, M = Ni, Pd, Pt). With respect to room temperature ST, the compound $\{[Fe^{II}(pz)][Pt^{II}(CN)_4]\}_n \cdot xH_2O$ ($x = 0$, 2) exhibits interesting properties. The single-crystal X-ray diffraction study of this analogue (Fig. 14a) revealed two-dimensional sheets of iron–tetracyanoplatinum moieties, which are interconnected via Fe^{II}-pyrazine linkers to a 3D network. Magnetic measurements of this compound reveal ST ($T_{1/2(\downarrow)} = 220$ K and $T_{1/2(\uparrow)} = 240$ K) with strong hysteretic behaviour ($\Delta T_{1/2} = 20$ K). In a more recent paper, Bousseksou et al. [29] describe the dependence of the ST of the same compound on the presence of interstitial water molecules. Note that the dehydrated form exhibits improved spin transition behaviour, exhibiting a more complete ST that is closer to room-temperature. Moreover, the hysteresis loop becomes wider ($\Delta T_{1/2} = 24$ K), rather square-shaped, and reproducible over several cycles (Fig. 14b).

Additionally, and for the first time, reversible light-induced LS ↔ HS one-shot laser excitation within the area of the hysteresis loop was reported. This is of fundamental importance, because in contrast with light-induced spin-state trapping (LIESST), this experiment even works at room temperature, and does not show thermal relaxation from HS to LS. The metastable HS or LS states have infinite lifetimes in the thermal hysteresis loop region, which may give access to switching behaviour that could be exploited in molecular hybrid device setups [29].

Room-temperature ST behaviour with hysteresis is also observed for the nickel analogue of the 3D Hoffman-type pyrazine network, $\{[Fe^{II}(pz)][Ni^{II}(CN)_4]\}_n \cdot 2H_2O$, but the transition is not so abrupt and the hysteresis is smaller ($T_{1/2(\downarrow)} = 280$ K and $T_{1/2(\uparrow)} = 305$ K) than for the previous compound [28].

With respect to the aim to use spin transition compounds in the field of memory storage devices, Hoffman-type pyrazine networks are excellent candidates for potential applications due to their unique combination of (1) abrupt spin transitions with (2) wide thermal hysteresis loops that are (3) centred on the room-temperature region. Furthermore, Cobo et al. [30] studied the surface-assisted creation of multilayers of this class of ST compounds. The first monolayer cycle was obtained from a mercaptopyridine surface link (Fig. 15a, step 1), while the conventional pyrazine ligand was used during subsequent cycles. Alternating coordination sequences of iron(II) ions/ $[Pt^{II}(CN)_4]^{2-}$/pyrazine finally led to an architecture of a few multilayers of water-free $\{[Fe^{II}(pz)Pt^{II}(CN)_4]\}_n$ on a gold substrate (Fig. 15a, step 2–4). The ST properties of the assembled thin films were subsequently studied by

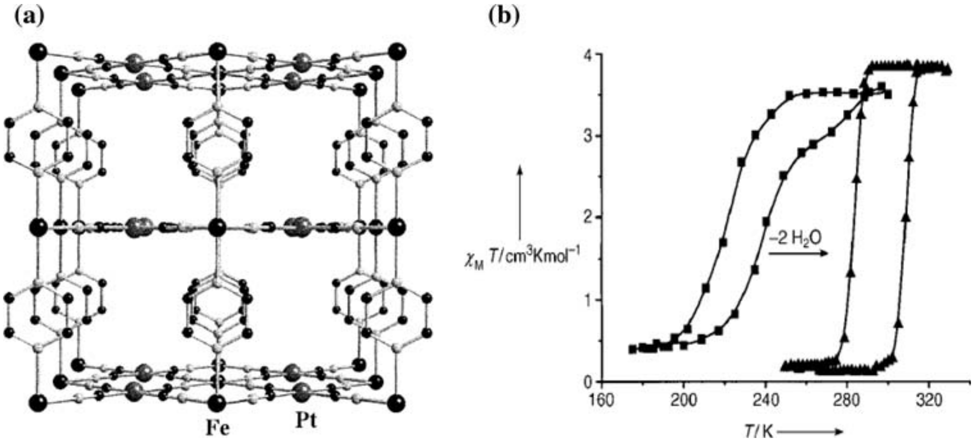

Fig. 14 **a** The crystal structure of the 3D Hoffman-type pyrazine network of $\{[Fe(pz)Pt(CN)_4]\}_n$, and **b** a representation of the solvent dependency of the ST properties of $[Fe(pz)Pt(CN)_4] \cdot 2H_2O$ in the $\chi_M T$ versus T plot

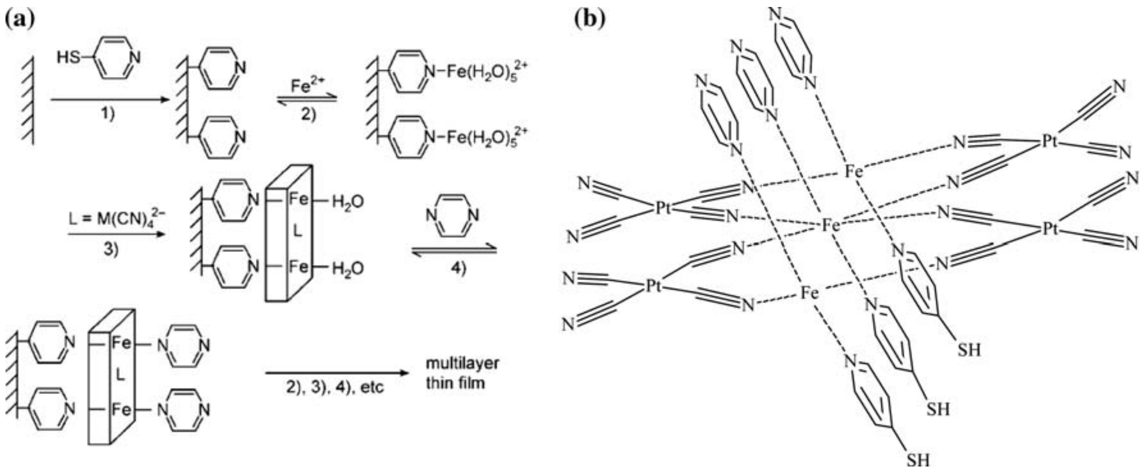

Fig. 15 **a** Sequential surface assembly of Hoffman-type multilayer [Fe(pz)Pt(CN)$_4$]: *1*, monolayer of mercaptopyridine; *2*, coordination of [Fe(H$_2$O)$_6$](BF$_4$)$_2$; *3*, two-dimensional networking with [Pt(CN)$_4$]$^{2-}$; *4*, assembly of pyrazine; **b** schematic representation of the molecular structure of the first layer of {[Fe(pz)Pt(CN)$_4$]}$_n$ on the gold surface

variable-temperature Raman spectroscopy. The Raman spectra of both a powder sample and the multilayer were measured at several temperatures in the cooling and heating cycles. The powder sample reveals a hysteresis loop width of 25 K centred around 290 K, corresponding closely to the magnetic susceptibility measurements (Fig. 16a). The multilayer sample displays a hysteresis loop centred around 310 K, also showing a hysteresis width of 25 K. However, the ST in the multilayers is much less abrupt and the square shape of the hysteresis loop has completely vanished (Fig. 16b). The authors normalized the Raman intensity by the formula $I(\text{norm}) = I(1{,}025\ \text{cm}^{-1})/I(1{,}230\ \text{cm}^{-1})$, since the modes at 1,025 and 1,230 cm^{-1} have the highest intensity, but other Raman markers provided comparable results (Fig. 16c).

The ST behaviour of nanoparticles made from Hoffman-type pyrazine networks was reported by Larionova et al. [31, 32]. The authors studied [Fe$^{\text{II}}$(pz)]$^{2+}$/[Ni$^{\text{II}}$(CN)$_4$]$^{2-}$/chitosan composite beads (Fig. 17) and determined the magnetic properties of the obtained material at fields of 1 T. The results revealed incomplete STs ($T_{1/2(\downarrow)} = 220$ K and $T_{1/2(\uparrow)} = 240$ K) for this kind of nanoparticle, and a 10 K thermal hysteresis width. Variable-temperature Mössbauer investigations confirmed the loss of ST completeness in the nanoparticle material. Obviously, only one-third of all iron(II) ions undergo ST, while two-thirds remain in the LS state at any temperature. The huge thermally inactive fraction can be related the high surface area to volume ratios of these tiny nanoparticles (3–5 nm), since 60–70% of the iron atoms are localized at the surface. Thus, the majority of the iron(II) centres in the nanoparticles experience a strongly modified coordination environment; and this situation leads to ST loss due to inappropriate ligand field strengths.

In addition to the abovementioned 3D structures, two isostructural compounds expressing 2D coordination polymer networks of the formula {[Fe$^{\text{II}}$(3-Xpy)$_2$Ag$^{\text{I}}$(CN)$_2$][Ag$^{\text{I}}$(3-Xpy)(CN)$_2$]}$_n$·3-Xpy (py = pyridine; X = Br, I) were reported [33]. These compounds create 2D corrugated layers, and the ST is situated in both cases close to room temperature (e.g. for X = I exhibiting a thermal hysteresis, $T_{1/2(\downarrow)} = 261$ K and $T_{1/2(\uparrow)} = 275$ K). In the bromo analogue, ST is only observed in the heating mode ($T_{1/2} = 306$ K); the compound remains blocked in the HS state during the subsequent cooling mode.

Iron(II) bis(pyrazol)pyridine complexes

Halcrow et al. [34–37] reported a mononuclear iron(II) complex which contains the tridentate *N* donor ligand 2,6-bis(pyrazol-1-yl)pyridine (1-bpp) in the molecular formula [Fe(1-bpp)$_2$](BF$_4$)$_2$ (Fig. 18). This compound shows an unusually abrupt spin transition centred somewhat below room temperature ($T_{1/2} = 259$ K) and possessing a mere 3 K thermal hysteresis. This ST is accompanied by significant thermochromism, with dark brown and mustard yellow colours indicating the LS and the HS states, respectively.

Systematic substitution in the 4′-position of the pyridine ring of the bpp ligand has been shown to be a useful tool since it increases the spin transition temperatures until they get close to room temperature (Fig. 19) [15, 38–40]. Thus, the introduction of a *para*-pyridyl substituent leads to the linear interconnection of the mononuclear iron(II) complexes into a chainlike hydrogen-bonding polymer {[Fe$^{\text{II}}$(1-bpp-4-py-H$^+$)(bpp-4-py)]}$_n$(ClO$_4$)$_{3n}$·(CH$_3$OH)$_n$ (Fig. 20a, c) [38] (1-bpp-4-py = 2,6-bis(pyrazol-1-yl)-4,4′-bipyridine, see Fig. 19a). The interconnecting

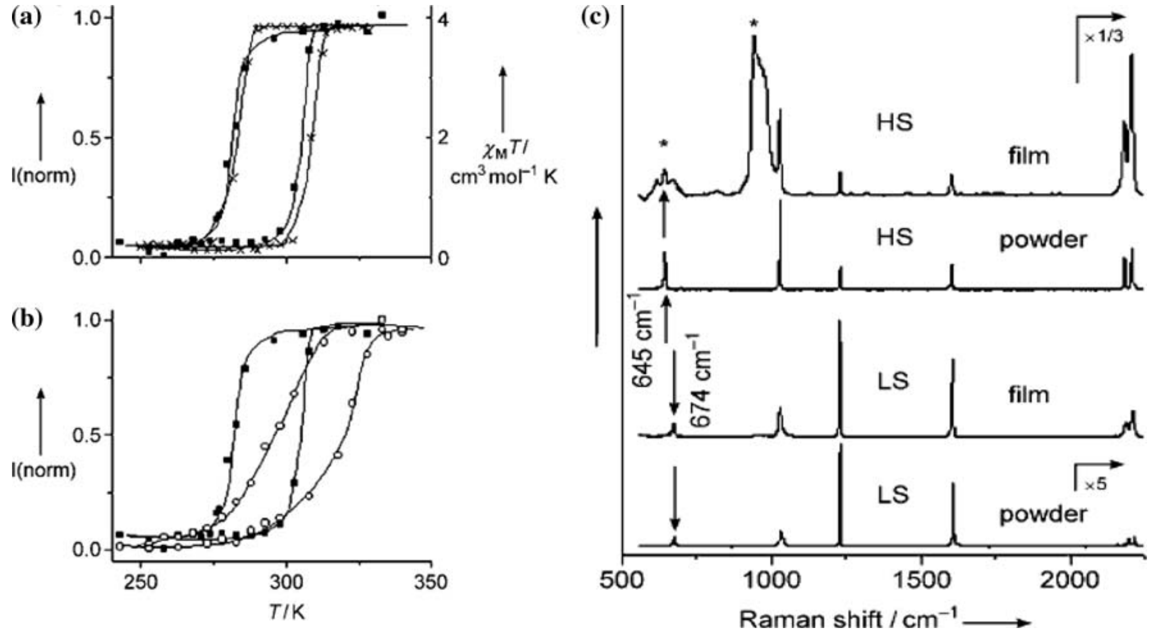

Fig. 16 **a** Comparison of the ST behaviours of the powder sample via SQUID measurements (*crosses*) and variable-temperature Raman spectroscopy (*filled squares*); **b** comparison of the ST behaviours of the powder sample (*filled squares*) and the multilayer film (*circles*), both obtained by variable-temperature Raman spectroscopy; **c** Raman spectra of the powder sample and the multilayer film at the HS (295 K) and LS (125 K) states (chosen modes at 1,025, and 1,230 cm^{-1}; I(norm) = I(1,025 cm^{-1})/I(1,230 cm^{-1}))

Fig. 17 **a** Schematic representation of the preparation of nanoparticles of the Hoffmann-type $[Fe^{II}(pz)]^{2+}$/$[Ni^{II}(CN)_4]^{2-}$/chitosan composite, and **b** diagram showing their magnetic behaviour

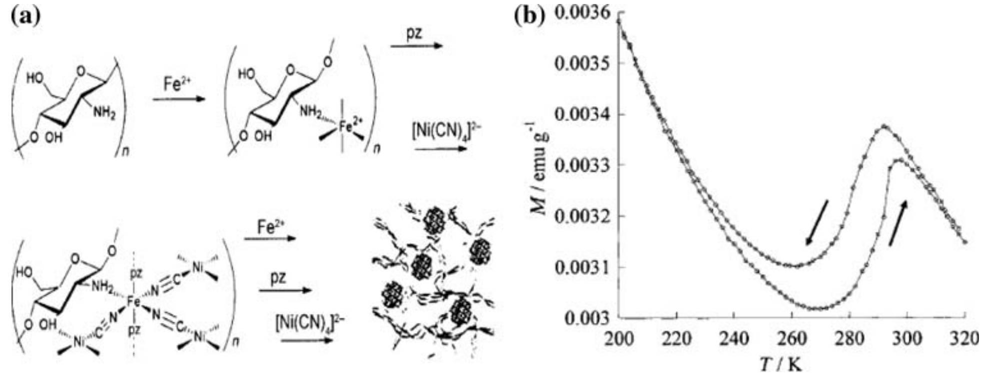

Fig. 18 The single-crystal structure and magnetic properties of $[Fe(1\text{-}bpp)_2](BF_4)_2$, $T_{1/2} = 259$ K, $\Delta T_{1/2} = 3$ K

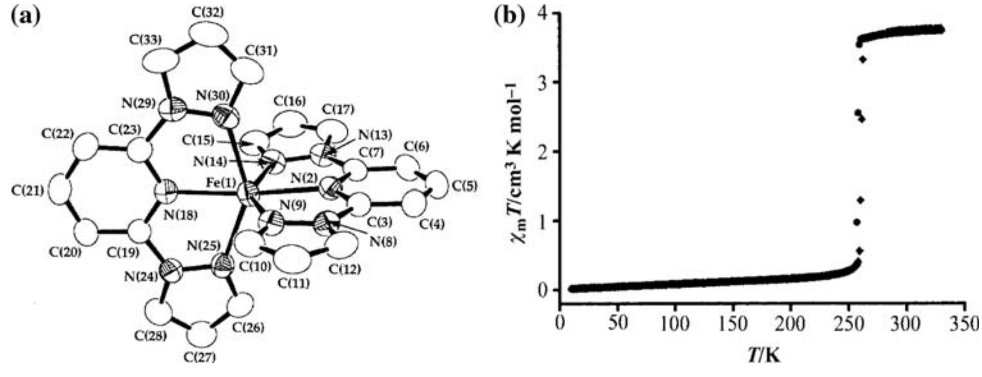

hydrogen bonds are performed by the semi-protonation of the *para*-pyridine nitrogens of the ligand 1-bpp-4-py, forming pyridinium cations that allow self-complementary N$^+$-H ···N hydrogen bonds together with deprotonated pyridines of neighbouring complex units, resulting in infinite one-dimensional chains of mononuclear ST Fe(II) centres. The ST of this 1D polymer, which is centred exactly at room temperature, is accompanied by a 2 K

Fig. 19 Molecular structures of different 2,6-bis(pyrazol-*n*-yl)pyridine-type ligands ($n = 1$ or 3)

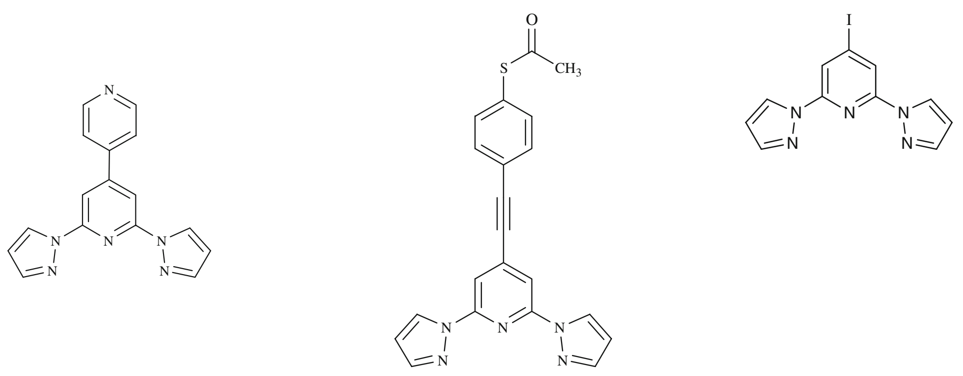

(a) 1-bpp-4-py **(b)** 1-bpp-4-acety-ph-SAc **(c)** 1-bpp-4-I

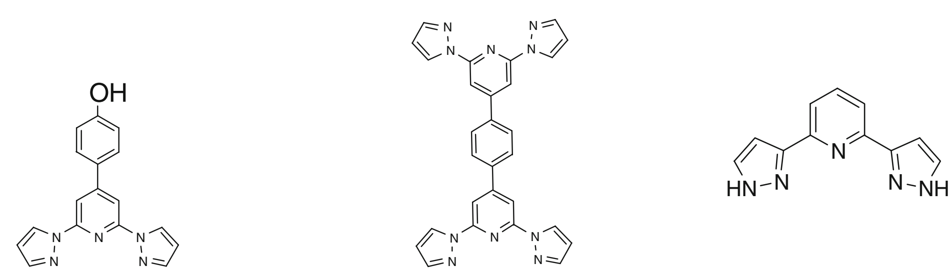

(d) 1-bpp-4-ph-OH **(e)** 1-bpp-ph-1-bpp **(f)** 3-bpp

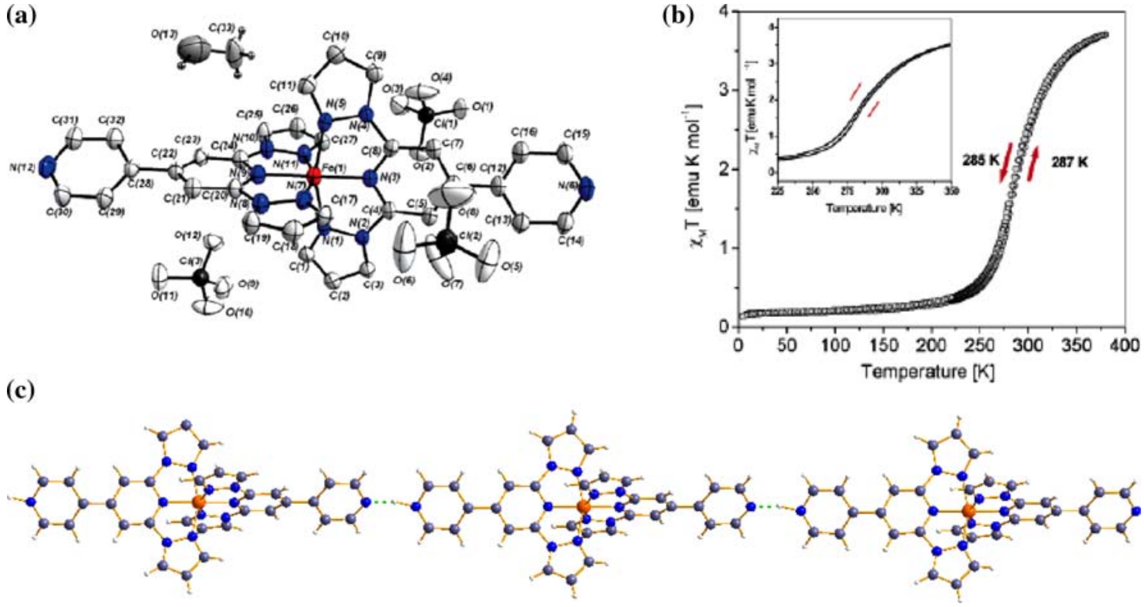

Fig. 20 **a** Representations of the single-crystal X-ray structure, **b** the magnetic behavior, and **c** the supramolecular 1D structure of compound $\{[\mathrm{Fe^{II}}(\text{1-bpp-4-py-H}^+)(\text{1-bpp-4-py})]\}_n(\mathrm{ClO_4})_{3n}\cdot(\mathrm{CH_3OH})_n$

hysteresis ($T_{1/2(\downarrow)} = 285$ K; $T_{1/2(\uparrow)} = 287$ K), and demonstrates the existence of a significant degree of cooperation mediated by hydrogen bonds and/or by the methanol molecules trapped in the lattice (Fig. 17b). The zero-field ^{57}Fe Mössbauer spectra of the powdered sample was obtained at several temperatures, and no discernible differences between the cooling and heating modes were discerned; the room-temperature ST of the sample was also confirmed.

In the same vein, a ST iron(II) complex incorporating the ligand 1-bpp-4-acety-ph-SAc (*S*-(4-{[2,6-(bispyrazol-1-yl)pyrid-4-yl]ethynyl}-phenyl)ethanethioate; see Fig. 19b)

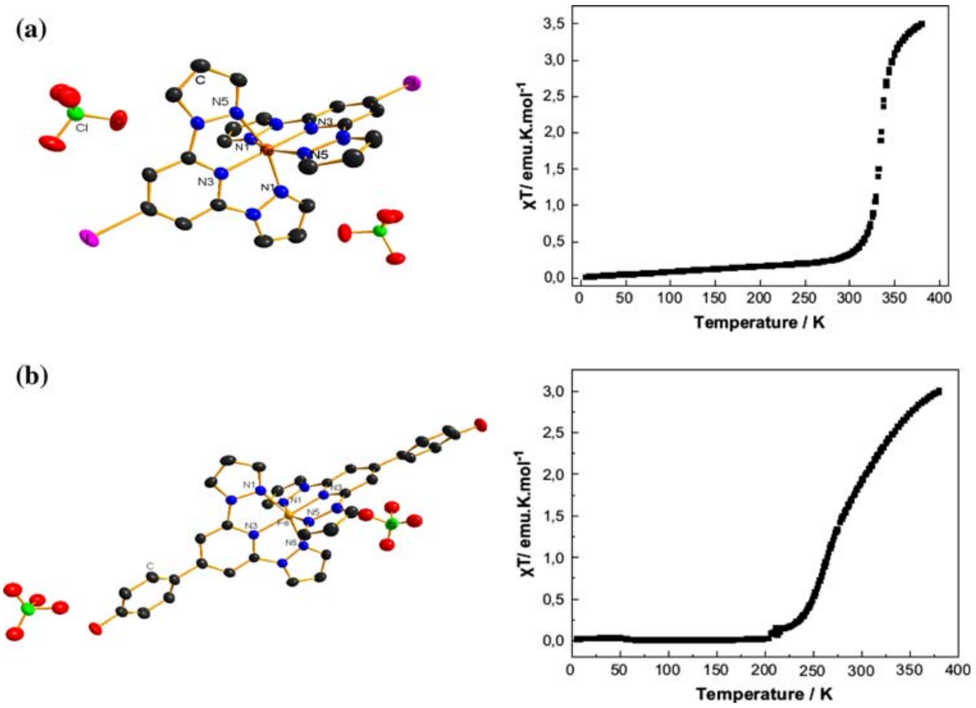

Fig. 21 The single-crystal X-ray structures and magnetic properties of the compounds **a** $[\mathrm{Fe^{II}(1\text{-}bpp\text{-}4\text{-}I)_2}](\mathrm{ClO_4})_2$ and **b** $[\mathrm{Fe^{II}(1\text{-}bpp\text{-}4\text{-}ph\text{-}OH)_2}](\mathrm{ClO_4})_2$

was reported recently [39]. The ST of the resulting mononuclear compound $[\mathrm{Fe^{II}(1\text{-}bpp\text{-}4\text{-}acety\text{-}ph\text{-}SAc)_2}](\mathrm{ClO_4})_2$ is situated very close to room temperature ($T_{1/2(\downarrow)} = 273$ K; $T_{1/2(\uparrow)} = 281$ K). The appearance of thermal hysteresis ($\Delta T_{1/2} = 8$ K) is attributed to intermolecular hydrogen-bonding interactions and sulfur–sulfur contact for acetyl-protected thiol end-groups. Further substitutions elucidate the influence of the nature of the 4-substituents on the ST temperature. The iodo analogue, $[\mathrm{Fe^{II}(1\text{-}bpp\text{-}4\text{-}I)_2}](\mathrm{ClO_4})_2$ (1-bpp-4-I = 4-iodo-2,6-bis(pyrazol-1-yl)pyridine; see Fig. 19c), shows an abrupt spin transition at $T_{1/2} = 333$ K, while the 4-hydroxy phenyl group causes the ST in $[\mathrm{Fe^{II}(1\text{-}bpp\text{-}4\text{-}ph\text{-}OH)_2}](\mathrm{ClO_4})_2$ (1-bpp-4-ph-OH = 4-(4-hydroxyphenyl)-2,6-bis(pyrazol-1-yl)pyridine; see Fig. 19d) to occur at exactly room temperature, $T_{1/2} = 281$ K, but without any evidence of hysteresis (Fig. 21a, b) [15]. Interestingly, X-ray diffraction studies carried out at 180 K did not reveal any intermolecular connectivity for these two compounds. The bond distances of the coordination polyhedra at this temperature confirm a low-spin state for the iron(II) in both cases, which is in accordance with magnetic measurements.

The synthesis, structural characterisation, magnetic properties and Mössbauer investigations of a linear iron(II) coordination chain of formula $[\mathrm{Fe^{II}(1\text{-}bpp\text{-}ph\text{-}1\text{-}bpp)}]_n(\mathrm{BF_4})_{2n}$ (1-bpp-ph-1-bpp = 1,4-bis{2,6-bis(pyrazol-1-yl)pyridin-4-yl}benzene) have been reported [40]. The polynuclear structure of the complex was proven via ESI mass spectral data for the complex in methanol–DMF–acetonitrile solution, providing evidence for the presence of a pentanuclear oligomeric unit $[\mathrm{Fe_5^{II}(1\text{-}bpp\text{-}ph\text{-}1\text{-}bpp)_5(BF_4^-)_8(OH^-)_6}]^{2+}$, together with fragmented smaller nuclear entities. However, the only partial solubility of the complex in the abovementioned solvent mixture advocates for the presence of higher-chain homologues that possess even more than five repeating units. Considering the linear rod-like shape of the ligand, the formation of cyclic oligomers can be excluded (Fig. 22).

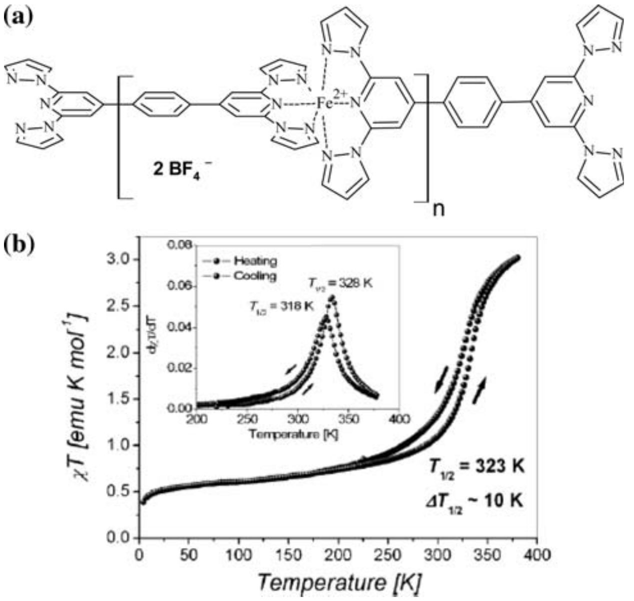

Fig. 22 **a** Representation of the molecular structure of the Fe(II) 1D coordination oligomer/polymer $[\mathrm{Fe^{II}(1\text{-}bpp\text{-}ph\text{-}1\text{-}bpp)}]_n(\mathrm{BF_4})_{2n}$, and **b** its ST properties

A variable-temperature magnetic investigation of $[Fe^{II}(1\text{-bpp-ph-}1\text{-bpp})]_n(BF_4)_{2n}$ was carried out in heating and cooling modes (Fig. 22b). A thermal hysteresis with a ca. 10 K loop width was observed, ($T_{1/2(\downarrow)} = 318$ K; $T_{1/2(\uparrow)} = 328$ K), although the χT value was almost constant below 225 K, reaching a minimum value of 0.38 emu K mol^{-1} at 4.5 K. This residual magnetic moment most likely arises from HS ions of the water end-capped iron(II) at the linear chain ends.

Another interesting family of iron(II) ST compounds with 2,6-bis(pyrazol-3-yl)pyridine (Fig. 19, 3-bpp) ligands was only recently reported by Clemente-León et al. [41]. In this work, three heterometallic complexes containing ST cations $[Fe^{II}(3\text{-bpp})]^{2+}$ and paramagnetic $[Cr^{III}(bpy)(ox)_2]^-$ or $[Cr^{III}(phen)(ox)_2]^-$ anions (bpy = 2,2′-bipyridine, phen = phenanthroline, ox = oxalate) are described. Single-crystal X-ray structural analysis of the compound exhibiting the formula $[Fe^{II}(3\text{-bpp})_2][Cr^{III}(bpy)(ox)_2]\cdot 2H_2O$ reveals two nonequivalent iron(II) sites, Fe(1A) and Fe(1B) (Fig. 23 a, b). The Fe(1A)–N distances are in the range of 2.146(2)–2.210(2) Å and are characteristic for the HS configuration. In contrast, the Fe(1B)–N distances are shorter, 1.921(2)–1.976(2) Å, and are typical of LS iron(II). Thus, the structure shows the coexistence of HS and LS iron centres in the same crystalline phase. The four noncoordinating –NH groups of centre A are hydrogen-bonded to three anions $[Cr^{III}(bpy)(ox)_2]^-$ and one water molecule, and the diamagnetic Fe(B) centres are surrounded by four $[Cr^{III}(bpy)(ox)_2]^-$ anions at hydrogen-bonding distances. Due to the fact that the terminal O atoms of oxalates are better hydrogen-bonding acceptors than water, the electron density in the corresponding pyrazolyl ring of B is increased with respect to the A centre, leading to a strengthening of the N(imine)–Fe(1B) bond, which favours the LS state for the Fe(1B) centre. Additionally, one more type of intermolecular interaction was found in the supramolecular structure of this compound. The cationic $[Fe^{II}(3\text{-bpp})]^{2+}$ units are organized into layers via π–π stacking interactions between neighbouring pyrazole parts (3.204 Å), and the anionic layers show aryl–aryl interactions between neighbouring bispyridyl ligands (in the range 3.583(2)–3.742(1) Å). Finally, the cationic and anionic layers are interconnected by an intricate hydrogen-bonding network involving water molecules. Note that dehydration and subsequent hydration are irreversible processes for this compound, and the crystal structure of the subsequent hydrated compound $[Fe(3\text{-bpp})_2][Cr^{III}(bpy)(ox)_2]\cdot 2H_2O$ exhibits only a HS type of $[Fe(3\text{-bpp})]^{2+}$ cation connected by hydrogen bonds to three $[Cr^{III}(bpy)(ox)_2]^-$ anions and one molecule of water.

The magnetic properties of $[Fe^{II}(3\text{-bpp})_2][Cr^{III}(bpy)(ox)_2]\cdot 2H_2O$ are shown in Fig. 23c. The spin states of the iron(II) centres show a strong dependence on the presence of water molecules in the structure. The dihydrate compound shows a constant value of the χT product (5.5 emu K mol^{-1}) up to 320 K, which corresponds to the situation where the Fe(A) centres are HS and the Fe(B) centres are in the LS state. Above 320 K, the χT versus T curve decreases due to the removal of water molecules and then reaches a plateau value of 7 emu K mol^{-1} at 400 K, which corresponds to a 100% HS state for all iron(II) atoms. In the anhydrous sample, all iron(II) centres undergo reversible and reproducible ST with a 16 K thermal hysteresis loop centred above room temperature ($T_{1/2(\downarrow)} = 353$ K and $T_{1/2(\uparrow)} = 369$ K). In the second cycle, the hydrated material shows completely different magnetic behaviour: below room temperature, the χT product is constant (7.5 emu K mol^{-1}) and its value is in good agreement with the spin-only value for a trinuclear system $2Cr^{III} + Fe^{II}(HS)$ ($2 \times S_1 = 3/2 + S_2 = 4/2$, $\chi T^{\text{spin-only}} = 6.76$ emu K mol^{-1}). Above 300 K, water is removed and the ST of the dehydrated compound is identical to that before hydration. The authors also present two other

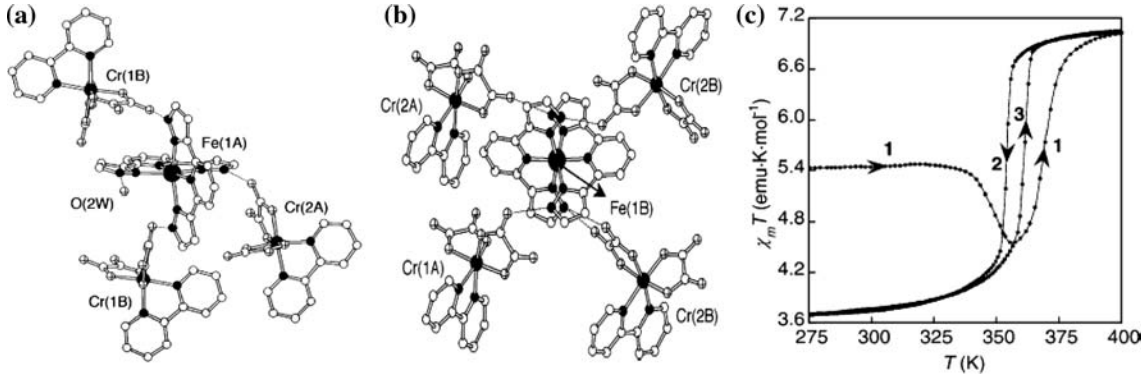

Fig. 23 Representation of the X-ray structural analysis of $[Fe^{II}(3\text{-bpp})_2][Cr^{III}(bpy)(ox)_2]\cdot 2H_2O$, showing **a** the two nonequivalent Fe(II) centres: the HS Fe^{II}(A) centre is linked by hydrogen bonds to three anions of $[Cr^{III}(bpy)(ox)_2]^-$ and to one molecule of water. **b** The LS Fe^{II}(B) is connected by hydrogen bonds to four Cr^{III} counteranions; **c** $\chi_M T$ versus T plot of $[Fe^{II}(3\text{-bpp})_2][Cr^{III}(bpy)(ox)_2]\cdot 2H_2O$; heating of the hydrated compound (first step), cooling (second step) and heating (third step)

compounds of general formula $[Fe^{II}(3\text{-bpp})_2][Cr^{III}(phen)(ox)_2]\cdot nH_2O\cdot mCH_3OH$, where $n = m = 1/2$, which are isostructural with the previous complex. Again, the single-crystal structure reveals two different iron(II) centres: Fe(A), which is HS and surrounded with three $[Cr^{III}(phen)(ox)_2]^-$ complexes and one molecule of water; and Fe(B) centres, which are LS and hydrogen bonded with four Cr^{III} complexes. There is also a similarity in terms of crystal packing: the π–π interactions are in-between pyrazolyl rings (cation part) and in-between phenanthroline rings (anion part). Equally, only the solvent-free compounds exhibit a complete spin transition, which is situated above room temperature and accompanied by thermal hysteresis ($T_{1/2(\downarrow)} = 353$ K and $T_{1/2(\uparrow)} = 369$ K, $\Delta T_{1/2} = 4$ K).

Miscellaneous room-temperature iron(II) ST systems

Recently, the Jäger-type mononuclear iron(II) complex $[Fe^{II}(Ph(Imoxo)_2)(HIm)_2]^0$ ($Ph(Imoxo)_2$ = diethyl(E,E)-2,2′-[1,2-phenylenebis-(iminomethylidyne)]-bis[3-butanoate], HIm = imidazole) was shown to exhibit an abrupt ST centred at approximately 297 K ($T_{1/2(\downarrow)} = 244$ K and $T_{1/2(\uparrow)} = 314$ K) and an unusually large thermal hysteresis loop with $\Delta T_{1/2} = 70$ K (Fig. 24b) [42]. The HS value of the χT product was determined as 3.32 emu K mol^{-1} (at 325 K), which is in accordance with the pure Fe^{II} HS state. The HS plateau remains approximately constant down to 250 K, where an abrupt transition to the LS state is observed and the LS value of χT is 0.15 K (at 200 K). Upon heating, the LS state of $[Fe^{II}(Ph(Imoxo)_2)(HIm)_2]^0$ stays constant up to 300 K (0.31 emu K mol^{-1}), when it increases abruptly to the HS value. These ST properties are resistant to grinding effects and are fully reproducible.

The single-crystal X-ray structure of $[Fe^{II}(Ph(Imoxo)_2)(HIm)_2]^0$ was obtained at 275 K and the bond distances of the coordination polyhedron (Fe^{II}–N(L) = 2.08 Å; Fe^{II}–N(HIm) = 2.22 Å; Fe^{II}–O = 2.03 Å) are in accord with those reported for similar HS iron(II) complexes (Fig. 24a). Due to the unusually large hysteresis, a detailed investigation of the intermolecular interactions is important to understanding of the ST properties of this complex. A closer look at the supramolecular contacts between the mononuclear units reveals two different types of hydrogen-bond bridging: the first one involves the N*H* hydrogen atom of the imidazole unit and the OCOEt oxygen atom (O5) of the ligand $Ph(Imoxo)_2$ (N···O = 2.841 Å), while the second contact connects the N*H* hydrogen atom of the second imidazole with the coordinated carbonyl oxygen atom (O1) of the ligand ($Ph(Imoxo)_2$) (N···O = 2.83 Å) (Fig. 25a). The combination of the two hydrogen-bond types leads to an infinite two-dimensional layer of linked mononuclear molecules. In addition, two other short contacts between the OCOEt oxygens and the aromatic C–H groups of the imidazole and phenylene rings seem to play a

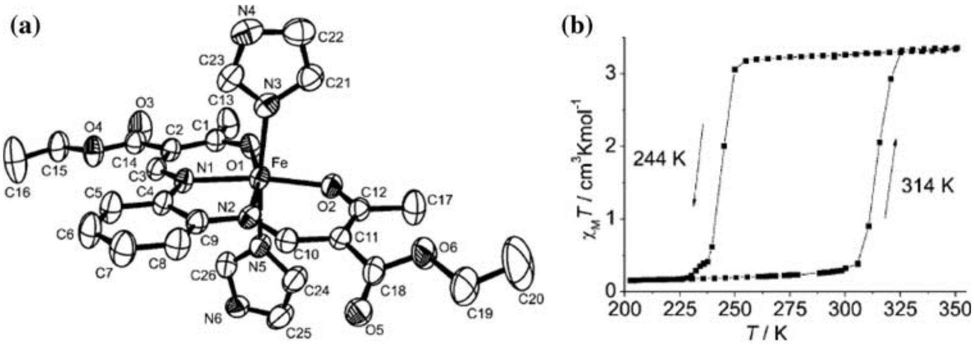

Fig. 24 **a** The single-crystal X-ray structure of the complex $[Fe^{II}((Ph(Imoxo)_2))(HIm)_2]^0$, and **b** its ST behaviour, with a thermal hysteresis $\Delta T = 70$ K

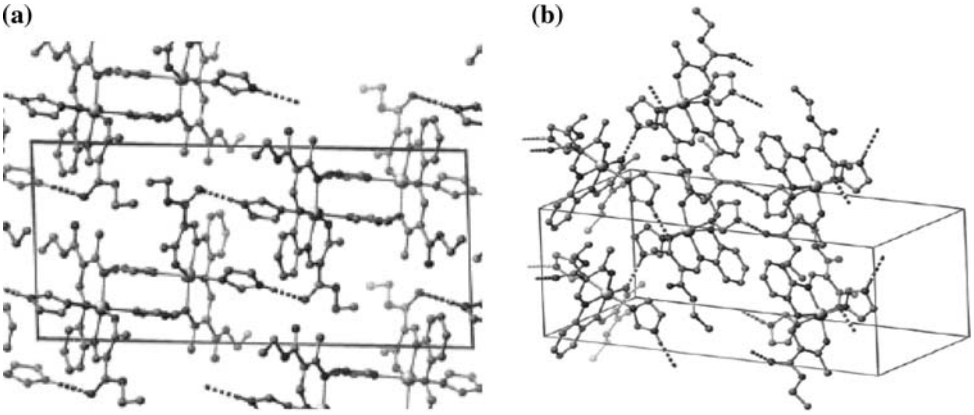

Fig. 25 Representation of the 2D layer of molecules of $[Fe^{II}((Ph(Imoxo)_2))(HIm)_2]^0$ created from **a** two different types of hydrogen bonds and **b** short-contact interactions between ester oxygens and aromatic carbons of imidazole and phenylene

role (Fig. 25b). This hydrogen-bond/short-contact network is clearly responsible for the highly cooperative character of the ST observed in this compound. It is interesting to note that a very similar mononuclear iron(II) complex involving the same ligands but a slightly different stoichiometry, $[Fe^{II}((Ph(Imoxo)_2))(HIm)_{1.8}]^0$, exhibits an ST above room temperature with a 4 K hysteresis, $T_{1/2(\downarrow)} = 328$ K and $T_{1/2(\uparrow)} = 332$ K [43]. The slight difference in stoichiometry seems to significantly disturb the subtly balanced H-bond network, leading to reduced cooperative interactions.

Another family of mononuclear ST complexes, of general formula $[Fe^{II}(L)_2](X)_2 \cdot n$S, has been reported by Boča et al. [44–46, 104], where L are tridentate N-donor benzimidazole-type ligands (Fig. 26).

The magnetic properties of $[Fe^{II}(bzimpy)_2](BPh_4)_2 \cdot nH_2O$ show a strong dependence on the presence of water in the lattice ($n = 4, 2, 0$) [104]. The complex with $n = 4$ exhibits a spin transition in the temperature range 280–350 K. The μ_{eff} values in the LS (ca 1.6 μ_B) and HS (ca 5.5 μ_B) states are typical of the $S = 0 \leftrightarrow 2$ spin crossover. Up to 323 K, the spin transition occurs without thermal hysteresis and is reproducible (Fig. 27). Above 400 K, the complex loses water and stays high spin. In the complex $[Fe^{II}(bzimpy)_2](SO_4)_2 \cdot 2H_2O$, the spin transition is visible between 300–480 K, but at the highest edge of the data collection it is not complete.

The perchlorate analogue $[Fe^{II}(bzimpy)_2](ClO_4)_2 \cdot 0.25H_2O$ shows an abrupt spin transition centred above RT, $T_{1/2(\uparrow)} = 409$ K and $T_{1/2(\downarrow)} = 397$ K (Fig. 28b); the hysteresis width is $\Delta T_{1/2} = 12$ K [45]. In this compound, a 3D network of π–π stacking exists among the benzene rings, which probably causes and/or enhances the solid-state cooperativeness. At the transition temperature, the complex shows a reversible, first-order phase transition (as verified by DSC calorimetry), and it exhibits a structural phase transition (as seen from powder diffraction patterns)

The compound $[Fe^{II}(tzimpy)_2](ClO_4)_2 \cdot 2H_2O$ shows strong temperature dependence of the effective magnetic moment, leading to the conclusion that the ST occurs above room temperature (Fig. 29) [46]. Values of μ_{eff} are 1.0 μ_B below 250 K (LS) and 5.1 μ_B at 385 K (HS), which means that a ST occurs between the spin states $S = 0$ and 2. This ST is associated with a thermal hysteresis centred at $T_{1/2} = 323$ K ($T_{1/2(\downarrow)} = 306$ K, $T_{1/2(\uparrow)} = 340$ K), and the hysteresis width is $\Delta T_{1/2} = 35$ K.

The neutral, mononuclear iron(II) complex of formula $[Fe^{II}(bzimpy_{-1H})_2]^0 \cdot H_2O$ with the deprotonated ligand bzimpy$_{-1H}$ shows a more complex magnetic behaviour (Fig. 30). The effective magnetic moment rises from its room-temperature value of 1.3 to 4.2 μ_B at 500 K. At about this temperature, the compound undergoes irreversible changes: liberation of the crystal water, a colour change (blue–green), followed by a structural change (as

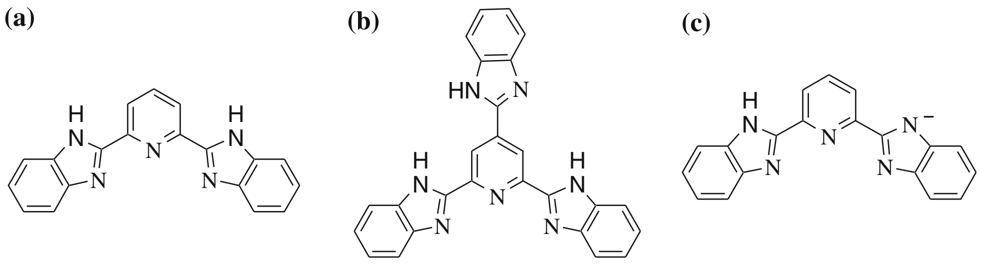

Fig. 26 Schematic representation of benzimidazole-type ligands: **a** bzimpy, 2,6-bis(benzimidazol-2-yl)pyridine; **b** tzimpy, 2,4,6-tris(benzimidazol-2-yl)pyridine; **c** bzimpy$_{-1H}$, mono-deprotonated bzimpy

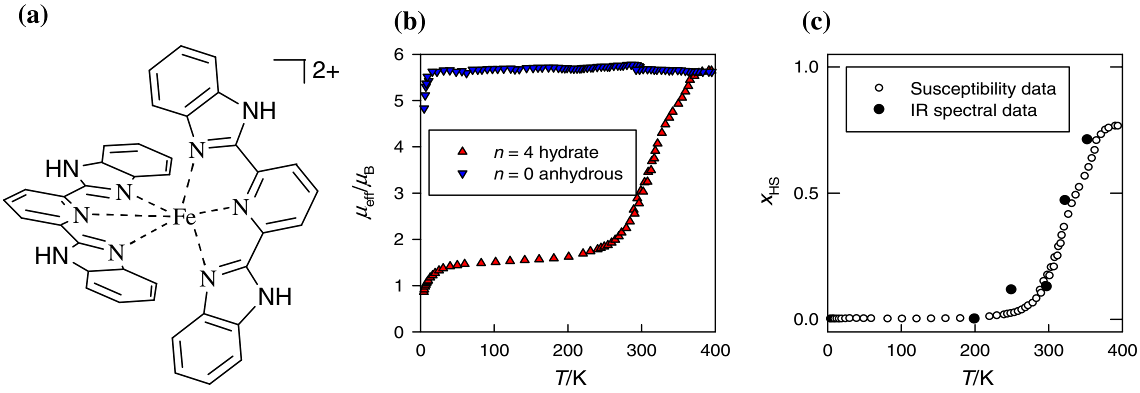

Fig. 27 $[Fe(bzimpy)_2](BPh_4)_2 \cdot nH_2O$ complexes: **a** molecular structure of $[Fe(bzimpy)_2]^{2+}$; **b** magnetic properties; **c** high-spin mole fraction for $n = 4$

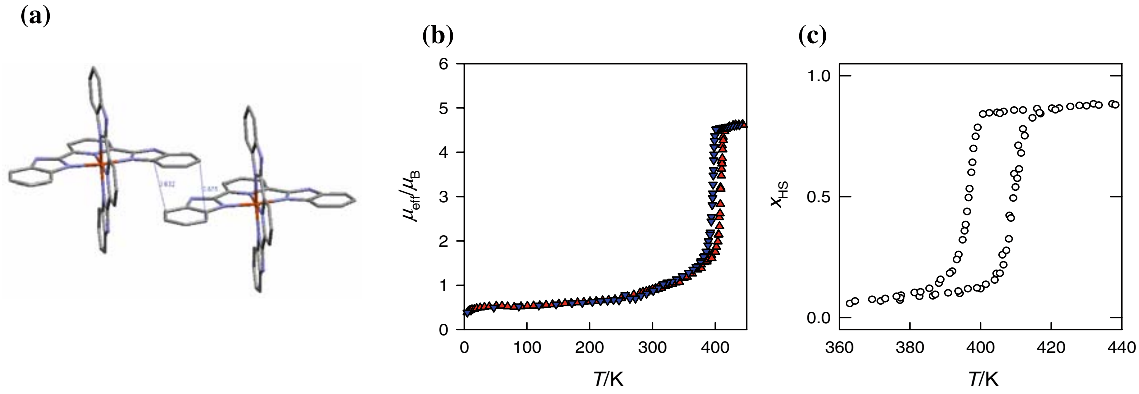

Fig. 28 $[Fe^{II}(bzimpy)_2](ClO_4)_2{\cdot}0.25H_2O$ complex: **a** packing of $[Fe^{II}(bzimpy)_2]^{2+}$ units with π–π stacking; **b** magnetic properties; **c** high-spin mole fraction

Fig. 29 $[Fe^{II}(tzimpy)_2](ClO_4)_2{\cdot}2H_2O$ complex: **a** structure of $[Fe^{II}(bzimpy)_2]^{2+}$ unit; **b** magnetic properties

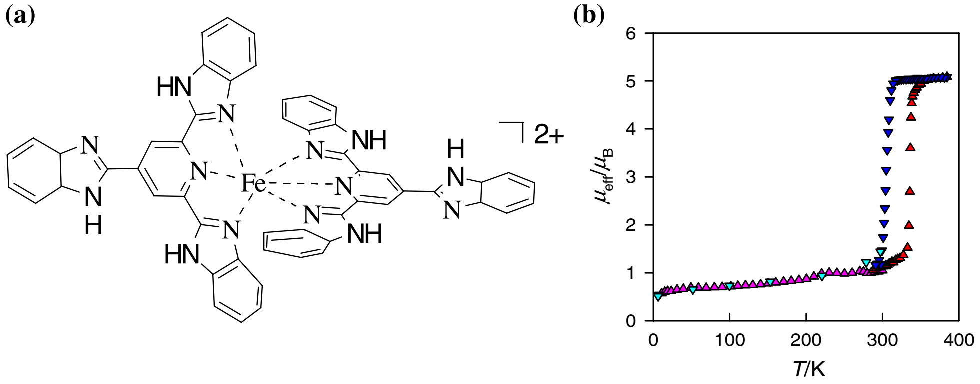

Fig. 30 Molecular compound $[Fe^{II}(bzimpy_{-1H})_2]^0$: **a** structure of the $[Fe^{II}(bzimpy_{-1H})_2]^0$ unit; **b** magnetic properties

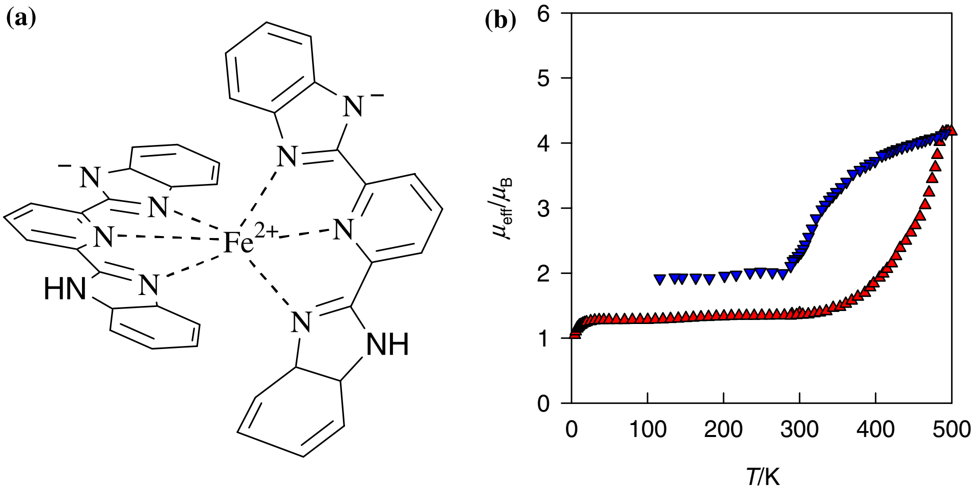

determined by TGA analysis, IR spectroscopy and X-ray powder diffraction). After that, in the cooling mode, the μ_{eff} gradually decreases, and below 300 K it adopts a value of 2.0 μ_B; this value is caused by partial oxidation above 500 K (the presence of iron(III) in the sample was confirmed by Mössbauer spectroscopy).

In 1976 Sams and Tsin reported a family of mononuclear iron(II) complexes of the bidentate N-donor ligand 2-(2′-pyridyl)benzimidazole (pyben) [47]. In this work, six complexes of general formula $[Fe^{II}(pyben)_3](X)_2{\cdot}nH_2O$ were described, and room-temperature STs were observed for $X = BPh_4^-$, $n = 1$; $X = Cr(NH_3)(NCS)_4^-$, $n = 0$ and $X = BF_4$, $n = 2$. However, due to experimental limitations, magnetic measurements of these compounds were only carried out up to room temperature, meaning that their STs were incomplete.

The ST properties of the compound $[Fe^{II}(phy)_2](BF_4)_2$ (phy = 1,10-phenanthroline-2-carbaldehyde phenylhydrazone, Fig. 31a) are reported in several papers by König et al. [48–50]. Magnetic measurements (Fig. 31b) of this complex reveal an ST, $T_{1/2(\downarrow)} = 279$ K and $T_{1/2(\uparrow)} = 286$ K, that exhibits a hysteresis loop of $\Delta T_{1/2} = 7$ K. This thermal hysteresis was consistently confirmed by other techniques: Mössbauer spectroscopy ($T_{1/2(\downarrow)} = 277$ K and $T_{1/2(\uparrow)} = 286$ K), variable-temperature X-ray powder diffraction ($T_{1/2(\downarrow)} = 277$ K and $T_{1/2(\uparrow)} = 284$ K), and DSC studies ($T_{1/2(\downarrow)} = 276$ K and $T_{1/2(\uparrow)} = 288$ K). The same group also presented a very detailed analysis of the hysteresis of this complex [49] and the effect of pressure on the thermal hysteresis [50].

Among the group of mononuclear iron(II) room-temperature ST compounds, we should mention the complexes of formula $[Fe^{II}(TRIM)_2](X)_2{\cdot}MeOH$ ($X = Br^-$, HCO_2^-; TRIM = 4-(4-imidazole-methyl)-2-(2-imidazolylmethyl) imidazole) [51]. Both of these compounds exhibit very similar magnetic properties—the magnetic moment starts to increase around 250 K from the low spin value, and at 380 K it reaches 5.1 μ_B ($X = Br^-$) and 5.0 μ_B ($X = HCO_2^-$), respectively (the ST is not finished at this temperature). The transition temperatures were determined as $T_{1/2} = 340$ K for the bromo and $T_{1/2} = 330$ K for the HCO_2 analogues. The absence of thermal hysteresis seems to be a characteristic of this family of compounds.

The crystal structure of the dinuclear complex $[(TPyA)Fe^{II}(DBQ^{2-})Fe^{II}(TPyA)](BF_4)_2$ (TPyA = tris(2-pyridylmethyl)amine; H_2DBQ = 2,5-di-t-butyl-3,6-dihydroxy-1,4-benzoquinone) elucidates strong π–π interactions between the iron(II) dimers that give rise to a two-dimensional sheet structure [52]. The pyridyl groups of the TPyA ligands and the benzene ring from the DBQ^{2-} are involved in C–H–π and offset face-to-face π–π interactions between the iron(II) dimers. The X-ray crystal structure of this compound (Fig. 32a) was collected at 208 K and indicated that both iron(II) ions were LS. At 298 K, the bond distances indicate a mixed spin state in the crystal, higher than observed for the LS state but smaller than

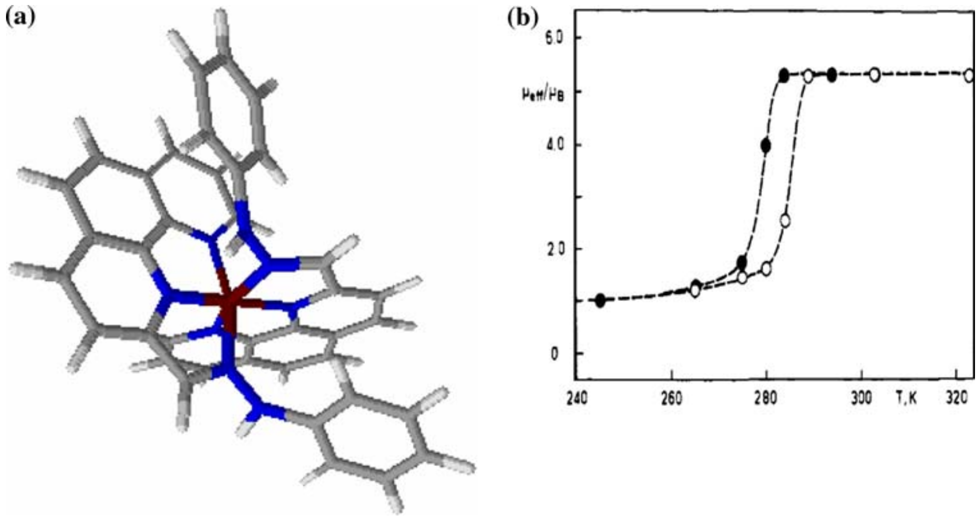

Fig. 31 Representation of **a** the molecular structure of the $[Fe^{II}(phy)_2]^{2+}$ cation (colour code for web version: *gray*, carbon; *blue*, nitrogen; *red*, iron), and **b** the magnetic properties of $[Fe^{II}(phy)_2](BF_4)_2$

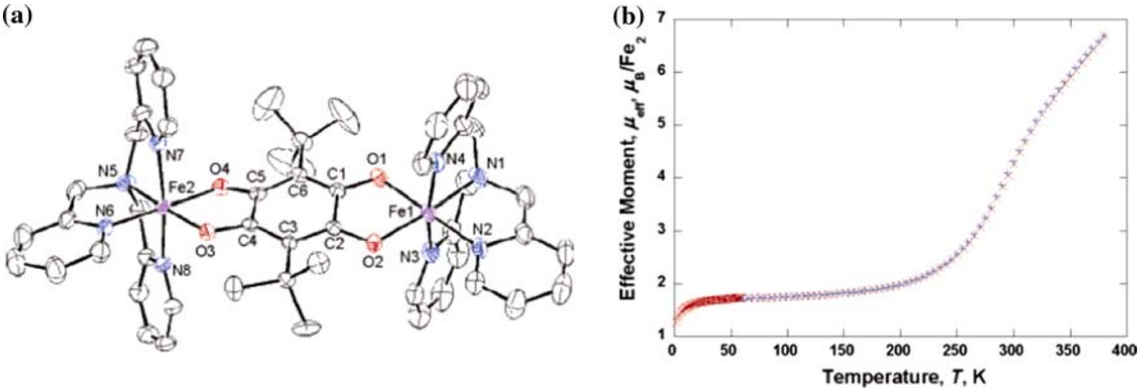

Fig. 32 **a** The ORTEP view of the complex cation $[(TPyA)Fe^{II}(DBQ^{2-})Fe^{II}(TPyA)]^{2+}$, and **b** the magnetic properties of the bulk $[(TPyA)Fe^{II}(DBQ^{2-})Fe^{II}(TPyA)](BF_4)_2$ compound

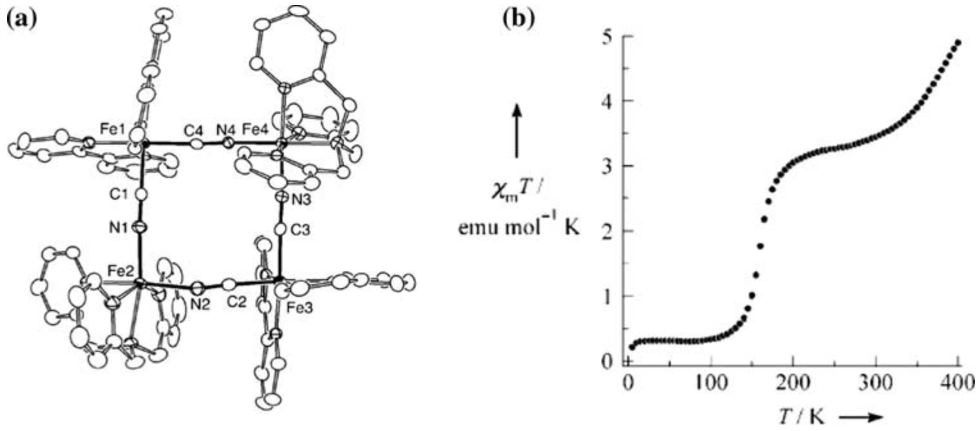

Fig. 33 **a** Representation of the molecular structure of the cation $[Fe^{II}_4(\mu\text{-CN})_4(bpy)_4(TPyA)_2]^{4+}$, and **b** the magnetic properties of the compound $[Fe^{II}_4(\mu\text{-CN})_4(bpy)_4(TPyA)_2](PF_6)_4$

observed for typical HS ions. These results are in good agreement with results from variable-temperature magnetic measurements (Fig. 32b). The magnetic moment starts to increase from an LS value of around 200 K, reaching 6.69 μ_B at 380 K, which is very close to the spin-only value for the system $2 \times S = 2$(ca. 6.93 μ_B).

Another interesting oligomer—the tetranuclear iron(II) complex $[Fe^{II}_4(\mu\text{-CN})_4(bpy)_4(TPyA)_2](PF_6)_4$ (bpy = 4,4′-bipyridine, TPyA = tris(2-pyridylmethyl)amine)—contains two types of irons, Fe1 and Fe3 (Fig. 33a), which are coordinated via the carbon from the cyano group, leading to LS at these centres over the whole investigated temperature range [53]. The bond distances of these iron(II) ions within the coordination polyhedra are typical of low-spin iron at 100 K. At 200 and 300 K, the Fe1, Fe3 and Fe4 centres are still in the LS state, but the Fe2 centre starts to form a longer Fe(II)–N bond (2.154–2.165 Å) characteristic of the HS iron(II) state. The magnetic properties of this complex are shown in Fig. 33b and are in good agreement with the X-ray results in the temperature range 5–100 K. As the temperature is raised to 200 K the χT product increases, reaching a plateau value at 3.2 emu K mol^{-1}, which is close to the spin-only value for a single spin system of $S = 2$. However, a second spin conversion starts around room temperature, and at 400 K the χT value reaches 4.9 emu K mol^{-1} without saturation. Variable-temperature Mössbauer spectroscopy of this compound did indeed confirm two-step spin transition behaviour at higher temperatures.

Iron(III) and mixed-valence room-temperature ST compounds

In general, the iron(III) ST does not deliver such an abrupt transition as that observed for iron(II) compounds, and of course the diamagnetic plateau of the low-spin state is replaced by a paramagnetic one. On the other hand, the thermochromism of iron(III) ST compounds shows more variety and more intensive colours than in the iron(II) case. Moreover, the d^5 spin system offers not only spin-state switching between the respective LS ($S = ½$) ↔ HS ($S = 5/2$) states, but also frequently involves an intermediate spin state, IS ($S = 3/2$) [54–59], which leads to ideas beyond bistability.

Thus, several reports deal with iron(III) room-temperature ST compounds containing thiosemicarbazone ligands (Fig. 34) [60–66]. Among the reported examples, the compound of formula $Li[Fe^{III}(5Br\text{-}thsa)_2]\cdot H_2O$ (H_2(5Br-thsa) = 5-bromosalicylaldehyde thiosemicarbazone, see Fig. 34a) was studied using several techniques, like SQUID measurement, DSC, temperature-dependent IR, X-ray powder and Mössbauer spectroscopy. The ligand is coordinated to iron(III) ion via its oxygen, Schiff-base nitrogen and sulfur donor atoms (Fig. 35a).

The SQUID measurements of $Li[Fe^{III}(5Br\text{-}thsa)_2]\cdot H_2O$ reveal a ST with a hysteresis loop in the range of $T_{1/2(\downarrow)} = 294$ K and $T_{1/2(\uparrow)} = 333$ K, with $\Delta T_{1/2} = 39$ K (Fig. 35b). The magnetic susceptibility measurements up to 380 K prove that the spin-state change at the iron(III) metal ion occurs between the LS ($S = ½$) and the HS ($S = 5/2$). The ST curve gradient is rather gradual in the cooling mode, but becomes rather abrupt in the heating mode. This abnormal asymmetry between branches is attributed to the

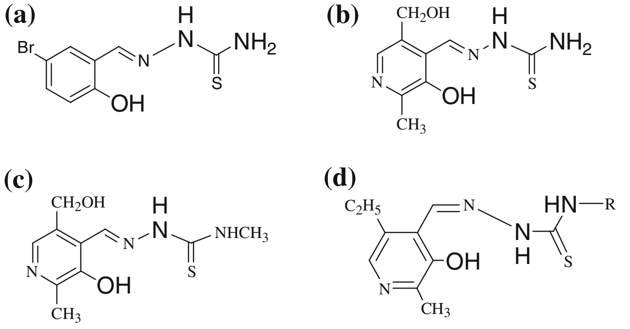

Fig. 34 The molecular structures of thiosemicarbazone-type ligands: **a** H_2(5Br-thsa); **b** H(thpy); **c** H(mthpy); and **d** H(R-thsa), R = Ph, Me, Et

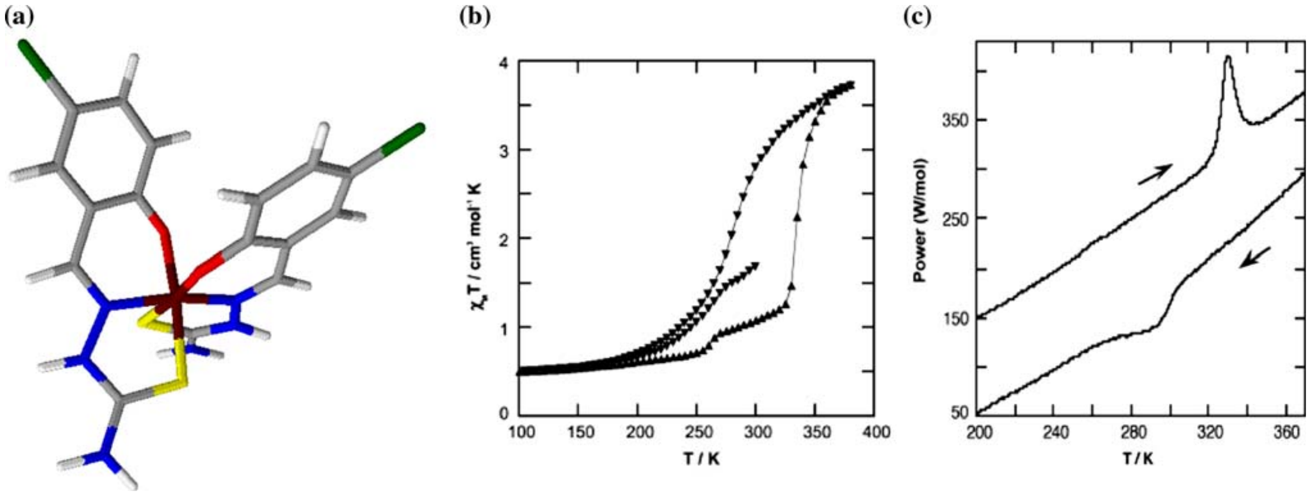

Fig. 35 **a** The proposed molecular structure of the complex anion $[Fe^{III}(5B\text{-rthsa})_2]^-$ (colour code for web version: *brown*, iron; *blue*, nitrogen; *red*, oxygen; *green*, bromine; *yellow*, sulfur; *grey*, carbon; *white*, hydrogen), **b** SQUID data, and **c** DCS diagram for $Li[Fe^{III}(5Br\text{-rthsa})_2]\cdot H_2O$

presence of solvent molecules in the crystal structure, which may provide additional defects or positional disorder and eventually provokes the loss of a small amount by desolvation. A further explanation for the asymmetric shape of the thermal hysteresis is the presence of two or more crystallographic phases, as also confirmed by X-ray powder investigations.

Variable-temperature Mössbauer spectroscopy of this compound confirmed an ST at $T_{1/2(\downarrow)} \approx 274$ K and $T_{1/2(\uparrow)} \approx 332$ K, while the DSC investigations yielded that the ST temperatures were slightly shifted from those in the magnetic measurements, $T_{1/2(\downarrow)} \approx 291$ K and $T_{1/2(\uparrow)} \approx 330$ K (Fig. 35c). The presence of thermal hysteresis was further corroborated by variable temperature X-ray powder studies, which yielded $T_{1/2(\downarrow)} \approx 279$ K and $T_{1/2(\downarrow)} \approx 338$ K.

Several other reports have demonstrated STs for a series of thiosemicarbazone iron(III) compounds where the ligands are only slightly different from H_2(5Br-thsa) or were just obtained by counteranion exchange. Note that the compound $NH_4[Fe(5\text{-Br-thsa})_2]$ [61], which crystallised into two different polymorphs, shows an ST in the region of around 200 K for a 2D "mica"-like crystal lattice, while the second polymorph (tabular plates) exhibits a gradual ST up to 400 K. The ST in the solvent-free compound $NH_4[Fe^{III}(3,5\text{-Cl-thsa})_2]\cdot 1,5H_2O$ (3,5-Cl-thsa = 3,5 dichlorosalicylaldehyde-thiosemicarbazone) starts at 80 K and continues to above room temperature, while $Cs[Fe^{III}(3,5\text{-Cl-thsa})_2]$ remains HS and $NH_4[Fe^{III}(thsa)_2]$ (thsa = salicylaldehydethiosemicarbazone) stays LS across the temperature range [62–64]. Another class of iron(III) room-temperature ST compounds that also belong to the category of complexes with thiosemicarbazone ligands was reported by Tido et al. [65]. Two mononuclear complexes of formula $[Fe^{III}(Hthpy)(thpy)]\cdot CH_3OH\cdot 3H_2O$ and $[Fe^{III}(Hmthpy)(mthpy)]\cdot 2H_2O$ (Hthpy = pyridoxal thiosemicarbazone (Fig. 30b), Hmthpy = pyridoxal methylthiosemicarbazone, see Fig. 34c; thpy⁻ and mthpy⁻ are the mono-deprotonated forms of these ligands) were investigated by X-ray, SQUID and DSC studies. In both compounds, the χT product starts to increase above 200 K from values typical of LS iron(III). Above room temperature, the spin transition is more abrupt and is not saturated at 375 K (Fig. 36a, b). The reports do not provide any evidence for thermal hysteresis.

In 1991, Gupta et al. [66] reported on three mononuclear iron(III) complexes with modified analogues of thiosemicarbazone ligands of general formula $[Fe(R\text{-thsa})_2]Cl_2$ (R-thsa = pyridoxal 4-R-thiosemicarbazone R = Ph, Me, Et). The magnetic properties of these compounds were obtained on a vibrating-sample magnetometer at 0.5 T. In the cases of R = Me and Et, the authors observed blocked LS behaviour, whereas for H(Ph-thsa) they observed abrupt ST behaviour at the temperatures of $T_{1/2(\uparrow)} = 299$ K and $T_{1/2(\downarrow)} = 290$ K. According to the values of μ_B, the ST occurs between the LS (S = ½) and HS (S = 5/2) states.

Another family of ST iron(III) compounds features the general formula $[Fe^{III}(qsal)_2]X\cdot solv$ (Hqsal = *N*-(8-quinolyl)salicylaldimine) [67–71]. The respective iron(III) ST compounds were reported by Sato and his research group for $[Fe^{III}(qsal)_2]NCSe\cdot solv$ (Fig. 37), where qsal is the tridentated Schiff base ligand coordinated with iron(III) via two nitrogens and one oxygen, and "solv" stands either for CH_3OH or CH_2Cl_2 [67]. It was shown that the magnetic properties of the cation $Fe^{III}(qsal)_2^+$ are strongly dependent on the nature of the counteranions and/or the solvent molecules [68, 69]. Temperature-dependent magnetic measurements were carried out in several heating and

Fig. 36 The X-ray structures and magnetic measurements of **a** $[Fe^{III}(Hthpy)(thpy)]\cdot CH_3OH\cdot 3H_2O$ and **b** $[Fe^{III}(Hmthpy)(mthpy)]\cdot 2H_2O$

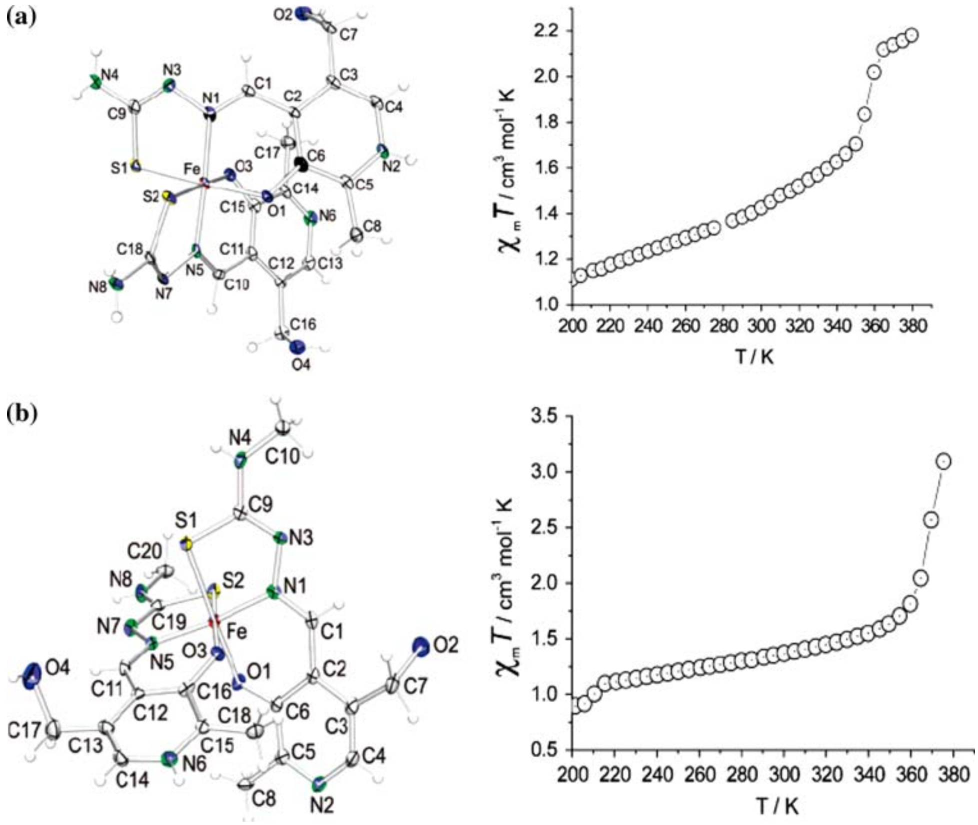

cooling cycles. For both solvation isomers, the first cycle in heating mode revealed a ST defined by $T_{1/2(\uparrow)} = 352$ K for solv = CH_3OH and 392 K for solv = CH_2Cl_2. In the subsequent cooling mode, both compounds showed an abrupt drop in magnetic moment at $T_{1/2(\downarrow)} = 212$ K. In the second thermal cycle, after desolvation, the magnetic properties of these two compounds were identical. In cooling mode, $T_{1/2(\downarrow)}$ remains at 212 K, and in the second heating mode ST is shifted to $T_{1/2(\uparrow)} = 282$ K, revealing a two-step ST with 70 K hysteresis in both cases (Fig. 37).

These very unusual magnetic properties—(1) ST with large thermal hysteresis widths of around 70 K, and (2) a two-step ST only in the heating mode—are attributed to the intermolecular arrangement of the ST molecules in the crystal structure. The $Fe^{III}(qsal)_2^+$ cations exhibit π–π stacking of the qsal ligands between the quinoline and phenyl rings, forming a one-dimensional network of solvated complexes in both cases. The nearest-neighbour distances between the quinoline and the phenyl rings are in range 3.35–3.52 Å, explaining the strong cooperativeness between the packed molecules. Furthermore, molecular stacking was noted between the phenyl rings in the qsal moieties, through which the one-dimensional molecular assemblies are converted into a 2D sheet structure. The distances between neighbouring molecules within the 2D sheets are around 13.75 Å (solv = CH_3OH) and 14.04 Å (solv = CH_2Cl_2), respectively. The counteranions and the solvent molecules are localized between the 2D sheets and do not participate in the polymeric superstructure. This result explains why these compounds do not lose their cooperative nature even after solvent removal.

It is worth noting that a iron(III)–qsal complex of formula $[Fe^{III}(qsal)_2]NCS$ exhibits a strong dependence of its magnetic properties on its preparation parameters, in particular its coordination temperature [71]. The complex prepared at 298 K exhibits ST in the range between 220 and 270 K, while the complex prepared below 280 K remains LS across the temperature range.

Another family of iron(III) ST compounds are complexes of formula $[Fe^{III}(pap)_2]X\cdot solv$ (Hpap = *N*-bis (2-hydroxyphenyl)-(2-pyridyl)-methaneimine]) [72–74]. Here, the solvent-free compounds with X = NO_3^- and BPh_4^- persist in their HS states, while the PF_6^- analogue is blocked in the LS state. However, freshly prepared, unsolvated $[Fe^{III}(pap)_2]ClO_4$ exhibits a ST with a hysteresis at $T_{1/2(\uparrow)} = 262$ K and $T_{1/2(\downarrow)} = 242$ K [72], but after aging in air in the presence of moisture, the ST temperatures were shifted to $T_{1/2(\uparrow)} = 180$ K and $T_{1/2(\downarrow)} = 165$ K, respectively [73]. The compound $[Fe^{III}(pap)_2]PF_6\cdot CH_3OH$ (Fig. 38a) shows a quite abrupt ST centred around $T_{1/2} = 288$ K (Fig. 38b). Moreover, this compound shows light-induced spin-state switching (the LIESST effect) at low temperatures [74].

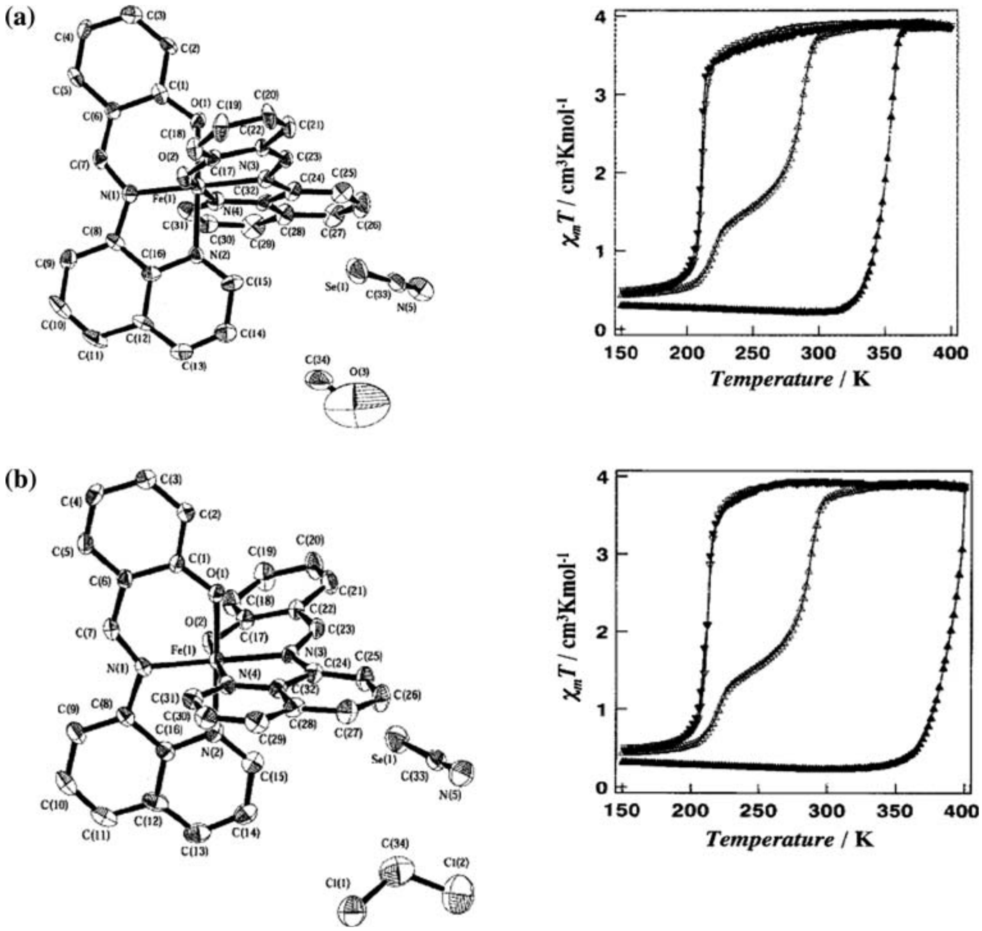

Fig. 37 Molecular structures (*left*) and magnetic properties (*right*) of **a** $[Fe^{III}(qsal)_2]NCSe\ CH_3OH$ and **b** $[Fe^{III}(qsal)_2]NCSe\ CH_2Cl_2$

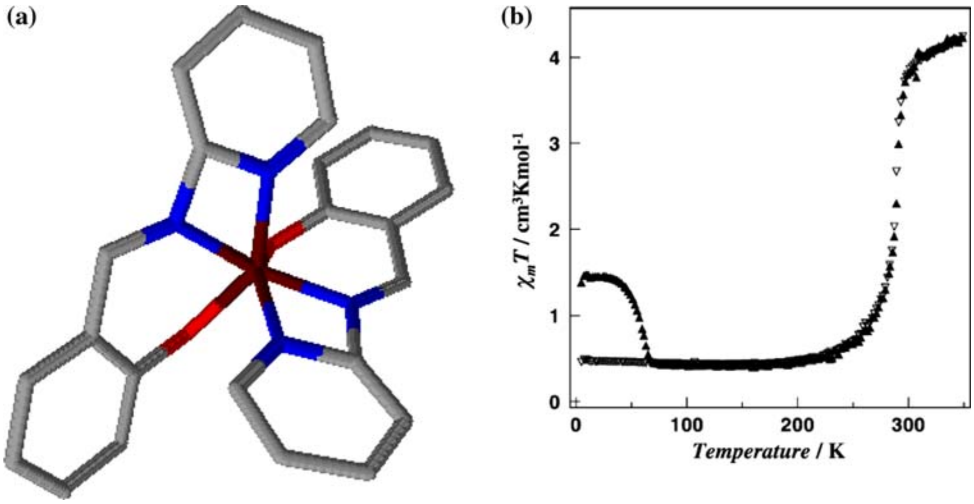

Fig. 38 **a** The proposed molecular structure of the complex $[Fe^{III}(pap)_2]^+$ (colour code for web version: *brown*, iron; *blue*, nitrogen; *red*, oxygen; *grey*, carbon; *white*, hydrogen), and **b** the magnetic properties of the compound $[Fe^{III}(pap)_2]PF_6{\cdot}CH_3OH$, showing LIESST at low temperatures

The supramolecular pseudo-dinuclear iron(III) complex of formula $\{[Fe^{II}H_2L]\cdots[Fe^{III}HL]\}(ClO_4)_2{\cdot}H_2O$, ($H_3L$ being the Schiff base condensate of 5-methylpyrazole-3-carbaldehyde and tris(2-aminoethyl)amine) belongs to the category of mixed-valence iron (II/III) complexes exhibiting room-temperature ST (Fig. 39a) [75]. The crystal structures of this compound, determined at 93 and 295 K, reveal a pseudodimer of two almost structurally identical iron complexes at different redox states (Fig. 39b). The variable-temperature magnetic measurements depicted in Fig. 39c show that the magnetic moment per pseudodimer in the temperature region 4–200 K is around 2.3 μ_B, a value which is consistent with both iron metal ions being in the LS state in each half-molecule, and this is confirmed by

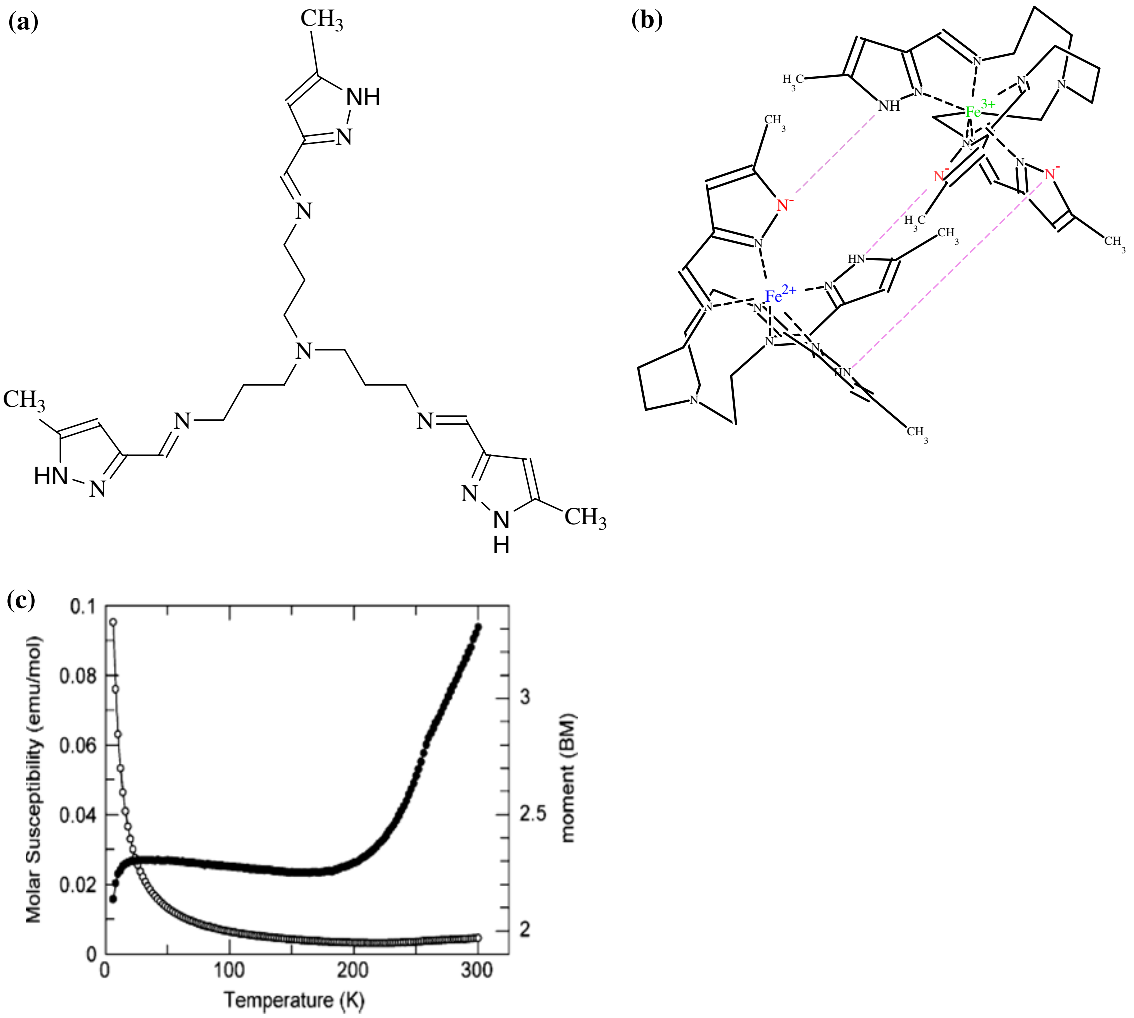

Fig. 39 **a** Molecular structure of the ligand H_3L, the Schiff base condensate of 5-methylpyrazole-3-carbaldehyde and tris(2-aminoethyl)amine; **b** 3D view of the pseudodimer complex cation $\{[Fe^{II}H_2L]\cdots[Fe^{III}HL]\}^+$ (colour code for web version: *red nitrogens* are negatively charged, *blue iron* is Fe^{II}, *green iron* is Fe^{III}, *pink dashed lines* represent hydrogen bonds); **c** magnetic properties of the pseudodimer compound $\{[Fe^{II}H_2L]\cdots[Fe^{III}HL]\}(ClO_4)_2{\cdot}H_2O$

Mössbauer spectroscopy. However, above 200 K the magnetic susceptibility starts to increase and reaches a value of 3.3 μ_B at 300 K, which can be interpreted as a situation where all iron(III) centres are in the LS state and 33% of iron(II) centres are HS. However, the Mössbauer spectra analysis at 298 K reveals that only 21% of the Fe^{II} are HS. These inconsistencies between the Mössbauer and SQUID data are attributed to Debye–Waller factors or non-Lorentzian line shapes in the Mössbauer spectra. Both investigation techniques clearly indicate that at 300 K a significant proportion of Fe^{II}(HS) emerges, and the shape of the μ_B versus T curve indicates the continuation of the ST above room temperature.

A series of polynuclear Prussian blue analoques of general formula $[M^{II}(tmphen)_2]_3[M'^{III}(CN)_6]{\cdot}xCH_3CN$ (tmphen = 3,4,7,8 tetramethyl-1,10-phenanthroline; M/M′ = Fe^{II}/Fe^{III}, Fe^{II}/Co^{III}, Fe^{II}/Cr^{III}) were described by Shatruk et al. [76]. In the case of M/M′ = Fe^{II}/Fe^{III} and Fe^{II}/Co^{III}, the compounds possess gradual ST behaviour starting at around 200 K and passing through room temperature (Fig. 40b, c). The compounds were synthesized by the same protocol, and TGA analyses determined the number of interstitial water and solvent molecules.

In the case of the Fe^{II}/Fe^{III} compound, the X-ray single-crystal structure reveals 14 molecules of acetonitrile within the crystal lattice. The magnetic investigations of this compound carried out on samples in the presence of water or not show that the ST is more gradual when water molecules are included (Fig. 40a). At low temperatures, the χT value only reflects the contribution from the LS Fe^{III} sites; therefore, the three Fe^{II} sites of the cluster must be LS up to 100 K, which is in agreement with the results of Mössbauer spectroscopy. Above this temperature, the χT product gradually increases and is not yet saturated at 375 K. At

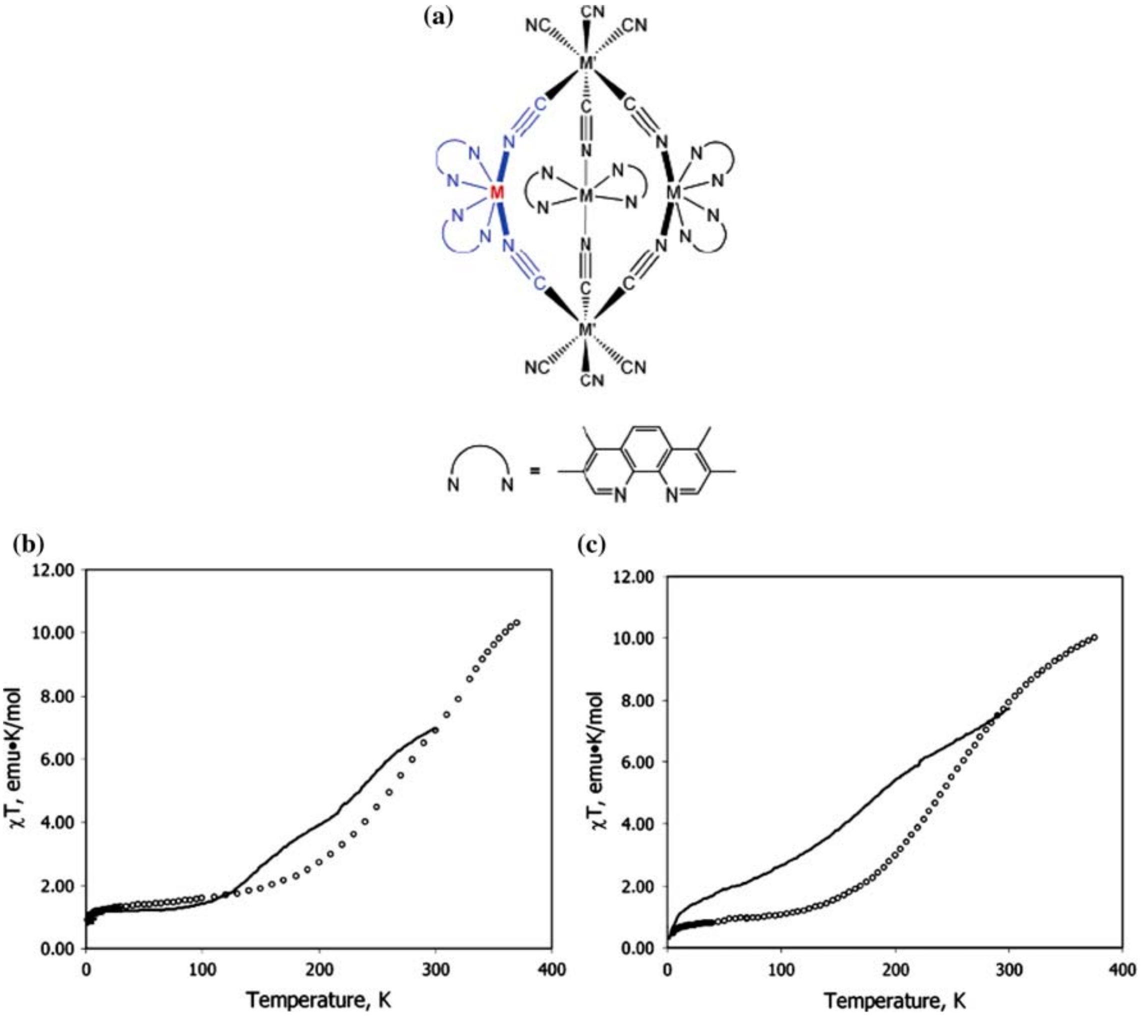

Fig. 40 Schematic molecular view of **a** the structure of the $[M^{II}(tmphen)_2]_3[M'^{III}(CN)_6]$ cluster, and representations of the magnetic properties of **b** $[Fe^{II}(tmphen)_2]_3[Fe^{III}(CN)_6]$ and **c** $[Fe^{II}(tmphen)_2]_3[Co^{III}(CN)_6]$ (water-containing samples: *open circles*; acetonitrile-wetted crystals: *solid line*)

300 K, after subtracting out the LS contribution of Fe^{III}, χT is equal to 5.3 emu K mol^{-1}, which corresponds to $\approx$1.8 HS Fe^{II} ($\chi_{HS(FeII)} \approx 60\%$) per one molecule of cluster.

Low-temperature Mössbauer spectroscopy (at 4.2 K) of the second series of complexes, $[Fe^{II}(tmphen)_2]_3[Co^{III}(CN)_6]\cdot xCH_3CN$ (with $x = 7.7$; 18; 11; 7.6), reveals that 10–20% HS Fe^{II} is present, which was attributed to impurities. The amount of paramagnetic impurities does not change up to 50 K, but at room temperature 66% of the iron(II) is converted into the HS state. Also in this case, the ST continues above 300 K and saturation begins at 375 K (Fig. 40c). The magnetic behaviour of a third compound, $[Fe^{II}(tmphen)_2]_3[Cr^{III}(CN)_6]\cdot 22CH_3CN$, follows the Curie law and the χT value corresponds to two isolated Cr^{III} centres, indicating that the three Fe^{II} nuclei are LS up to 300 K. A similar Fe_3^{III}–Cr^{III} Prussian blue analogue was also reported by Herchel et al. [77], which shows a gradual ST from 5 K up to above room temperature.

In 1997, Fallon et al. [78] reported the mononuclear ST complex $[Fe^{III}(dmptacn)Cl][PF_6]_2\cdot MeOH$, (dmptacn = 1,4-bis(pyridin-2-yl-methyl)-1,4,7-triazacyclononane), coordinated by three nitrogens from the triazacyclononane ring and with two nitrogens from two pyridine substituents. In the temperature range of 4.2 K to ca. 100 K, the compound remains in the LS iron(III) state. The ST starts above 150 K and reaches 3.58 μ_B at 300 K, which is close to the expected value for the intermediate spin state of $iron^{III}$ (IS, $S = 3/2$, spin-only value $\mu_{eff} = 3.88\ \mu_B$). Unfortunately, variable-temperature magnetic measurements of this compound were only carried out up to 300 K; no experimental data that allow us to discern whether the ST continues beyond the intermediate state (IS) above room temperature are available. For a recent review of Fe(III) SC, see Ref. [79].

Theoretical background of ST processes

The spin crossover process can be viewed as a unimolecular reaction LS ↔ HS, for which the high-spin mole fraction (x_{HS}) and the low-spin mole fraction (x_{LS}) fulfill the normalization $x_{\mathrm{LS}} + x_{\mathrm{HS}} = 1$. The transformation is an entropy-driven process conditioned by positive enthalpy and entropy changes, $\Delta H > 0$, $\Delta S > 0$. Therefore, a critical temperature ($T_{\mathrm{c}} = T_{1/2}$) exists above which the change in Gibbs energy is negative ($\Delta G < 0$) so that the reaction proceeds spontaneously. The equilibrium constant $K = x_{\mathrm{HS}}/(1 - x_{\mathrm{HS}})$ obeys the van't Hoff equation, so the function ln$K$ versus $1/T$ is linear. At the critical temperature, $x_{\mathrm{HS}} = 0.5$ is fulfilled and so $\ln K(T_{\mathrm{c}}) = 0$ (Fig. 41).

The real systems differ from the above idealisation in that the Boltzmann statistics are influenced by interactions in the solid state. The cooperativeness originates from the interaction energy, which can be written in the form

$$E_{\mathrm{int}}(x_{\mathrm{HS}}) = E_{\mathrm{LL}}(1 - x_{\mathrm{HS}})^2 + 2E_{\mathrm{LH}}x_{\mathrm{HS}}(1 - x_{\mathrm{HS}}) + E_{\mathrm{HH}}x_{\mathrm{HS}}^2 \quad (7)$$

Here E_{LL}, E_{LH} and E_{HH} refer to the pair-interaction energies. This equation can be rewritten as

$$E_{\mathrm{int}}(x_{\mathrm{HS}}) = j_0 + j_1 x_{\mathrm{HS}} + j_2 x_{\mathrm{HS}}^2 \quad (8)$$

with the individual coefficients introduced as follows

$$j_0 = E_{\mathrm{LL}} \quad (9)$$

$$j_1 = 2E_{\mathrm{LH}} - 2E_{\mathrm{LL}} = \left(\frac{\partial E_{\mathrm{int}}}{\partial x_{\mathrm{HS}}}\right) = \mu \quad (10)$$

$$j_2 = E_{\mathrm{LL}} + E_{\mathrm{HH}} - 2E_{\mathrm{LH}} = \frac{1}{2}\left(\frac{\partial^2 E_{\mathrm{int}}}{\partial x_{\mathrm{HS}}^2}\right) = \eta. \quad (11)$$

One can reconsider Eq. 8 as the Taylor expansion of the interaction energy in terms of the high-spin mole fraction, where μ is the chemical potential (equal to minus the absolute electronegativity) [80] and η is the chemical hardness [81, 82]. The relationship between the interaction parameters is shown in Fig. 42.

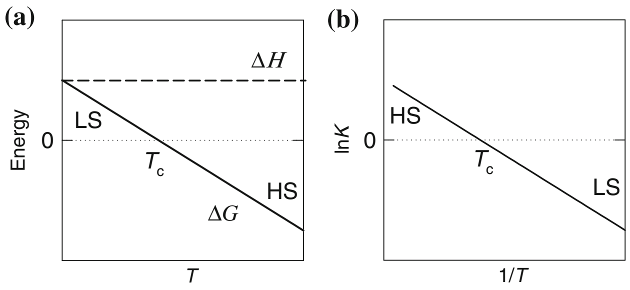

Fig. 41 Thermodynamics of the spin crossover process: **a** temperature variation of the Gibbs energy, **b** the van't Hoff plot

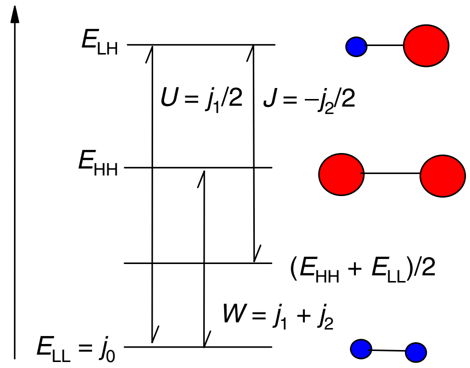

Fig. 42 The relationship between the interaction parameters

The identification of the second-order coefficient as the chemical hardness ($j_2 = \eta$) allows a more detailed inspection of the nature of the cooperativeness [83]. The conventional cooperativeness parameter J is introduced through the relationship [84]

$$J = E_{\mathrm{LH}} - (E_{\mathrm{HH}} + E_{\mathrm{LL}})/2 = -j_2/2 > 0 \quad (12)$$

as the difference between the interaction energy between dissimilar spins (E_{LH}) and the average of the interaction energy for same-spin pairs.

The first-order contribution to the cooperativeness j_1 (the "chemical potential") disappears on the assumption that

$$W = j_1 + j_2 = E_{\mathrm{HH}} - E_{\mathrm{LL}} \to 0 \quad (13)$$

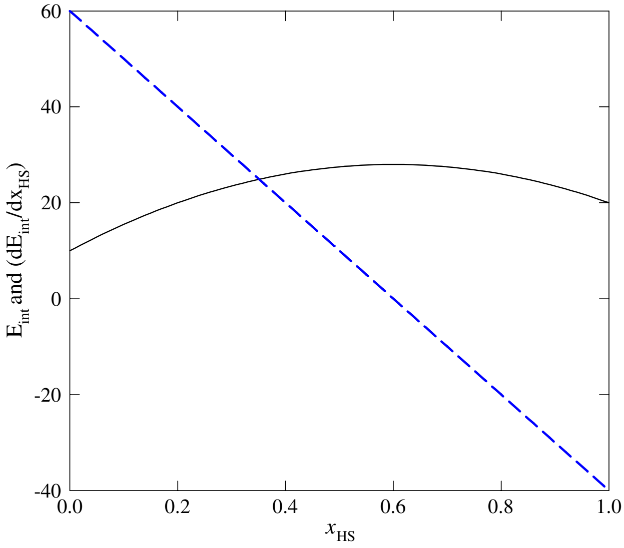

Fig. 43 Dependence of the interaction energy (*solid*) and its derivative (*dashed*) on the high-spin mole fraction. $E_{\mathrm{LL}} = 10$, $E_{\mathrm{LH}} = 40$, $E_{\mathrm{HH}} = 20$ (arbitrary units)

Table 3 Thermodynamic data on mononuclear complexes

No	System/note (abbreviations of the ligands under *A1*)	Method^a	T_c [K]^b	ΔH kJ mol^{-1}	ΔS J K^{-1} mol^{-1}	$\Delta H/\Delta S$	J/k [K]^c	References
(A) $T_c < 200$ K, mono- and bidentate ligands								
1	$[Fe(py)_2phen(NCS)_2]\cdot 0.5py$	DSC	106	3.7	37.0	100		Claude et al. [87]
	flexible monodentate ligands							
2	$[Fe(py)_2bpym(NCS)_2]\cdot 0.5py$	DSC	116	6.5	56	116		Claude et al. [87]
	flexible monodentate ligands							
3	$[Fe(2\text{-}pic)_3]Cl_2\cdot EtOH$	Mg	114.0	6.14	50.6	121.3	123	Kaji and Sorai [88]
	flexible bidentate ligands, two-step		122.2					
4	$[Fe(2\text{-}pic)_3]Cl_2\cdot MeOH$	Cal	150	8.88	59.5	149		Nakamoto et al. [89]
	flexible bidentate ligands							
5	$[Fe(2\text{-}pic)_3]Cl_2\cdot H_2O$	Cal	280	17.1	59.4	288		Nakamoto et al. [90]
	flexible bidentate ligands							
6	$[Fe(btr)_2(NCS)_2]\cdot H_2O$	DSC	132	10.2	76.4	134		Martin et al. [91]
7	$[Fe(Hpt)_3](BF_4)_2\cdot 2H_2O$	DSC	150	5.81	39.5	147		Roubeau et al. [92]
8	$[Fe(pybzim)_3](ClO_4)_2\cdot H_2O$	DSC	153	2.92	19.0	154	114	Boča et al. [83]
	rigid bidentate ligands	MgX	141	2.62	18.5	142	112	Boča et al. [83]
9	$[Fe(5NO_2\text{-}sal(1,4,7,10))]$,	MgX	145(↑)	7.6	50	152	280	Petrouleas et al. [93]
	flexible hexadentate ligand, two-step		180(↑)					
10	$[Fe(4ditz)_3](PF_6)_2$ 0.25EtOH,	DSC	168(↑)	18.8	109	172		Bartel et al. [94]
	two-step		180(↑)					
11	$[Fe(4ditz)_3](PF_6)_2$ 0.075MeOH,	DSC	174(↑)	9.6	55.3	174		Bartel et al. [94]
	two-step		181(↑)	9.0	49.7	181		
12	$[Fe(phen)_2(NCS)_2]$	Cal	176.3	8.60	48.8	176.2		Sorai et al. [95]
	rigid bidentate ligands							
13	α-$[Fe(dppa)_2(NCS)_2]$	MgX	178	6.9	39	177	160	Matouzenko et al. [96]
14	$[Fe(dpyatriz)_2(SCN)_2]$	DSC	200	7.45	37.7	198		Quesada et al. [97]
15	$[Fe(bpy)_2(NCS)_2]$	DSC	212	10	48	208		Kulshreshtha and Iyer [98]
	rigid bidentate ligands							
16	$[Fe(PM\text{-}BiA)_2(NCS)_2]$	DSC	168	10.06	59.88	168		Letard et al. [99]
			173	10.05	58.09	173		
(B) $T_c > 200$ K, tridentate ligands								
17	$[Fe(dapp)(abpt)](ClO_4)_2$	DSC	186	15.4	83.7	184		Miyazaki et al. [100]
18	$[Fe(trim)_2]Cl_2\cdot 0.5MeOH$	MoS	170	11	64	172		Lemercier et al. [101]
19	$[Fe(trim)_2](PhCO_2)(ClO_4)$	MgX	220	14.4	65	226	170	Lemercier et al. [102]
20	$[Fe(phen)_2(NCSe)_2]$	Cal	231.3	11.60	51.2	227		Sorai et al. [95]
	rigid bidentate ligands							
21	$[Fe(phy)_2](ClO_4)_2$	DSC	248	15.8	65	243		Kulshreshtha and Iyer [103]
22	$[Fe(phy)_2](BF_4)_2$	DSC	283	15.6	56	279		Kulshreshtha and Iyer [103]
23	$[Fe(bzimpy)_2](BPh_4)_2\cdot 4H_2O$	MgX	330(↑)	14.9	45	331	226	Boča et al. [104]
24	$[Fe(bzimpy)_2](ClO_4)_2\cdot 0.25H_2O$	DSC	414(↑)	17.4	43.1	404		Boča et al. [45]
			406(↓)					
		MgX	409(↑)	17.9	44.4	403	418(b)	Boča et al. [45]
			397(↓)				454(c)	
25	$[Fe(tzimpy)_2](ClO_4)_2\cdot H_2O$	MgX	340(↑)	11.9	37	322	424	Boča et al. [46]
			305(↓)					
25	$[Fe(bzimpy_{-1H})_2\cdot H_2O$	MgX	424(↑)	18.1	43	421	519	Boča et al. [46]
		DSC	425(↑)					Papánková et al. [105]
26	$[Fe(trim)_2]Br_2\cdot MeOH$	MoS	340	13.0	38.2	340		Thiel et al. [51]

Table 3 continued

No	System/note (abbreviations of the ligands under *A1*)	Method[a]	T_c [K][b]	ΔH kJ mol^{-1}	ΔS J K^{-1} mol^{-1}	$\Delta H/\Delta S$	J/k [K][c]	References
27	$\{[Fe^{II}(Htrz)_3]\}_n(BF_4)_{2n}$	DSC	334	8.9(↑)				Kroeber et al. [19]
	Polymorph α[d]			9.5(↓)				
28	$\{[Fe^{II}(Htrz)_2(trz)]\}_n(BF_4)_n$ Polymorph A[d]	DSC	361	27.8(↑)				Kroeber et al. [19]
				28.6(↓)				
	Polymorph B[d]		363	22.5				
(C) Fe(III) complexes								
29	$[Fe^{III}(3MeO\text{-}salenEt)_2]PF_6$	Cal	162.3	5.94	36.7	161.9		Sorai et al. [106]
30	$[Fe^{III}(3EtO\text{-}salapa)_2]\ ClO_4{\cdot}C_6H_4Cl_2$	Cal	150	5.38	39.5	136		Conti et al. [107]
31	$[Fe^{III}(3EtO\text{-}salapa)_2]\ ClO_4{\cdot}C_6H_5Br$	Cal	165	7.99	40.4	198		Sorai [108]
32	$[Fe^{III}(3EtO\text{-}salapa)_2]\ ClO_4{\cdot}C_6H_6$	Cal	187	7.08	34.8	203		Kaji et al. [109]
33	$[Fe^{III}(3EtO\text{-}salapa)_2]\ ClO_4{\cdot}C_6H_5Cl$	Cal	188	6.34	36.1	176		Sorai et al. [110]
34	$[Fe^{III}(acpa)_2]PF_6$	Cal	190	7.03	36.2	194		Sorai et al. [111]

For the ligand abbreviation, see the table in the "Appendix"

[a] *Cal*, adiabatic calorimetry; *DSC*, differential scanning calorimetry; *MgX*, fitting the magnetic susceptibility (Ising-like model); *MoS*, fitting the Mössbauer spectra

[b] T_c, critical temperature for $x_{HS} = 0.5$; peak values T_p are reported for DSC and adiabatic calorimetry

[c] J, solid-state cooperativeness—a model-dependent quantity; multiple values refer to different models

[d] See text—triazole part

The role of the first-order parameter j_1 has not been modelled so far, except in one paper [85]. The effect of the cooperativeness on the total interaction energy is shown in Fig. 43.

As reviewed elsewhere [13], the molar Gibbs energy can be constructed from the following contributions:

$$G = x_{HS}G^o_{HS} + (1 - x_{HS})G^o_{LS} - TS_{mix} + E_{int} \qquad (14)$$

where G^o_{HS} (G^o_{LS}) is the molar Gibbs energy for the HS (LS) molecules in the absence of any cooperative interaction, and

$$S_{mix} = -(R/n)\{x_{HS}\ln x_{HS} + (1 - x_{HS})\ln(1 - x_{HS})\} \qquad (15)$$

represents the mixing entropy in the regular solution/domain model (n is the number of molecules per domain). The requirement for equilibrium demands

$$\left(\frac{\partial G}{\partial x_{HS}}\right)_{T,p} = G^o_{HS} - G^o_{LS} + (RT/n)\ln\left(\frac{x_{HS}}{1 - x_{HS}}\right) + j_1 + 2j_2x_{HS} = 0 \qquad (16)$$

and at the transition temperature, where the high-spin mole fraction is $x_{HS} = 0.5$, the following expression is obtained:

$$\Delta G^o = G^o_{HS} - G^o_{LS} + j_1 + j_2\big|_{T=T_{1/2}} = 0 \qquad (17)$$

The transition temperature

$$T_{1/2} = (\Delta H^o + j_1 + j_2)/\Delta S^o \qquad (18)$$

then involves the cooperativeness factors (unless the cancellation $W = j_1 + j_2 \rightarrow 0$ is assumed in the theoretical model, as it is in the case of the Ising-like model). Moreover, there is no need to restrict ourselves to two-body interactions [86]; three-body ones will produce a third-order term $j_3x^3_{HS}$ in Eq. 8 that gives rise to an additional term $\Delta T_{1/2} = (3/4)j_3/\Delta S$ in Eq. 18.

Equation 18 is a key formula for understanding the transition temperature and the factors that influence it. It is evident that an increase in ΔH (disfavouring a ST) will shift the transition temperature to higher values. This factor can be tuned chemically in a transparent way.

Let us consider a monodentate donor set, like the compounds $[Fe^{II}(py)_2phen(NCS)_2]{\cdot}0.5py$ and $[Fe^{II}(py)_2bpym(NCS)_2]{\cdot}0.5py$, numbered (1) and (2) in Table 3. Their $T_{1/2}$ values (106 and 116 K, respectively) lie at the lowest edge of the reported values for iron(II) complexes. At the same time, the enthalpy of the ST has rather small values, $\Delta H = 4$–6 kJ mol^{-1}. This quantity matches the electron energy difference between the LS and HS states, corrected to the zero-point vibrations: $\Delta H = (E_{el} + e_{vib})_{HS} - (E_{el} + e_{vib})_{LS}$. Analogous behaviour is exhibited by the compound $[Fe^{II}(2\text{-}pic)_3]Cl_2{\cdot}EtOH$, numbered (3) in Table 3, though it contains flexible bidentate ligands (2-picolylamine). The term "flexible ligand" is used in the sense that the single bonds allow the donor atoms to be positioned in near-octahedral positions for both the LS and HS states. Interestingly, the rigid ligands (e.g. bpy, phen, bzimpy) cause a positive shift in the $T_{1/2}$. The term "rigid ligand" here means that the octahedral positions of donor atoms cannot be maintained as the Fe^{II}–N bond lengths increase during the ST. In general, the substitution of flexible ligands with rigid ones causes an increase in the ΔH (although there are some exceptions). The enthalpic barrier $\Delta H > 10$ kJ mol^{-1} is most marked for rigid tridentate ligands, as listed in Table 3.

However, ΔH is not the only factor entering $T_{1/2}$, since the value of ΔS assists in the denominator. Its variation is more difficult to understand. It basically includes the electronic (spin) and vibrational parts; the second one is dominant. It also reflects other degrees of freedom in the solid state, like the free or hindered rotations of groups, etc. Therefore, chemically tuning it is a far from routine task. Even in the case where ΔH is increasing, ΔS can decrease, increase, or to stay the same, which can produce an unexpected final $T_{1/2}$.

The cooperativeness factor $W = j_1 + j_2 + \ldots$ acts in symbiosis with the ΔH value in the numerator for $T_{1/2}$. Note that the solid-state cooperativeness is a fictitious quantity that cannot be measured directly; it is a model-dependent parameter that acts like the activity in equations for ideal solutions when applied to real solutions. The real thermodynamic enthalpy and the entropy change (detectable by calorimetry) are temperature-dependent quantities: $\Delta H(T)$ and $\Delta S(T)$; these naturally include the cooperativeness as $\Delta H = \Delta H^{o} + j_1 + j_2$. The cooperativeness, however, causes a nonlinearity in the van't Hoff plot around $\ln K = 0$. When $W/k > T_c$, the system exhibits a thermal hysteresis on heating/cooling.

Conclusion

This review describes the state of the art in research on iron ST complexes in relation to their room-temperature switching, a critical criterion for the integration of ST compounds as active components into application devices. The survey showed that there are an increasing number of iron(II) and iron(III) complexes with critical temperatures around room temperature, and in general the iron(II) ST complexes exhibit more abrupt transitions $T_{1/2}$ combined with occasionally very large temperature-induced hystereses $\Delta T_{1/2}$. Coexistence of the latter two ST parameters leads to bistability at ambient conditions, mostly in their solid-state bulk phases. Iron(II) ST complexes also show maximal magnetic discrimination between dia- and paramagnetic states, while iron(III) ST complexes have to deal with two different paramagnetic states (and sometimes even an intermediate spin state). Such a situation complicates the spin-state picture; on the other hand, this class of ST compounds often delivers more pronounced thermochromism.

A common disadvantage of all iron ST systems is that they sometimes show extreme sensitivity to local environmental influences, including crystal packing, inclusion of solvent and anion/cation molecules, and concomitant crystalline phase transition events. The recent report on neutral ST complexes with room-temperature critical temperatures and large hystereses appears to be a first step towards circumventing such problems (such as excluding anions at the very least).

Generally speaking, critical switching temperatures at ambient conditions seem to be favoured (1) by the use of rigid, multi (preferentially ter)-dentate ligand systems. Desirable wide regions of bistability around room temperature can be achieved (2) by multidimensional (1D, 2D, 3D) interlinking of the respective mononuclear ST centres through relatively weak but multiple hydrogen-bonding networks or stronger coordination bond networks. The use of multinuclear ST compounds does not seem to be useful in this respect, particularly due to the potential for magnetic exchange processes that dilute the magnetic response and lead to more complex switching schemes.

However, the full process of introducing, integrating, and implementing ST complexes as active units into molecular hybrid devices still has some way to go. The recent reports that persistent ST switching has been observed, even in nanoscale thin layers and particles, are important since they provide the basis for introducing ST into device architectures. However, spin-state switching in such highly predefined device environments [112, 113] may require—in addition to the previously described triggers of temperature, pressure and light—the development of more suitable triggers, for example the direct application of electrical fields or the implementation of single-molecule optical readout of spin state. Generally speaking, addressing single monolayers or even molecules is yet to be investigated as a research topic, and the inherent tendency of ST compounds to respond to multiple triggers simultaneously is a problem that will probably need to be tackled in the future [114]. However, despite these many remaining challenges, ST remains a uniquely attractive phenomenon that is equally appealing to chemists, physicists, biologists and electrical engineers, since it points to new horizons in molecular data processing and storage [115].

Acknowledgments Grant agencies and project sponsors (Germany: DFG-Center for Functional Nanostructures, Project E3; Slovakia: VEGA 1/0213/08, APVV 0006-07, COST-0006-06, VVCE 0004-07) are acknowledged for their financial support.

Appendix

A1 Abbreviations of ligands

1,2,4-triazole type of ligands	
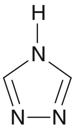 1,2,4-triazole **Htrz**	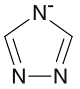 1,2,4-triazole(–) **trz**(–)
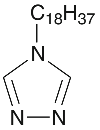 4-(n-octadecyl)- 1,2,4-triazole **C$_{18}$H$_{37}$trz**	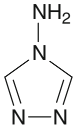 4-(amino)- 1,2,4-triazole **4-NH$_2$trz**
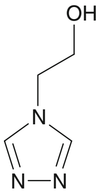 4-(2-hydroxyethyl)- 1,2,4-triazole **hyettrz**	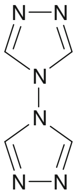 4,4’-bis(1,2,4-triazole) **btrz**
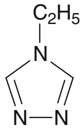 4-ethyl- 1,2,4-triazole **ettrz**	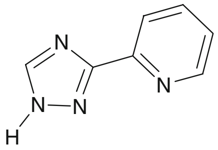 3-(pyridin-2-yl)-1,2,4-1H-triazole **Hpt**

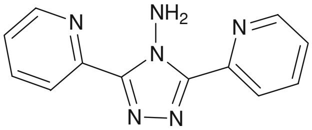 4-amino-3,5-bis(pyridin-2-yl)-1,2,4-triazole **abpt**	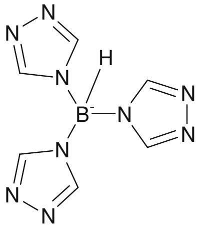 bis[hydrotris(1,2,4-triazol-1-yl)borate] **HB(trz)$_3$**
N-donor Ligands with six membered ring	
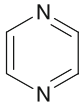 pyrazine **pz**	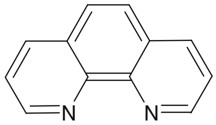 1,10-phenantroline **phen**
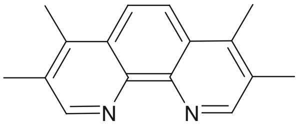 3,4,7,8-tetramethyl-1,10-phenantroline **tmphen**	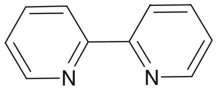 2,2’-bipyridine **2,2’-bipy**
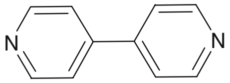 4,4’-bipyridine **4,4’-bipy**	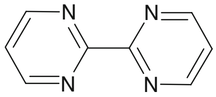 2,2’-bipyrimidine **bpym**

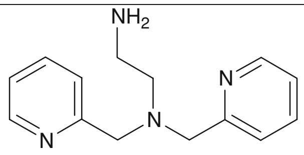 (3-aminopropane-1-yl)bis(pyridin-2-yl-methyl)amine **DPPA**	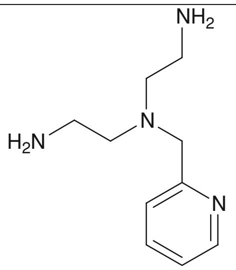 bis(3-aminopropyl)(2-pyridylmethyl)amine **dapp**
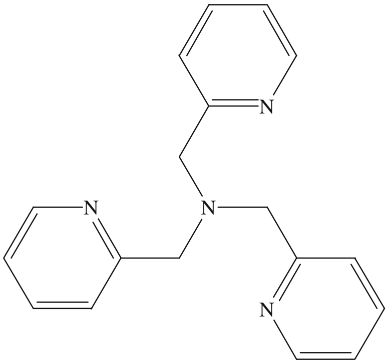 tris(2-pyridylmethyl)amine **TPyA**	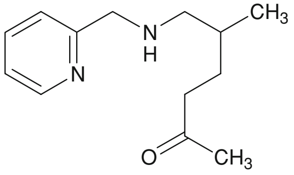 N−(1-acetyl-2-propylidene)(2-pyridylmethyl)amine **Hacpa**

Bis(pyrazol-n-yl)pyridine ligands	
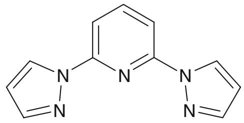 2,6-bis(pyrazol-1-yl)pyridine **1-bpp**	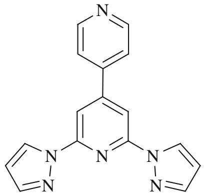 2,6-bis(pyrazol-1-yl)-4,4'-bipyridine **1-bpp-4-py**
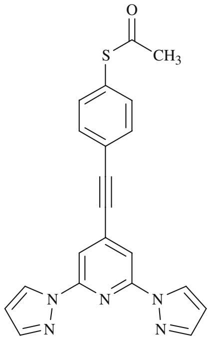 *S*-(4-{[2,6-(bispyrazol-1-yl)pyrid-4-yl]ethynyl}-phenyl)ethanethioate **1-bpp-4-acety-ph-SAc**	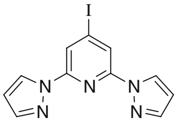 4-iodo-2,6-bis(pyrazol-1-yl)pyridine **1-bpp-4-I**
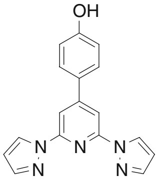 1-bpp-4-ph-OH = 4-(4-hydroxyphenyl)-2,6-bis(pyrazol-1-yl)pyridine **1-bpp-4-ph-OH**	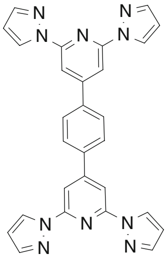 1,4-bis{2,6-bis(pyrazol-1-yl)pyridin-4-yl)benzene) **1-bpp-ph-1-bpp**
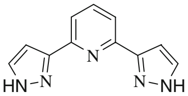 2,6-bis(pyrazol-3-yl)pyridine **3-bpp**	

Benzimidazole types of ligands	
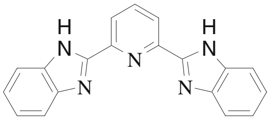 2,6-bis(benzimidazol-2-yl)pyridine **bzimpy**	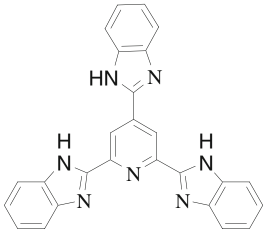 2,4,6-tris(benzimidazol-2-yl)pyridine **tzimpy**
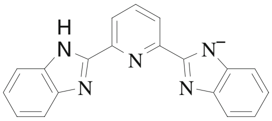 2,6-bis(benzimidazol-2-yl)pyridine(–) **bzimpy$_{\text{-1H}}$**	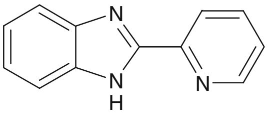 2-(2’-pyridyl)benzimidazole) **pybzim**
Others	
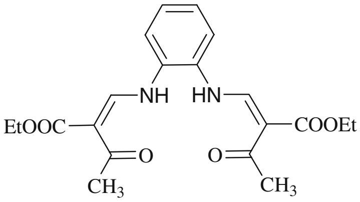 diethyl(E,E)-2,2’-[1,2-phenylenebis -(iminomethylidyne)]-bis(3-butanoate) **Ph(Imoxo)$_2$**	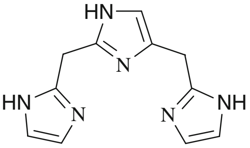 4’-(4-methylimidazole)-2’-(2’’-methyl- imidazole)imidazole **trim**
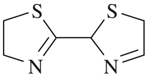 2,2’-bis(2-thiazoline) **bt**	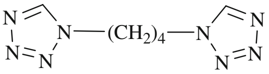 1,4-bis(tetrazol-1-yl)butane **4ditz**

Schiff Base ligands	
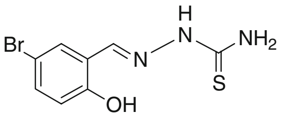 5-bromosalicylaldehyde thiosemicarbazone **H_2(5Br-thsa)**	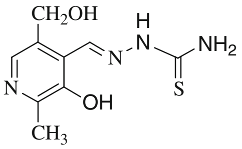 pyridoxal thiosemicarbazone **H(thpy)**
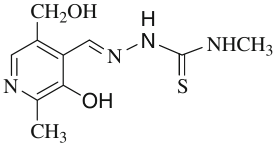 pyridoxal methylthiosemicarbazone **H(mthpy)**	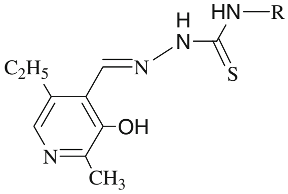 pyridoxal 4-R-thiosemicarbazone R= Ph, Me, Et **H(R-thsa)**,
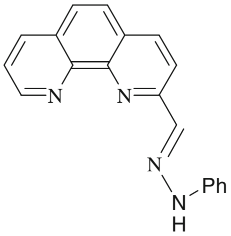 1,10-phenantroline-2-carbaldehyde - phenylhydrazone **phy**	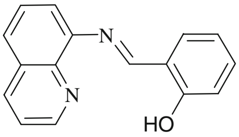 N-(8-quinolyl)salicylaldimine **Hqsal**

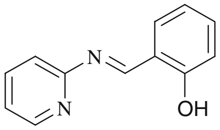 N-bis(2hydroxyphenyl)-(2-pyridyl)-methaneimine **Hpap**	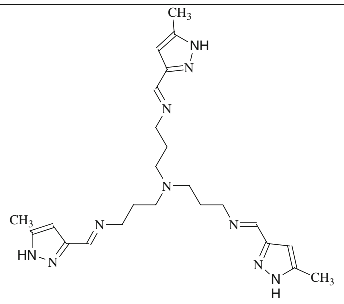 Schiff base condensate of 5-methylpyrazole-3-carbaldehyde and tris(2-aminoethyl)amine **H_3L**
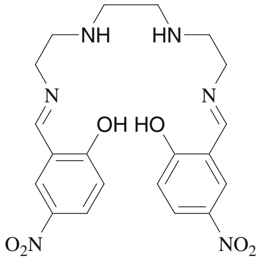 Schiff base condensed from 5-nitrosalicylaldehyde and 1,4,7,10-tetraazadecane (2:1) **5NO_2-sal-(1,4,7,10)**	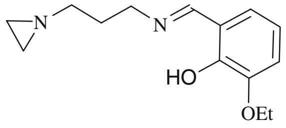 Schiff base condensed from 3-ethoxysalicylaldehyde and *N*-aminopropylaziridine (1:1) **3OEt-salapa**
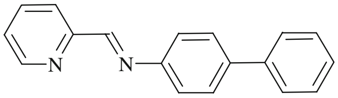 *N*-(2-pyridylmethylene)aminobiphenyl **PM-BiA**	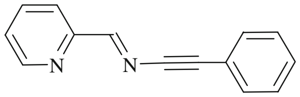 *N*-(2'-pyridylmethylene)-4-(phenylethynyl)aniline **PM-PEA**

References

1. Cambi L, Szegö L, Cassano A (1932) Acad Naz Lincci 15:329
2. Ferlay S, Mallah T, Ouahes R, Veillet P, Verdaguer M (1995) Nature 378:701
3. Kahn O, Martinez CJ (1998) Science 279:44
4. Gütlich P, Hauser A, Spiering HC (1994) Angew Chem Int Ed 33:2024
5. Real JA, Gaspar AB, Munoz MC (2005) J Chem Soc Dalton Trans 2062

6. Niel V, Martinez-Agudo JM, Munoz MC, Gaspar AB, Real JA (2001) Inorg Chem 40:3838
7. Zaworotko MJ (2000) Angew Chem Int Ed 39:3052
8. Yaghi OM, O'Keeffe M, Ockwig NW, Chae HK, Eddaoudi M, Kim J (2003) Nature 423:705
9. Beauvais LG, Long JR (2002) J Am Chem Soc 115:9810
10. Coronado E, Galan-Mascaros JR, Garcia-Gomez CJ, Laukhin V (2000) Nature 408:447
11. Bousseksou A, Molnar G, Demont P, Menegotto (2003) J Mater Chem 13:2069
12. Halder GJ, Kepert CJ, Moubaraki B, Murray KS, Cashion JD (2002) Science 298:1762
13. Boča R, Linert W (2003) Monat Chem 134:199
14. Mikami M, Konno M, Saito Y (1980) Acta Cryst B36:275
15. Madhu NT, Salitros I, Schramm F, Kyatskya S, Fuhr O, Ruben M (2008) Compt Rend Chimie 11:1166
16. Gütlich P (1981) Struct Bonding 44:83
17. Armand F, Badoux C, Bonville P, Ruaudel-Teixier A, Kahn O (2003) Langmuir 11:3467
18. Michalowicz A, Moscovici J, Ducourant B, Cracco D, Kahn O (1995) Chem Mater 7:1833
19. Kroeber J, Audiere JP, Claude R, Codjovi E, Kahn O, Haasnoot JG, Groliere F, Jay C, Bousseksou A (1994) Chem Mater 6:1404
20. Coronado E, Ramon Galan-Mascaros J, Monrabal-Capilla M, Garcia-Martinez J, Pardo-Ibanez P (2007) Adv Mater 19:1359
21. Kröber J, Codjovi E, Kahn O, Groliere F, Jay C (1993) J Am Chem Soc 115:9810
22. Codjovi E, Sommier L, Kahn O (1996) New J Chem 20:503
23. Cantin C, Daubric H, Kliava J, Servant Y, Sommier L, Kahn O (1998) J Phys Condens Matter 10:7057
24. van Konningsbruggen PJ, Gracia Y, Codjovi E, Lapouyade R, Kahn O, Fournes L, Rabardel L (1997) J Mater Chem 7:2069
25. Garcia Y, van Koningsbruggen PJ, Lapouyade R, Rabardel L, Michalowicz A. Kahn O, Wieczorek M, Bronisz R, Ciunik Z, Rudolf MF (1998) C R Acad Paris IIC 523
26. Garcia Y, Guionneau P, Bravic G, Chasseau D, Howard JAK, Kahn O, Ksenofontov V, Reimanand S, Gütlich P (2000) Eur J Inorg Chem 25:1531
27. van Koningsbruggen PJ, Miller JS (2008) Solid State Sci (in press)
28. Niel V, Martinez-Agudo JM, Muñoz MC, Gaspar AB, Real JA (2001) Inorg Chem 40:3838
29. Bonhommeau S, Molnár G, Galet A, Zwick A, Real JS, McGarvey JJ, Bousseksou A (2005) Angew Chem Int Ed 44:4069
30. Cobo S, Molnár G, Real JA, Bousseksou A (2006) Angew Chem Int Ed 45:5786
31. Larionova J, Salmon L, Guari Y, Tokarev A, Molvinger K, Molnár G, Bousseksou (2008) Angew Chem Int Ed 47:8236
32. Boldog I, Gaspar AB, Marínez V, Pardo-Ibañez P, Ksenofontov V, Bhattacharje A, Gütlich P, Real JA (2008) Angew Chem Int Ed 47:6433
33. Munoz MC, Gaspar AB, Galet A, Real JA (2007) Inorg Chem 46:8182
34. Holland JM, McAllister JA, Kilner CA, Thornton-Pett M, Bridgeman AJ, Halcrow MA (2002) J Chem Soc Dalton Trans 548
35. Holland JM, McAllister JA, Lu Z, Kilner CA, Thornton-Pett M, Halcrow MA (2001) Chem Commun 577
36. Halcrow MA (2007) Polyhedron 26:3523
37. Halcrow MA (2005) Coord Chem Rev 249:2880
38. Rajadurai Ch, Schramm F, Brink S, Fuhr O, Ghafari M, Kruk R, Ruben M (2006) Inorg Chem 45:10019
39. Rajadurai Ch, Schramm F, Fuhr O, Ruben M (2008) Eur J Inorg Chem 2649
40. Rajadurai Ch, Fuhr O, Kruk R, Ghafari M, Hahn H, Ruben M (2007) Chem Commun 2636
41. Clemente-León M, Coronado E, Giménez-López MC, Romero FM (2007) Inorg Chem 46:11266
42. Weber B, Bauer W, Obel J (2008) Angew Chem Int Ed 47 (in press)
43. Müller BR, Leibeling B, Jäger BG (2000) Chem Phys Lett 319:368
44. Boča R, Baran P, Dlhan L, Fuess H, Haase W, Renz F, Linert W, Svoboda I, Wemer R (1997) Inorg Chim Acta 260:129
45. Boča R, Boča M, Dlhan L, Falk K, Fuess H, Haase W, Jarosciak R, Papankova B, Renz F, Vrbova M, Werner R (2001) Inorg Chem 40:3025
46. Boča R, Renz F, Boča M, Fuess H, Haase W, Kickelbick G, Linert W, Vrbova-Schikora M (2005) Inorg Chem Comm 8:227
47. Sams JR, Tsin TB (1976) Inorg Chem 15:1544
48. König E, Ritter G, Kulshreshtha SK, Waigler J, Goodwin HA (1984) Inorg Chem 23:1896
49. Konig E, Kanellakopulos B, Powietzka B, Goodwin HA (1990) Inorg Chem 29:4944
50. König E, Ritter G, Waigler J, Goodwin HA (1985) J Chem Phys 83(6):3055
51. Thiel A, Bousseksou A, Verelst M, Varret F, Tuchagues JP (1999) Chem Phys Lett 302:549
52. Min KS, DiPasquale A, Arnold L, Rheingold AL, Miller JS (2007) Inorg Chem 46:1048
53. Nihei M, Ui M, Yokota M, Han L, Maeda A, Kishida H, Okamoto H, Oshio H (2005) Angew Chem Int Ed 44:6484
54. Wells FV, McCann SV, Wickman HH, Kessel SL, Hendrickson DN, Feltham RD (1982) Inorg Chem 21:2306
55. Earnshaw A, King EA, Larkworthy LF (1965) Chem Commun 180
56. Earnshaw A, King EA, Larkworthy LF (1969) J Chem Soc A:2459
57. Haller KJ, Johnson PL, Feltham RD, Enemark JH, Ferraro JR, Basile LJ (1979) Inorg Chim Acta 33:119
58. Fitzsimmons BW, Larkworthy LF, Rogers KA (1980) Inorg Chim Acta 44:L53
59. König E, Ritter G, Waigel J, Larkworthy LF, Thompson RM (1987) Inorg Chem 26:1563
60. Flowuet S, Boillot ML, Fiviére E, Varret E, Boukheddaden K, Morineau D, Négrier P (2003) New J Chem 27:341
61. Ryabova NA, Ponomarev VI, Atovmyan, Zelentsov VV, Shipilov VI (1978) Koord Khim 4:119
62. Zelentsov VV, Bogdanova LG, Ablov AV, Gerbeleu NV, Dyatlova CV (1973) Russ J Inorg Chem 18:1410
63. Ryabova NA, Ponomarev VI, Zelentsov VV, Atovmyan LO (1981) Kristallografiya 26:101
64. Ivanov EV, Zelentsov VV, Gerbeleu NV, Ablov AV (1970) Dokl Akad Nauk SSSR 191:827
65. Tido EWY, van Ekenstein GORA, Meetsma A, van Koningsbruggen PJ (2008) Inorg chem 47:143
66. Gupta NS, Mohan M, Jha NK, Antholine WE (1991) Inorg Chim Acta 184:13
67. Hayami S, Gu ZZ, Yoshiki H, Fujishima A, Sato O (2001) J Am Chem Soc 123:11644
68. Dahl BM, Dahl O (1969) Acta Chem Scand 23:1503
69. Dickinson RC, Baker WA Jr, Collins RL (1977) J Inorg Nucl Chem 39:1531
70. Hayami S, Kawahara T, Juhasz G, Kawamura K, Uehashi K, Sato O, Maeda Y (2003) J Radioanal Nucl Chem 255:443
71. Oshio H, Kitazaki K, Mishiro KJ, Kato N, Maeda Y, Takashima Y (1987) J Chem Soc Dalton Trans 1341
72. Hayami S, Maeda Y (1997) Inorg Chim Acta 255:181
73. Hayami S, Gu ZZ, Shiro M, Einaga Y, Fujishima A, Sato O (2000) J Am Chem Soc 122:7126

74. Juhász G, Hayami S, Sato O, Maeda Y (2002) Chem Phys Lett 364:164
75. Brewer CT, Brewer G, Butcher RJ, Carpenter EE, Schmiedekamp AM, Viragh C (2007) J Chem Soc Dalton Trans 295
76. Shatruk M, Dragulescu-Andrasi A, Kristen E, Chambers KE, Stoian SA, Bominaar EL, Achim C, Dunbar KR (2007) J Am Chem Soc 129:6104
77. Herchel R, Boča R, Gembicky M, Kozisek J, Renz F (2004) Inorg Chem 43:4103
78. Fallon GD, McLachlan GA, Moubaraki B, Murray KS, O'Brien L, Spiccia L (1997) J Chem Soc Dalton Trans 2765
79. Nihei M, Shiga T, Maeda Y, Oshio M (2007) Coord Chem Rev 251:2606
80. Sen KD, Jorgensen CK (eds) (1987) Electronegativity (Structure and Bonding 66). Springer, Berlin
81. Sen KD (ed) (1993) Chemical hardness (Structure and Bonding 80). Springer, Berlin
82. Pearson RG (1997) Chemical hardness. Wiley, Weinheim
83. Boča R, Boča M, Ehrenberg H, Fuess H, Linert W, Renz F, Svoboda I (2003) Chem Phys 293:375
84. Kahn O (1993) Molecular magnetism. VCH, New York
85. Rao PS, Ganguli P, McGarvey BR (1981) Inorg Chem 20:3682
86. Koudriavtsev AB (1999) Chem Phys 241:109
87. Claude R, Real JA, Zarembowitch J, Kahn O, Ouahab L, Grandjean D, Boukheddaden K, Varret F, Dworkin A (1990) Inorg Chem 29:4442
88. Kaji K, Sorai M (1985) Thermochim Acta 88:185
89. Nakamoto T, Tan ZC, Sorai M (2001) Inorg Chem 40(15):3805
90. Nakamoto T, Bhattacharjee A, Sorai M (2004) Bull Chem Soc Jpn 77
91. Martin JP, Zarembowitch J, Dworkin A, Haasnoot JG, Codjovi E (1994) Inorg Chem 33:2617
92. Roubeau O, deVos M, Stassen AF, Burriel R, Haasnoot JG, Reedijk J (2003) J Phys Chem Solids 64:1003
93. Petrouleas V, Tuchagues J-P (1987) Chem Phys Lett 137(1):21
94. Bartel M, Absmeier A, Jameson GNL, Werner F, Kato K, Takata M, Boča R, Hasegawa M, Mereiter K, Caneschi A, Linert W (2007) Inorg Chem 46:4220
95. Sorai M, Seki S (1974) J Phys Chem Solids 35:555
96. Matouzenko GS, Bousseksou A, Lecocq S, van Koningsbruggen PJ, Perrin M, Kahn O, Collet A (1997) Inorg Chem 36:5869
97. Quesada M, Monrabal M, Aromi G, de la Pena VA, O'Shea, Gich M, Molins E, Roubeau O, Teat SJ, MacLean EJ, Gamez P Reedijk J (2006) J Mater Chem 16:2669
98. Kulshreshtha SK, Iyer RM (1984) Chem Phys Lett 108:501
99. Letard J-F, Guionneau P, Rabardel L, Howard JAK, Goeta A, Chasseau D, Kahn O (1998) Inorg Chem 37:4432
100. Miyazaki Y, Nakamoto T, Ikeuchi S, Saito K, Inaba A, Sorai M, Tojo T, Atake T, Matouzenko GS, Zein S, Borshch SA (2007) J Phys Chem B 111:12508
101. Lemercier G, Bousseksou A, Verelst M, Varret F, Tuchagues JP (1995) J Magn Magn Mater 150:227
102. Lemercier G, Bousseksou A, Seigneuric S, Varret F, Tuchagues J-P (1994) Chem Phys Lett 226:289
103. Kulshreshtha SK, Iyer RM (1987) Chem Phys Lett 134(3):239
104. Boča R, Baran P, Boča M, Dlháň L, Fuess H, Haase W, Linert W, Papánková B, Werner R (1998) Inorg Chim Acta 278:190
105. Papánková B, Vrbová M, Boča R, Šimon P, Falk K, Miehe G, Fuess H (2002) J Thermal Anal Calorim 67:72
106. Sorai M, Burriel R, Westrum EF, Hendrickson DN (2008) J Phys Chem B 112(14):4344
107. Conti AJ, Kaji K, Nagano Y, Sena KM, Yumoto Y, Chadha RK, Rheingold AL, Sorai M, Hendrickson DN (1993) Inorg Chem 32:2681
108. Sorai M (2001) Bull Chem Soc Jpn 74:2223
109. Kaji K, Sorai M, Contiij AJ, Hendrickson DN (1993) J Phys Chem Solids 54:1621
110. Sorai M, Nagano Y, Conti AJ, Hendrickson DN (1994) J Phys Chem Solids 55:317
111. Sorai M, Maeda Y, Oshio H (1990) J Phys Chem Solids 51:941
112. Ruben M (2005) Angew Chem Int Ed 44:1594
113. Lin N, Stepanov S, Vidal F, Kern K, Alam MS, Strömsdorfer S, Dremow V, Müller P, Landa A, Ruben M (2006) Dalton Trans 43:2794
114. Ruben M, Landa A, Lörtscher E, Riel H, Mayor M, Görls H, Weber HB, Arnold A, Evers F (2008) Small 4:2229
115. Ruben M, Rojo FJ, Romero-Salguero J, Lehn JM, Uppadine L (2004) Angew Chem Int Ed 43:3644